



ISSN 1605-2730

MATERIALS PHYSICS AND MECHANICS

Vol. 42, No. 3, 2019

MATERIALS PHYSICS AND MECHANICS

Principal Editors:

Dmitrii Indeitsev
*Institute of Problems of Mechanical Engineering
of the Russian Academy of Science (RAS), Russia*

Andrei Rudskoi
Peter the Great St.Petersburg Polytechnic University, Russia

Founder and Honorary Editor: Ilya Ovid'ko (1961-2017)

*Institute of Problems of Mechanical Engineering
of the Russian Academy of Sciences (RAS), Russia*

Associate Editors:

Anna Kolesnikova
*Institute of Problems of Mechanical Engineering
of the Russian Academy of Sciences (RAS), Russia*

Alexander Nemov
Peter the Great St.Petersburg Polytechnic University, Russia

Editorial Board:

E.C. Aifantis
Aristotle University of Thessaloniki, Greece

K.E. Aifantis
University of Florida, USA

U. Balachandran
Argonne National Laboratory, USA

A. Bellosi
Research Institute for Ceramics Technology, Italy

A.K. Belyaev
Institute of Problems of Mechanical Engineering (RAS), Russia

S.V. Bobylev
Institute of Problems of Mechanical Engineering (RAS), Russia

A.I. Borovkov
Peter the Great St.Petersburg Polytechnic University, Russia

G.-M. Chow
National University of Singapore, Singapore

Yu. Estrin
Monash University, Australia

A.B. Freidin
Institute of Problems of Mechanical Engineering (RAS), Russia

Y. Gogotsi
Drexel University, USA

I.G. Goryacheva
Institute of Problems of Mechanics (RAS), Russia

D. Hui
University of New Orleans, USA

G. Kiriakidis
IESL/FORTH, Greece

D.M. Klimov
Institute of Problems of Mechanics (RAS), Russia

G.E. Kodzhaspirov
Peter the Great St.Petersburg Polytechnic University, Russia

S.A. Kukushkin
Institute of Problems of Mechanical Engineering (RAS), Russia

T.G. Langdon
University of Southampton, U.K.

V.P. Matveenko
Institute of Continuous Media Mechanics (RAS), Russia

A.I. Melker
Peter the Great St.Petersburg Polytechnic University, Russia

Yu.I. Meshcheryakov
Institute of Problems of Mechanical Engineering (RAS), Russia

N.F. Morozov
St.Petersburg State University, Russia

R.R. Mulyukov
Institute for Metals Superplasticity Problems (RAS), Russia

Yu.V. Petrov
St.Petersburg State University, Russia

N.M. Pugno
Politecnico di Torino, Italy

B.B. Rath
Naval Research Laboratory, USA

A.E. Romanov
Ioffe Physico-Technical Institute (RAS), Russia

A.M. Sastry
University of Michigan, Ann Arbor, USA

B.A. Schrefler
University of Padua, Italy

N.V. Skiba
Institute of Problems of Mechanics (RAS), Russia

A.G. Sheinerman
Institute of Problems of Mechanics (RAS), Russia

R.Z. Valiev
Ufa State Aviation Technical University, Russia

K. Zhou
Nanyang Technological University, Singapore

"Materials Physics and Mechanics" Editorial Office:

Phone: +7(812)552 77 78, ext. 224 **E-mail:** mpmjournal@spbstu.ru **Web-site:** <http://www.mpm.spbstu.ru>

International scientific journal "Materials Physics and Mechanics" is published by Peter the Great St.Petersburg Polytechnic University in collaboration with Institute of Problems of Mechanical Engineering of the Russian Academy of Sciences in both hard copy and electronic versions.

The journal provides an international medium for the publication of reviews and original research papers written in English and focused on the following topics:

- Mechanics of composite and nanostructured materials.
- Physics of strength and plasticity of composite and nanostructured materials.
- Mechanics of deformation and fracture processes in conventional materials (solids).
- Physics of strength and plasticity of conventional materials (solids).
- Physics and mechanics of defects in composite, nanostructured, and conventional materials.
- Mechanics and physics of materials in coupled fields.

Owner organizations: Peter the Great St. Petersburg Polytechnic University; Institute of Problems of Mechanical Engineering RAS.

Materials Physics and Mechanics is indexed in Chemical Abstracts, Cambridge Scientific Abstracts, Web of Science Emerging Sources Citation Index (ESCI) and Elsevier Bibliographic Databases (in particular, SCOPUS).



МЕХАНИКА И ФИЗИКА МАТЕРИАЛОВ

Materials Physics and Mechanics

Том 42, номер 3, 2019 год

Учредители:

ФГАОУ ВО «Санкт-Петербургский политехнический университет Петра Великого»
ФГБУН «Институт проблем машиноведения Российской Академии Наук»

Редакционная коллегия журнала

Главные редакторы:

д.ф.-м.н., чл.-корр. РАН **Д.А. Индейцев**
Институт проблем машиноведения Российской Академии Наук
(РАН)

д.т.н., академик РАН **А.И. Рудской**
Санкт-Петербургский политехнический университет
Петра Великого

Основатель и почетный редактор: д.ф.-м.н. **И.А. Овидько (1961-2017)**

Институт проблем машиноведения Российской Академии Наук (РАН)

Ответственные редакторы

д.ф.-м.н. **А.Л. Колесникова**
Институт проблем машиноведения Российской Академии Наук
(РАН)

к.т.н. **А.С. Немов**
Санкт-Петербургский политехнический университет Петра
Великого

Международная редакционная коллегия:

д.ф.-м.н., проф. **А.К. Беляев**
Институт проблем машиноведения РАН, Россия
д.ф.-м.н. **С.В. Бобылев**
Институт проблем машиноведения РАН, Россия
к.т.н., проф. **А.И. Боровков**
Санкт-Петербургский политехнический у-т Петра Великого, Россия
д.ф.-м.н., проф. **Р.З. Валнев**
Уфимский государственный технический университет, Россия
д.ф.-м.н., академик РАН **И.Г. Горячева**
Институт проблем механики РАН, Россия
д.ф.-м.н., академик РАН **Д.М. Климов**
Институт проблем механики РАН, Россия
д.т.н., проф. **Г.Е. Коджаспиров**
Санкт-Петербургский политехнический у-т Петра Великого, Россия
д.ф.-м.н., проф. **С.А. Кукушкин**
Институт проблем машиноведения РАН, Россия
д.ф.-м.н., академик РАН **В.П. Матвеев**
Институт механики сплошных сред РАН, Россия
д.ф.-м.н., проф. **А.И. Мелькер**
Санкт-Петербургский политехнический у-т Петра Великого, Россия
д.ф.-м.н., проф. **Ю.И. Мещеряков**
Институт проблем машиноведения РАН, Россия
д.ф.-м.н., академик РАН **Н.Ф. Морозов**
Санкт-Петербургский государственный университет, Россия
д.ф.-м.н., чл.-корр. РАН **Р.Р. Мулюков**
Институт проблем сверхпластичности металлов РАН, Россия
д.ф.-м.н., чл.-корр. РАН **Ю.В. Петров**
Санкт-Петербургский государственный университет, Россия
д.ф.-м.н., проф. **А.Е. Романов**
Физико-технический институт им. А.Ф. Иоффе РАН, Россия
д.ф.-м.н. **Н.В. Скиба**
Институт проблем машиноведения РАН, Россия
д.ф.-м.н., проф. **А.Б. Фрейдлин**
Институт проблем машиноведения РАН, Россия
д.ф.-м.н. **А.Г. Шейнман**
Институт проблем машиноведения РАН, Россия

Prof., Dr. **E.C. Aifantis**
Aristotle University of Thessaloniki, Greece
Dr. **K.E. Aifantis**
University of Florida, USA
Dr. **U. Balachandran**
Argonne National Laboratory, USA
Dr. **A. Bellosi**
Research Institute for Ceramics Technology, Italy
Prof., Dr. **G.-M. Chow**
National University of Singapore, Singapore
Prof., Dr. **Yu. Estrin**
Monash University, Australia
Prof., Dr. **Y. Gogotsi**
Drexel University, USA
Prof., Dr. **D. Hui**
University of New Orleans, USA
Prof., Dr. **G. Kiriakidis**
IESL/FORTH, Greece
Prof., Dr. **T.G. Langdon**
University of Southampton, UK
Prof., Dr. **N.M. Pugno**
Politecnico di Torino, Italy
Dr. **B.B. Rath**
Naval Research Laboratory, USA
Prof., Dr. **A.M. Sastry**
University of Michigan, Ann Arbor, USA
Prof., Dr. **B.A. Schrefler**
University of Padua, Italy
Prof. Dr. **K. Zhou**
Nanyang Technological University, Singapore

Тел.: +7(812)591 65 28 E-mail: mpmjournal@spbstu.ru Web-site: <http://www.mpm.spbstu.ru>

Тематика журнала

Международный научный журнал "Materials Physics and Mechanics" издается Санкт-Петербургским политехническим университетом Петра Великого в сотрудничестве с Институтом проблем машиноведения Российской Академии Наук в печатном виде и электронной форме. Журнал публикует обзорные и оригинальные научные статьи на английском языке по следующим тематикам:

- Механика композиционных и наноструктурированных материалов.
- Физика прочности и пластичности композиционных и наноструктурированных материалов.
- Механика процессов деформации и разрушения в традиционных материалах (твердых телах).
- Физика прочности и пластичности традиционных материалов (твердых тел).
- Физика и механика дефектов в композиционных, наноструктурированных и традиционных материалах.
- Механика и физика материалов в связанных полях.

Редколлегия принимает статьи, которые нигде ранее не опубликованы и не направлены для опубликования в другие научные издания. Все представляемые в редакцию журнала "Механика и физика материалов" статьи рецензируются. Статьи могут отправляться авторам на доработку. Не принятые к опубликованию статьи авторам не возвращаются.

Журнал "Механика и физика материалов" ("Materials Physics and Mechanics") включен в систему цитирования Web of Science Emerging Sources Citation Index (ESCI), SCOPUS и PИИЦ.

© 2019, Санкт-Петербургский политехнический университет Петра Великого

© 2019, Институт проблем машиноведения Российской Академии Наук

Contents

Evolution of the droplet shape in the vapor-liquid-solid growth of III-V nanowires under varying material fluxes	265-271
V.G. Dubrovskii, A.S. Sokolovskii	
Study of heat dissipating material using boron nitride fabricated by laser ablation.....	272-279
Atsushi Yamaguchi, Pankaj Koinkar, Akihiro Furube	
Comparative study of adsorption of ozone molecule on pristine and Si doped Single Wall Carbon Nanotube by density functional theory	280-287
R.G. Atram, M.R. Sonawane	
Effect of warm rolling on microstructure, porosity, and hardness of a spray-formed LM25 aluminum alloy	288-295
Bandi Venkata Ramana Reddy, S.R. Maity, K.M. Pandey	
Coupled thermo-electro-mechanical modeling of thermal fatigue of single-crystal corset samples.....	296-310
A.V. Savikovskii, A.S. Semenov, L.B. Getsov	
Numerical method of single-crystal turbine blade static strength estimation taking into account plasticity and creep effects	311-322
Boris Vasilyev, Alexander Selivanov	
Identification of micro-mechanical characteristics of monoclinic tungsten trioxide microparticles by nanoindentation technique	323-329
A.B.D. Nandiyanto, F. Triawan, R. Firly, A.G. Abdullah, Y. Aono, K. Inaba, K. Kishimoto	
Supercomputing analysis of fan-shaped waves in the Earth's crust at the depth of seismic activity.....	330-339
V.M. Sadovskii, O.V. Sadovskaya	
Finite element modeling and investigation of elastic homogeneous and heterogeneous materials	340-350
V.L. Leontiev, I.V. Efremkov	
Neural networks and data-driven surrogate models for simulation of steady-state fracture growth.....	351-358
A.V. Kalyuzhnyuk, R.L. Lapin, A.S. Murachev, A.E. Osokina, A.I. Sevostianov, D.V. Tsvetkov	
Modeling plastic deformation and damage accumulation processes in structural steels under block non-symmetric low-cycle loading	359-366
Ivan A. Volkov, Leonid A. Igumnov, Denis N. Shishulin	
Effect of bamboo weight fraction on mechanical properties in non-asbestos composite of motorcycle brake pad.....	367-372
Y. Sukrawan, A.Hamdani, S.A. Mardani	

EVOLUTION OF THE DROPLET SHAPE IN THE VAPOR-LIQUID-SOLID GROWTH OF III-V NANOWIRES UNDER VARYING MATERIAL FLUXES

V.G. Dubrovskii^{1,2,*}, A.S. Sokolovskii¹

¹ITMO University, Kronverkskiy pr. 49, 197101 St. Petersburg, Russia

²Ioffe Institute RAS, Politekhnicheskaya 26, 194021 St. Petersburg, Russia

*e-mail: dubrovskii@mail.ioffe.ru

Abstract. We present a model for the time evolution of the shape of a droplet catalyzing the vapor-liquid-solid growth of III-V semiconductor nanowires under varying group III or group V fluxes. Under the assumption of a constant radius of the nanowire top, the model gives the time dependence of the droplet contact angle. These results can be used for the fine tuning of the droplet shape, which affects the preferred crystal phase (zincblende or wurtzite) of III-V nanowires.

Keywords: Catalyst droplet, vapor-liquid-solid growth, III-V nanowires

1. Introduction

III-V nanowires (NWs) and heterostructures within such NWs [1,2] offer otherwise unattainable functionalities of optoelectronic devices, in particular those monolithically integrated with silicon electronic platform. Very efficient elastic stress relaxation on the NW lateral sidewalls enable dislocation-free growth of lattice-mismatched III-V NW heterostructures [3,4] on silicon substrates [4], which is challenging in planar layers and even quantum dots [5]. Most III-V NWs are obtained via the vapor-liquid-solid (VLS) method [6] with a catalyst droplet promoting the NW growth in vertical direction. Catalyst metals are usually gold [6-10] or a group III metal [11-13] in the self-catalyzed approach. One of the most interesting features of VLS NWs of zincblende (ZB) III-V materials is their ability to form in the wurtzite (WZ) phase (see, for example, Ref. [14] for a review). This ZB-WZ polytypism in III-V NWs has been of great interest for a long time. As a result, several methods have been developed to controllably switch the crystal phase of III-V NWs by the growth parameter tuning, for example, by changing the V/III flux ratio [15]. The so-called crystal phase quantum dots, or ZB/WZ heterostructures have thus become possible, with extremely abrupt interfaces and interesting optical properties [16]. However, some aspects require a deeper understanding, in particular, the role of the droplet contact angle in the crystal phase selection and how the droplet shape changes under varying material fluxes.

The first models of polytypism in III-V NWs were originally developed for vertical facets and planar liquid-solid interface [17-19], which is the natural geometry of VLS NWs. However, more recent *in situ* experimental observations of III-V NW growth in a transmission electron microscope [20-22] revealed the presence of truncated facets at the growth interface of GaP [21] and GaAs [22] NWs. It has been shown that the morphology of gold-catalyzed GaAs NWs critically depends on the contact angle of the catalyst droplet, with the growth front being planar at smaller and truncated at larger contact angles [22]. According to Tersoff *et al.* [20,21] the crystal phase of truncated III-V NWs should be pure ZB. This is related to the stability of truncated facet such that new islands nucleate at the liquid-solid

http://dx.doi.org/10.18720/MPM.4232019_1

© 2019, Peter the Great St. Petersburg Polytechnic University

© 2019, Institute of Problems of Mechanical Engineering RAS

interface rather than at the triple phase line where the vapor, liquid and solid phases meet. Nucleation at the triple phase line is indeed the necessary condition for the WZ phase formation according to Glas *et al.* [17]. This explains the importance of the contact angle, which is currently considered as the most important parameter controlling the crystal phase selection in III-V NWs [22,23].

We have recently presented a stationary model for the droplet shape under different group III and V fluxes [24]. Here, we develop a non-stationary generalization of the model which yields the time dependence of the droplet contact angle under varying material fluxes.

2. Model

Let us consider the most general case of a ternary Au-III-V droplet catalyzing the VLS growth of a binary III-V NW. Introducing the numbers N_k of group III ($k = 3$), group V ($k = 5$) and gold ($k = Au$) atoms in the liquid droplet, their sum is related to the radius of the NW top R and the contact angle of the droplet β as

$$N_3(t) + N_5(t) + N_{Au} = \frac{\pi R^3(t)}{3\Omega_L} f[\beta(t)]. \quad (1)$$

Here, Ω_L is the average elementary volume per atom in the liquid phase ($\Omega_L \cong 0.02 \text{ nm}^3$ for Au-Ga-As alloy [2]) and

$$f(\beta) = \frac{(1 - \cos \beta)(2 + \cos \beta)}{(1 + \cos \beta) \sin \beta} \quad (2)$$

is the geometrical function of the contact angle. These expressions are written for cylindrical NW and spherical cap droplet seated on the NW top. According to Eq. (1), the number of gold atoms in the droplet is fixed ($N_{Au} = const$), while both N_3 and N_5 can change with time, leading to the time dependence of the NW top radius R , or the contact angle β , or both R and β in the general case.

Assuming that (i) the number of group III atoms in the droplet changes in time due to the direct impingement flux and NW growth, without surface diffusion from the NW sidewalls [2,9], (ii) there is no desorption of group III atoms from the droplet at a growth temperature, and (iii) the NW growth is mononuclear [2,14,17,18], the kinetic equations describing the time evolution of N_3 and N_5 are given by [2,24]:

$$\frac{dN_3}{dt} = \frac{\pi R^2}{\Omega_s} [\chi_3(t)v_3(t) - \pi R^2 h J(t)], \quad (3)$$

$$\frac{dN_5}{dt} = \frac{\pi R^2}{\Omega_s} \left[\chi_5(t)v_5(t) - \frac{2}{[1 + \cos \beta(t)]} v_5^{des} \exp(n\mu_5) - \pi R^2 h J(t) \right]. \quad (4)$$

Here, Ω_s is elementary volume per III-V pair in the solid phase ($\Omega_s = 0.0452 \text{ nm}^3$ for ZB GaAs [14]), $\chi_k(\beta)$ are the geometrical coefficients ($\chi_k = 2/(1 + \cos \beta)$ for both growth species in vapor deposition techniques, while in the directional deposition methods such as molecular beam epitaxy they are given in Ref. [25]), $v_k(t)$ are the time-dependent vapor fluxes, including possible re-emission (in nm/s), h is the height of a monolayer ($h = 0.326 \text{ nm}$ for ZB GaAs [14] growing in $\langle 111 \rangle$ direction), v_5^{des} is the pre-exponent of the desorption term for group V atoms, μ_5 is the chemical potential of group V atoms in the liquid phase in thermal units, and $n = 2$ is group V atoms desorb as dimers (As_2 or P_2). The $J(t)$ is the nucleation rate of two-dimensional islands on the NW top facet [in $1/(\text{nm}^2\text{s})$] (Refs. [2,24]).

For large enough β or small incident angles of the group III and V beams with respect to the vertical, the result of Ref. [25] for χ_k is reduced to $\chi_k = 1/\sin^2(\beta)$ for both growth species.

Very important results of Ref. [26] revealed the existence of the two stable contact angles of self-catalyzed GaAs NWs, one around 90-95° and the other around 130°, corresponding to the NW growth with shrinking or extending the top radius. Between these two stable angles, the droplet changes its volume by changing the contact angle at a constant top radius, corresponding to $R = const$ in Eqs. (3) and (4). A time-independent radius should be even more usual in the case of gold-catalyzed VLS growth [2]. Treating Eqs. (3) and (4) at $R = const$, using Eq. (1) under the standard condition $N_5 \ll N_3$ (Refs. [2,14,24]) and Eq. (2), we can relate dN_3/dt to $d\beta/dt$ according to

$$\frac{dN_3}{dt} = \frac{\pi R^3}{\Omega_L} \frac{1}{(1 + \cos \beta)^2} \frac{d\beta}{dt}. \quad (5)$$

The time-dependent nucleation rate can be presented in the form [27-29]

$$J(t) = J_* \exp\left[-\frac{A}{\Delta\mu(t)}\right]. \quad (6)$$

Here, A is the dimensionless surface energy of two-dimensional island and $\Delta\mu$ is the time-dependent chemical potential of III-V pair in liquid with respect to the reference solid state. The pre-exponential factor J_* can be treated as composition-independent in the first approximation. The $\Delta\mu$ is defined as [24]

$$\Delta\mu(t) = \mu_3(t) + \mu_5(t) - \mu_{35}^0, \quad (7)$$

with μ_{35}^0 as the chemical potential of solid and μ_k as the concentration-dependent chemical potentials of group III and V atoms in liquid.

Chemical potentials in liquid are calculated within the regular solution model omitting the power terms with $c_k \ll 1$ [24]

$$\begin{aligned} \mu_3(t) &= \mu_3^0 + \ln[c_3(t)] + \omega_{3Au}[1 - c_3(t)]^2, \\ \mu_5(t) &= \mu_5^0 + \ln[c_5(t)] + \omega_{35}c_3^2(t) + \omega_{5Au}[1 - c_3(t)]^2 + (\omega_{35} + \omega_{5Au} - \omega_{3Au})c_3(t)[1 - c_3(t)], \end{aligned} \quad (8)$$

with the atomic concentrations $c_k = N_k/(N_3 + N_5 + N_{Au}) \cong N_k/(N_3 + N_{Au})$ for $k = 3$ and 5 . Here, μ_k^0 are chemical potentials of pure liquids and ω_{ik} are the binary interaction constants (in thermal units). In calculations, we use the parameters of gold-catalyzed GaAs NWs summarized in Table 1, for a typical growth temperature of 500 °C [30]. The A value corresponds to the effective surface energy of two-dimensional island $\gamma_{eff} = 0.23$ J/m², with regular triangle shape [17,18]. The $\Delta\mu_{GaAs}^0$ is defined according to $\Delta\mu_{GaAs}^0 = \mu_{Ga}^0 + \mu_{As}^0 - \mu_{GaAs}^0$. Now, Eqs. (3) to (8) constitute the closed system for finding the time-dependent droplet composition and contact angle under the given fluxes $v_3(t)$ and $v_5(t)$. This system can only be solved numerically; analytical approximations for the solutions will be considered elsewhere.

Table 1. Parameters of Au-Ga-As system used in calculations

ω_{GaAs}	ω_{GaAu}	ω_{AsAu}	$\Delta\mu_{GaAs}^0$	γ_{eff} (J/m ²)	A	v_{As}^{des} (nm/s)	J_* (1/nm ² s)
-4.488	-9.517	1.101	11.80	0.23	14.6	37000	23 000

3. Results and discussion

Figure 1 shows the time evolution of the droplet contact angle from the initial value of 90° , obtained by numerically solving the model equations at a fixed $v_5 - v_3 = 3$ nm/s, two different $v_3 = 0.5$ nm/s and 1.5 nm/s, and three different GaAs NW radii $R = 20, 40,$ and 80 nm, for the parameters of GaAs NWs given in Table 1. Both gallium and arsenic fluxes are turned on at $t = 0$. In the considered range of gallium fluxes, the stationary contact angle ranges between ~ 115 and $\sim 120^\circ$. For a given gallium flux, saturation to the stationary value takes longer time for thicker NWs, which is explained by a larger reservoir effect in larger droplets. Increasing v_3 at a fixed $v_5 - v_3$ is equivalent to decreasing the V/III flux ratio v_5/v_3 , and yields larger stationary contact angles. For a given NW radius, higher gallium flux v_3 leads to a much faster increase of the contact angle and its saturation to the stationary value. This conclusion seems plausible, because inputting gallium at a higher rate should lead to a more rapid swelling of the droplet.

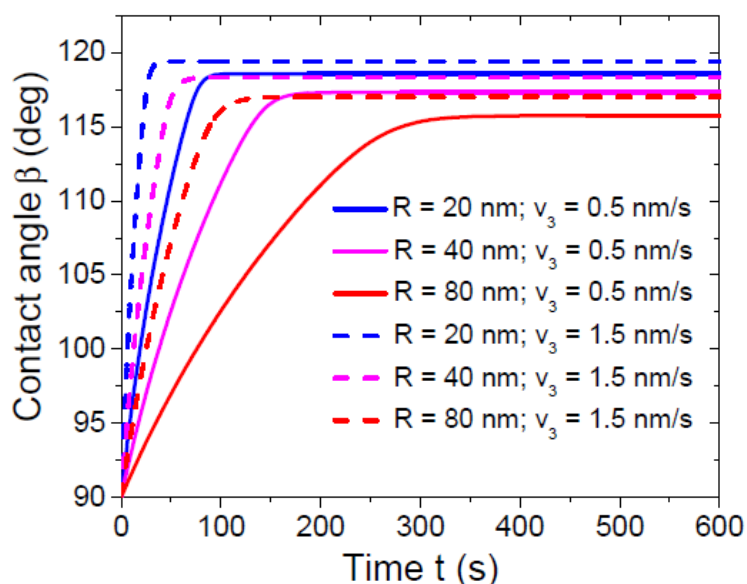


Fig. 1. Time evolution of the droplet contact angle from the initial state $\beta = 90^\circ$ at $t = 0$, after switching the material fluxes v_3 and v_5 . The difference $v_5 - v_3$ is fixed at 3 nm/s. The gallium fluxes v_3 and the NW radii R are given in the legend

Figure 2 shows a more interesting situation where one of the material fluxes is changed abruptly during the NW growth. Such a procedure is used during *in situ* growth monitoring in a transmission electron microscope to investigate the crystal phase selection in GaAs NWs as a function of the contact angle [22]. In the first case (loop (a) in Fig. 2), the gallium flux is fixed at 4.5 nm/s, while the arsenic flux is changed abruptly from 8.5 nm/s to either 19.5 nm/s or 6.0 nm/s, and returned to its initial value after 40 s. As expected, increase (decrease) of the arsenic flux leads to a rapid decrease (increase) of the contact angle. However, the shapes of the corresponding curves are not symmetric. In the second case (loop (b) in Fig. 2), the arsenic flux is fixed at 8.5 nm/s, while the gallium flux is changed abruptly from 4.5 nm/s to either 6.5 nm/s or 0.5 nm/s, and returned to its initial value after 86 s. Increase (decrease) of the gallium flux leads to an increase (decrease) of the contact angle. The droplet shape changes slower than under varying arsenic flux, while the shapes of the two curves becomes more symmetric compared to the first case. We note that even with these large values of material fluxes (which are more typical deposition techniques), the droplet contact angle can

only be tuned within a narrow range of 113-120°. This may suggest a strong influence of re-emitted species [28] and in any case requires further study. The curves shown in Fig. 2 clearly demonstrate that a very similar effect on the droplet contact angle can be achieved by modifying either group V or group III flux.

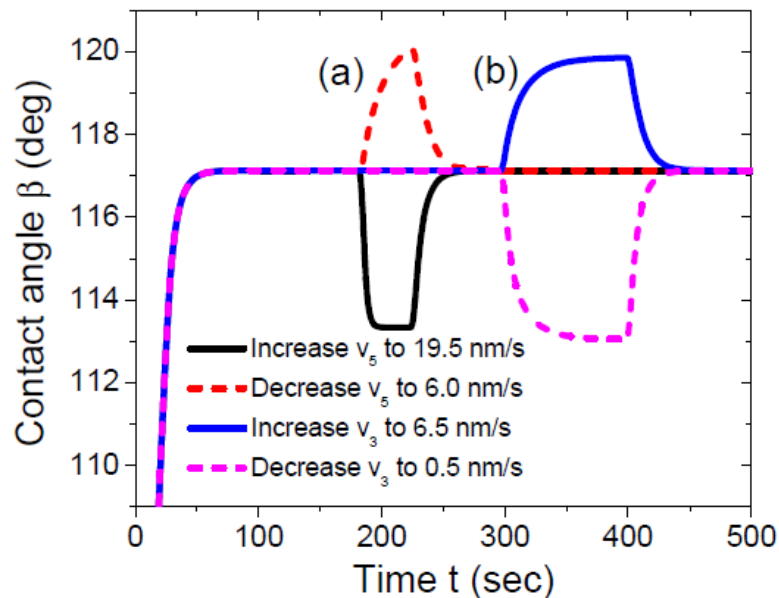


Fig. 2. Contact angle versus time at (a) variable v_5 which is changed abruptly from $v_5^0 = 8.5$ nm/s to 19.5 nm/s (solid line) or 6.0 nm/s (dashed line) for 40 s and then returned abruptly to its initial value, at a fixed $v_3^0 = 4.5$ nm/s; and (b) variable v_3 which is changed abruptly from $v_3^0 = 4.5$ nm/s to 6.5 nm/s (solid line) or 0.5 nm/s (dashed line) for 86 s and then returned abruptly to its initial value, at a fixed $v_5^0 = 8.5$ nm/s. The value R of GaAs NW radius is fixed at 20 nm

In conclusion, we have presented a model for non-stationary droplet shape during the VLS growth of III-V NWs under varying materials inputs. It captures the main ingredients of this non-stationary process, including the ability to quickly inflate or shrink the droplet by abruptly changing one of the two material fluxes, and then retain its initial shape. This can be very useful for understanding and controlling the crystal phase switching of GaAs and other III-V NWs, and possibly to minimize the faulted polytypic regions in the WZ-to-ZB phase transitions. We now plan to model the experimentally measured shapes of the droplet within the frame of the model.

Acknowledgements. The authors thank the Russian Science Foundation for financial support under the Grant 19-72-30004.

References

- [1] Zhang A, Zheng G, Lieber CM. *Nanowires: Building blocks for nanoscience and nanotechnology*. Springer; 2016.
- [2] Dubrovskii VG. Theory of VLS growth of compound semiconductors. In: Morral AF, Dayeh SA, Jagadish C. (eds.) *Semiconductor Nanowires I: Growth and Theory, Volume 93*. 1st ed. Burlington: Academic Press; 2015. p.1-78.
- [3] Glas F. Critical dimensions for the plastic relaxation of strained axial heterostructures in free-standing nanowires. *Physical Review B*. 2006;74(12): 121302 (R).

- [4] Ng KW, Ko WS, Tran TTD, Chen R, Nazarenko MV, Lu F, Dubrovskii VG, Kamp M, Forchel A, Chang-Hasnain CJ. Unconventional growth mechanism for monolithic integration of III–V on silicon. *ACS Nano*. 2013;7(1): 100-107.
- [5] Cirlin GE, Dubrovskii VG, Petrov VN, Polyakov NK, Korneeva NP, Demidov VN, Golubok AO, Masalov SA, Kurochkin DV, Gorbenko OM, Komyak NI, Ustinov VM, Egorov AY, Kovsh AR, Maximov MV, Tsatusul'nikov AF, Volovik BV, Zhukov AE, Kop'ev PS, Alferov ZI, Ledentsov NN, Grundmann M, Bimberg D. Formation of InAs quantum dots on a silicon (100) surface. *Semiconductor Science & Technology*. 1998;13(1): 1262-1265.
- [6] Wagner RS, Ellis WC. Vapor liquid solid mechanism of single crystal growth. *Applied Physics Letters*. 1964;4: 89.
- [7] Dubrovskii VG, Sibirev NV, Suris RA, Cirlin GE, Harmand JC, Ustinov VM. Diffusion-controlled growth of semiconductor nanowires: vapor pressure versus high vacuum deposition. *Surface Science*. 2007;601(18): 4395-4401.
- [8] Dubrovskii VG, Sibirev NV, Cirlin GE. Kinetic model of the growth of nanodimensional whiskers by the vapor-liquid-crystal mechanism. *Technical Physics Letters*. 2004;30(8): 682-686.
- [9] Dubrovskii VG, Soshnikov IP, Sibirev NV, Cirlin GE, Ustinov VM. Growth of GaAs nanoscale whiskers by magnetron sputtering deposition. *Journal of Crystal Growth*. 2006;289(1): 31-36.
- [10] Dubrovskii VG, Soshnikov IP, Cirlin GE, Tonkikh AA, Samsonenko YB, Sibirev NV, Ustinov VM. On the non-monotonic lateral size dependence of the height of GaAs nanowhiskers grown by molecular beam epitaxy at high temperature. *Physica Status Solidi B*. 2004;241(7): R30-R33.
- [11] Colombo C, Spirkoska D, Frimmer M, Abstreiter G, Morral AF. Ga-assisted catalyst-free growth mechanism of GaAs nanowires by molecular beam epitaxy. *Physical Review B*. 2008;77(15): 155326.
- [12] Gibson SJ, Boulanger JP, LaPierre RR. Opportunities and pitfalls in patterned self-catalyzed GaAs nanowire growth on silicon. *Semiconductor Science & Technology*. 2013;28(10): 105025.
- [13] Matteini F, Dubrovskii VG, Ruffer D, Tütüncüoğlu G, Fontana Y, Morral AF. Tailoring the diameter and density of self-catalyzed GaAs nanowires on silicon. *Nanotechnology*. 2015;26(10): 105603.
- [14] Dubrovskii VG. *Nucleation theory and growth of nanostructures*. Berlin: Springer; 2014.
- [15] Dheeraj DL, Munshi AM, Scheffler M, Van Helvoort ATJ, Weman H, Fimland BO. Controlling crystal phases in GaAs nanowires grown by Au-assisted molecular beam epitaxy. *Nanotechnology*. 2013;24(1): 015601.
- [16] Akopian N, Patriarche G, Liu L, Harmand JC, Zwiller V. Crystal phase quantum dots. *Nano Letters*. 2010;10(4): 1198–1201.
- [17] Glas F, Harmand JC, Patriarche G. Why does wurtzite form in nanowires of III-V zinc-blende semiconductors? *Physical Review Letters*. 2007;99(14): 146101.
- [18] Dubrovskii VG, Sibirev NV, Harmand JC, Glas F. Growth kinetics and crystal structure of semiconductor nanowires. *Physical Review B*. 2008;78(23): 235301.
- [19] Johansson J, Karlsson LS, Dick KA, Bolinsson J, Wacaser BA, Deppert K, Samuelson L. Effects of supersaturation on the crystal structure of gold seeded III–V nanowires. *Crystal Growth & Design*. 2009;9(2): 766-773.
- [20] Ross FM. Controlling nanowire structures through real time growth studies. *Reports on Progress in Physics*. 2010;73(11): 114501.

- [21] Wen CY, Tersoff J, Hillerich K, Reuter MC, Park JH, Kodambaka S, Stach EA, Ross FM. Periodically changing morphology of the growth interface in Si, Ge, and GaP nanowires. *Physical Review Letters*. 2011;107(2): 025503.
- [22] Jacobsson D, Panciera F, Tersoff J, Reuter MC, Lehmann S, Hofmann S, Dick KA, Ross FM. Interface dynamics and crystal phase switching in GaAs nanowires. *Nature*. 2016;531: 317-322.
- [23] Dubrovskii, VG. Development of growth theory for vapor-liquid-solid nanowires: contact angle, truncated facets and crystal phase. *Crystal Growth & Design*. 2017;17(5): 2544-2548.
- [24] Dubrovskii VG, Sokolova ZV, Rylkova MV, Zhiglinsky AA. Composition and contact angle of Au-III-V droplets on top of Au-catalyzed III-V nanowires. *Materials Physics and Mechanics*. 2018;36(1): 1-7.
- [25] Glas F. Vapor fluxes on the apical droplet during nanowire growth by molecular beam epitaxy. *Physica Status Solidi B*. 2010;247(2): 254-258.
- [26] Kim W, Dubrovskii VG, Vukajlovic-Plestina J, Tütüncüoğlu G, Francaviglia L, Güniat L, Potts H, Friedl M, Leran JB, Morral AF. Bi-stability of contact angle and its role in achieving quantum-thin self-assisted GaAs nanowires. *Nano Letters*. 2018;18(1): 49-57.
- [27] Dubrovskii VG. Nucleation and growth of adsorbed layer: self-consistent approach based on Kolmogorov-Avrami model. *Physica Status Solidi B*. 1992;171(2): 345-356.
- [28] Glas F, Ramdani MR, Patriarche G, Harmand JC. Predictive modeling of self-catalyzed III-V nanowire growth. *Physical Review B*. 2013;88(19): 195304.
- [29] Dubrovskii, VG, Grecenkov J. Zeldovich nucleation rate, self-consistency renormalization, and crystal phase of Au-catalyzed GaAs nanowires. *Crystal Growth & Design*. 2015;15(1): 340-347.
- [30] Leshchenko ED, Ghasemi M, Dubrovskii VG, Johansson J. Nucleation-limited composition of ternary III-V nanowires forming from quaternary gold based liquid alloys. *CrystEngComm*. 2018;20: 1649-1655.

STUDY OF HEAT DISSIPATING MATERIAL USING BORON NITRIDE FABRICATED BY LASER ABLATION

Atsushi Yamaguchi, Pankaj Koinkar, Akihiro Furube*

Graduate School of Technology, Industrial and Social Sciences, Tokushima University, Tokushima 770-8506,
Japan

*e-mail: furube.akihiro@tokushima-u.ac.jp

Abstract. More research interest is developing rapidly on two dimensional (2D) materials owing to their excellent electro-optic properties to develop next generation of electronics and highly functional devices. Among well-known and widely used 2D materials, boron nitride (BN) is an electrical insulator with a band gap of 5.5 eV, and attests high chemical stability, outstanding mechanical properties, and high thermal conductivity. Accordingly, BN is considered as a promising candidate to improve the heat dissipation material performance. In this study, the cooling rate of composite materials of poly methyl methacrylate (PMMA), hexagonal boron nitride (h-BN) and gold nanoparticles was investigated using femtosecond transient absorption spectroscopy. The main objective of this study is to prepare the flexible BN-PMMA films could have a significant impact on heat dissipation to enhance the performance of electronics devices. BN nanostructures were prepared by nanosecond laser ablation in acetone. The laser ablation was carried out at room temperature with laser ablation time of 120 min. The SEM images of bulk BN and laser ablated BN were obtained for structural and surface morphological characterization. Gold colloidal solution was prepared using gold nano-particles with chloroauric acid and distilled water. For the preparation of composite film, PMMA was dissolved in acetone solvent and then mixed with BN and gold colloid solution. The prepared composite films were examined for cooling rate of photoexcited gold nanoparticles using femtosecond transient absorption spectroscopy. It is found that the lifetime is shorter for composite films with Au and high BN content.

Keywords: boron nitride, laser ablation, X-ray diffraction, raman spectroscopy, scanning electron microscopy, cooling process, transient absorption spectroscopy (TAS)

1. Introduction

During the past few years, (2D) materials have received a great deal of interest due to their wide application in micro and nano optoelectronics, photocatalysis and energy conversion device. Significant progress has been achieved in preparation of 2D materials using various synthesis methods such as mechanical exfoliation, chemical exfoliation and hydrothermal or solvothermal reactions, and chemical vapor deposition. These techniques are very effective to fabricate high quality nanosheets with limited efficiency [1-3]. A widely used 2D form of carbon is called as graphene. Graphene is well-known and one of the most extensively studied materials because of its fascinating physical and chemical properties [4-6]. It can be exfoliated from graphite. Graphite, a base material for graphene, is relatively low cost and widely used in our daily life such as lead of pencil. In the same way, besides graphene, atomically thin transition-metal dichalcogenides (TMDs) also attracts enormous attention all over the world [7]. TMDs layered materials such as Molybdenum sulfide (MoS_2), Tungsten

sulfide (WS_2) and Boron nitride (BN) exhibits unique features and characteristics, establishing their significance in opto-electronic devices and applications. BN nanostructure has greatly shown its potentials for applications in high performance devices like electron devices, gas absorbents and reinforcing agents [8]. BN can be found in two forms; hexagonal BN (h-BN) and cubic BN (c-BN). Among these, h-BN having similar structure to graphite is new material for research as compared to widely studied c-BN. The h-BN is now widely used in study. Recently, success in synthesis of Boron nitride nanotube (BNNT) has gaining much attention because of their physicochemical properties. BNNT has similar nanostructure to that of carbon nanotube (CNT) where boron and nitrogen atoms are arranged in hexagonal network. BNNT displays comparable or even better characteristics as compared to CNT and is considered as a promising material for strengthening polymers, ceramics and metals because of it has high rigidity and high chemical stability. It also exhibits superior properties like antioxidant power and heat resistance, it is hard to oxidize up to 950°C and structurally stable up to 900°C . It is reported that the h-BN can change to BNNTS and C-BN by using laser ablation [2]. In the last decade, there have been few reports on the alternative routes for the preparation of BN using the polymer as a precursor. In this context, few reports suggest that poly methyl methacrylate (PMMA) and poly-styrene (PS) can be used as precursor to synthesis BN-polymer composite film [3]. When BN coated with polymer, it shows improvement in the properties such as thermal conductivity and mechanical strength due to the interfacial adhesion in the composite films. Furthermore, previous reports suggest that the fabrication of new functional material combined with 2D materials and metal nanoparticle. The formation of new composite materials exhibits superior performance as compared to noble metal nanoparticle because of excellent characteristic of 2D material, the obtained large surface area, chemical stability and prevention of aggregation of nanoparticles. Also, composite material of graphene and gold nanoparticle is emerging as a material with future potential for high sensitivity electrochemical sensor [9-10]. In addition, composite material like Au nanoparticle modified with of MoS_2 nanostructure can be possible serve as an active substrate to produce enhanced light absorption [11]. Most recently, advancement in information and communication technologies accelerates the research activities for the production of innovative machines and devices. This creates increase in the demands of electronic parts such as CPU and memory. For the development of flexible electronic devices, a flexible material with superior heat dissipation are needed around the world [12]. The heat released from smaller electronic devices could alter the performance which results in overheat or explosion. The heat dissipation is one factor which limits to develop electronic devices such as mobile phones and batteries. Since BN produces high thermal conductivity, it can be effectively used to control heat dissipation. Therefore, it is thought that BN could be considered as promising material to control heat dissipation to make smaller devices cooler and safer without causing damage. In the present work, we have prepared composite film of BN with flexible PMMA and Au nanoparticle. The cooling process of BN and polymer composite films were studied using femtosecond transient absorption spectroscopy.

2. Experimental

Chemicals and Materials. Chemicals and materials used were purchased and used as received; BN powder (Wako Chemical Japan), $H AuCl_4 \cdot 4H_2O$ ($0.1 \text{ ml } 2.5 \times 10^{-5} \text{ mol}$) (Kishida Chemical, Japan, 99.0 %), $Na_3C_6H_5O_7$ (Kanto Chemical, Japan: $0.100 \text{ g } /10 \text{ ml}$, $294.1 \text{ g } /\text{mol}$), Poly-methylmetaclyl-acid (PMMA), Acetone (Kishida Chemical, Japan: 99.5%)

Preparation of 40 nm diameter gold nanoparticles by chemical synthesis. Gold nanoparticles are synthesized by the chemical method. $H AuCl_4$ aqueous solution ($0.1 \text{ ml: } 2.5 \times 10^{-5} \text{ mol}$) was added into deionized water (100 ml). The mixture was heated and stirred at 100°C . Then, the $Na_3C_6H_5O_7$ (1 ml) solution was added into the mixture. After the

mixture was stirred at heating for 5 minutes and then kept for cooling at room temperature. Finally, deionized water was added for total volume 100 ml. Au nanoparticle size was determined by the experimentally observed peak position from UV-vis spectra.

Preparation of PMMA–Au–BN nanocomposite. PMMA solution was prepared as follows: 4 g of PMMA ($M_w = 100,000$) was dissolved into 30 ml of Acetone. After this, 1 mg and 5 mg laser ablated BN powder was added into PMMA mixture and stirred for 10 minutes to prepare PMMA-Au-BN solution. Then, PMMA solution was mixed with 13 ml of Au nanoparticle colloid. PMMA-Au-BN nanocomposite film was prepared transferring PMMA-Au-BN solution on glass substrate at room temperature for 3 hours. The PMMA-Au-BN composite film with 1 g of BN and 5 g of Au hereafter referred as sample 1 and sample 2 respectively. The preparation details of sample 1 and 2 is shown in Table 1.

Table 1. Synthesis of BN, PMMA and Au Colloid

Sample	BN (mg)	Au (nm)	BN:Au (Weight ratio)
S1	1	40	16:1
S2	5	40	78:1

Laser Ablation and characterization. The BN nanoparticle was prepared by nanosecond laser ablation using acetone as a solvent. We used analytical grade h-BN powder about 100 mg mixed with 30 mL acetone into a glass bottle. The solution was kept under magnetic stirring for 30 min prior to laser ablation. The laser ablation was carried out with Nd:YAG laser (wavelength 532 nm, pulse duration 10 ns, pulse repetition frequency 10 Hz, beam size 5 mm and laser power 56 mJ). During the laser ablation process, the solution was rotated by magnetic stirrer and laser ablation time was 120 min. After laser ablation, BN colloidal suspension was heated in air to obtain dry BN nanoparticle in the form of powder. The laser ablated BN nanoparticles sample was characterized by X-ray diffraction (XRD) and scanning electron microscopy (SEM) to confirm the formation of nanostructure, surface morphological changes as well as structural features.

Transient Absorption Spectroscopy (TAS) using femtosecond laser (cooling process of Au nanoparticle). Cooling process of the PMMA-Au-BN film was investigated using femtosecond transient absorption spectroscopy. The measurements were carried out with an amplified Ti:sapphire laser (800 nm wavelength, 130 fs fwhm pulse width, 0.8 mJ/pulse intensity, 1 kHz repetition; Spectra Physics, Hurricane). The second harmonic of 400 nm wavelength at a 500 Hz modulation frequency was used for a pump light. On the other hand, the white-light continuum generated by focusing the fundamental beam from Ti:sapphire laser onto a sapphire plate (2 mm thick) was used for a probe light. The probe light was focused at the center of the pump light (~0.3 mm diameter) on the sample, and the diffuse reflected probe light was detected by a Si photodiode after passing through a monochromator (Acton Research, SpectraPro-150). Au nanoparticle of dispersion including PMMA film was irradiated by the pump light (400 nm). Cooling effect of PMMA film including BN was measured by probe light (850 nm).

3. Results and discussion

The spectroscopic data of bulk BN and laser treated BN were obtained using XRD diffraction, Raman spectroscopy and SEM. Figures 1(a) and 1(b) display the XRD spectra of bulk BN powder and laser-treated BN for 120 min. Figure 1(a) shows that the intensity of the diffraction peak (002) and (004) decreased for laser-treated BN with small shift as compared to the bulk BN. It suggests that the bulk BN has been transformed into h-BN nanostructure after the laser ablation while keeping its crystalline structure unchanged [13]. Figure 1(b)

shows that the intensity of the diffraction peaks (101), (100) and (102) slightly increases. It indicates that the c-BN content is also observed after laser ablation.

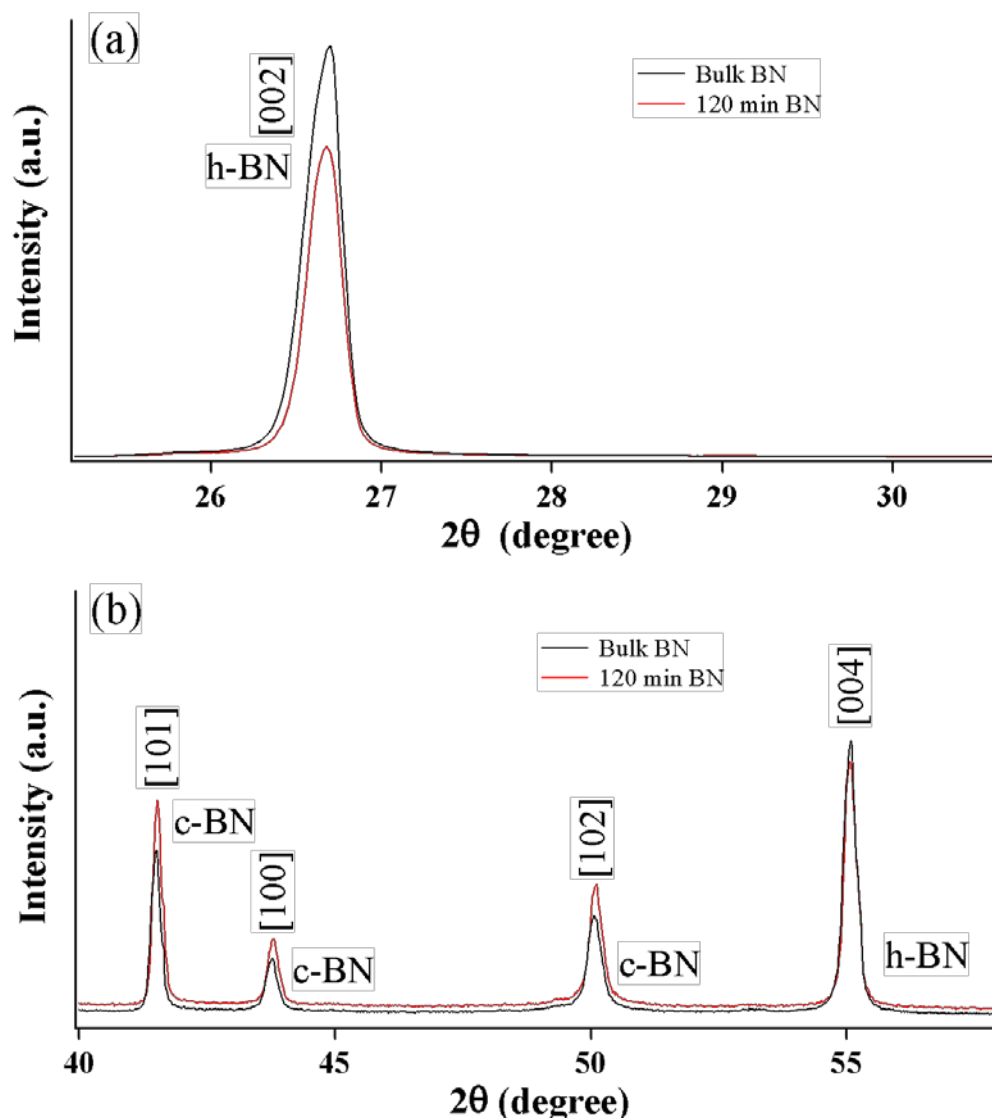


Fig. 1. High resolution XRD spectra of (a) bulk BN powder and (b) laser ablated BN

The raman spectra of bulk BN powder and laser-treated BN for 120 is shown in Fig. 2. In case of laser ablated BN, the spectra graph indicates that the signature peak assigned to h-BN is observed at 1364.4 cm^{-1} [7,14]. The increase in the intensity of peak at 1364.4 cm^{-1} confirms that h-BN nanostructure was still unchanged after the laser ablation.

Figure 3 illustrates SEM images of bulk BN powder and laser ablated BN for 120 min. The SEM images show the formation of BN nanostructures upon laser ablation. Figure 3 (a) shows that the BN sheets having the diameter varies from $2\text{ }\mu\text{m}$ to $10\text{ }\mu\text{m}$. In the case of laser ablated BN sample, the formation of nanoparticle is observed with diameter of 30-70 nm and the transformation of bulk BN powder into BN nanostructure might be due to the intense thermal activity produced during laser ablation.

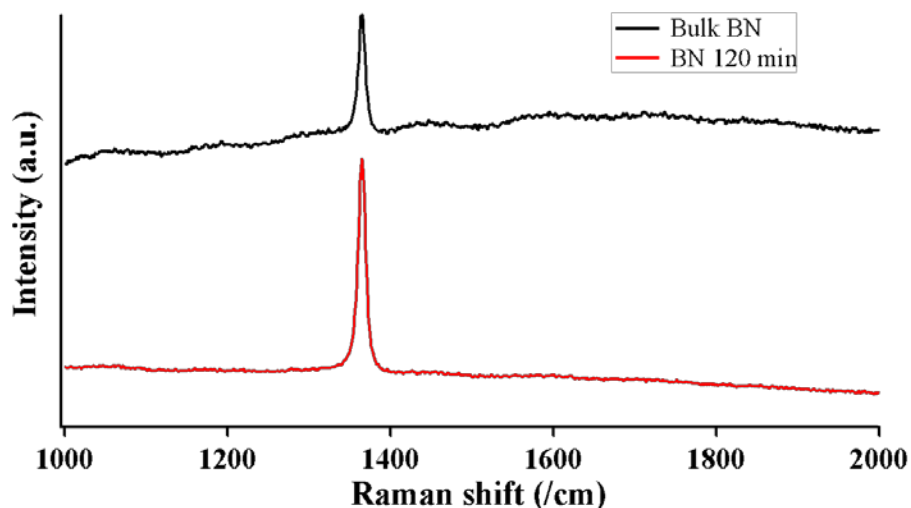


Fig. 2. Raman spectra of laser ablated BN

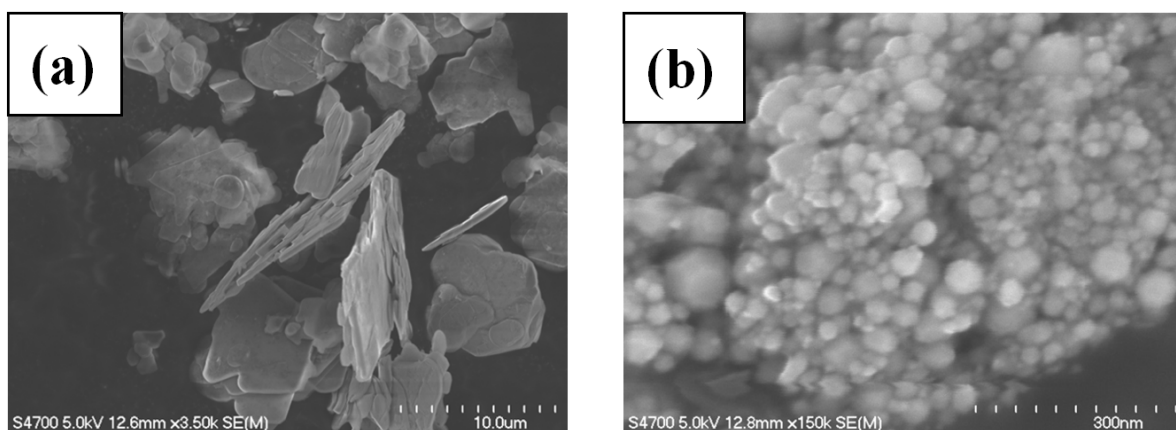


Fig. 3. SEM images of (a) Bulk BN, (b) 120 min laser ablated BN

Figure 4 shows the UV-vis reflection spectra results of PMMA film, sample S1 and sample S2. The reflectances of sample S1 and sample S2 are noticeably lower around 550 to 570 nm, extending toward longer wavelength around 800 nm as compared to the nearly constant reflectance of PMMA film. This lowering in the reflectance might be attributed to aggregation of Au nanoparticle in sample S1 and sample S2, because non-aggregated Au nanoparticles could not show such a broad absorption band.

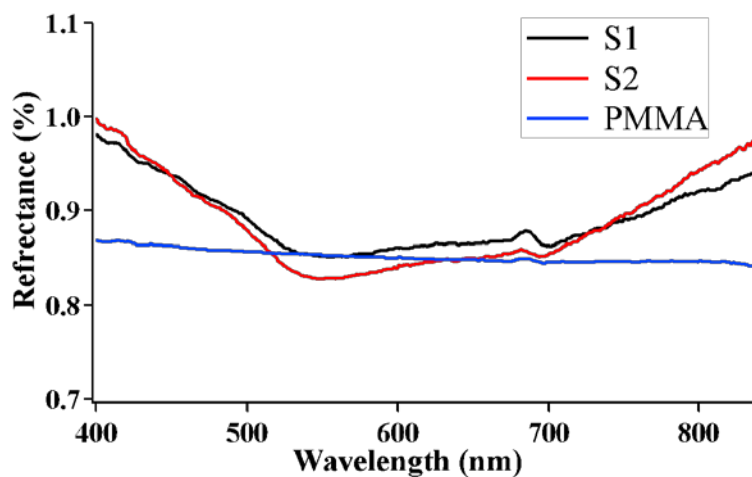


Fig. 4. Reflection spectra images of PMMA and Au-BN-PMMA composite films

Figure 5 shows that transient absorption spectroscopy (TAS) using femto second laser (Probe light: 850 nm, Excitation light intensity: 3.0 mW). The summary of sample lifetime is shown in Table 2 from TAS measurement fitting graph result.

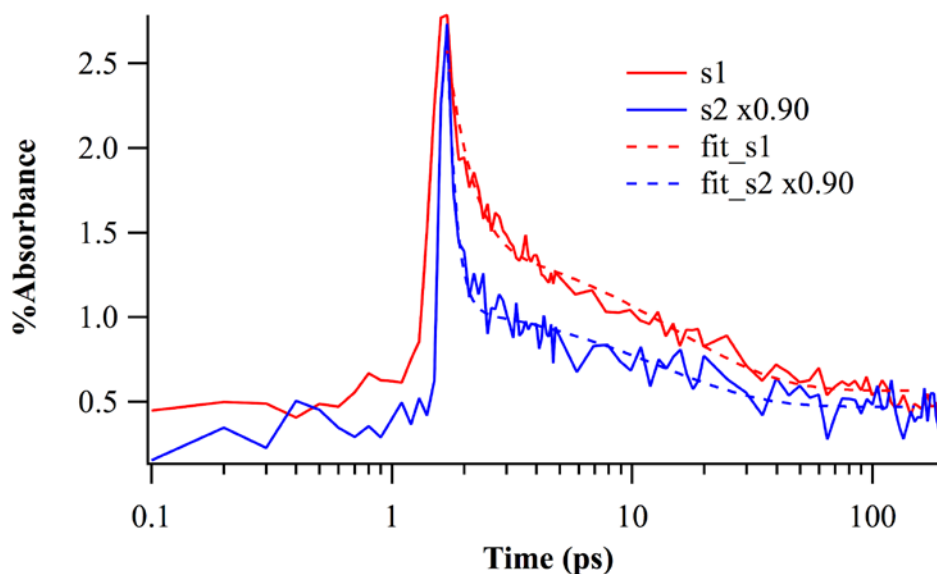


Fig. 5. TAS measurement of PMMA films including BN and Au

Cooling process of Au nanoparticle by photoexcitation was observed as reported previously [15]. 400 nm excitation generates electron-hole pairs in the Au nanoparticle and electron-electron scattering elevates the electron temperature within 100 fs. Thermal equilibrium process happens by electron phonon scattering of the internal Au nanoparticle from 100 fs to 1 ps. Thermal diffusion process happens by Au phonon – media phonon scattering from 10 ps to 100 ps. It is seen that heat transfer occurs from Au nanoparticle to circumference medium.

Table 2. Summary of lifetime of sample S1 and S2

Sample	tau 1	tau 2
S1	0.45591 ± 0.0504	15.396 ± 1.6
S2	0.15535 ± 0.0186	13.064 ± 2.23

Long wavelength area of plasmon band became broader by photoexcitation and the effect was observed in this transient absorption experiment of using probe light of 850 nm. Here the growth and decay of the transient signals correspond to temperature increase and decrease. Figure 4 shows that sample including low BN (sample S1) has long lifetime better than sample including more BN (sample S2) (see tau 2 vales in Table 2). That is, cooling process of Au nanoparticle after photoexcitation of including more BN is promoted by the effect of efficient heat transfer property of BN.

4. Conclusions

We have successfully prepared the BN nanostructures using nanosecond laser ablation in acetone. The formation of BN nanostructure was confirmed by XRD, raman spectroscopy and SEM measurements. We prepared to PMMA composite films with the laser ablated BN and Au nanoparticle of a 40 nm diameter. The cooling process after exciting the Au nanoparticles in the film was examined using femtosecond transient absorption spectroscopy and the effect of BN as an efficient heat dissipater was observed. Heat dissipation performance from BN

could play a crucial role in energy saving and enhance the overall performance of electronic devices. Therefore, it is recommended that further research on heat dissipation is important to resolve a major challenge of high-temperature rise during the process which reduces the efficiency of future generation flexible electronic devices.

Acknowledgements. *The authors sincerely acknowledge the cooperation and experimental facilities provided by Prof. Shuichi Hashimoto, Prof. Toshihiro Moriga and Dr. Kei-ichiro Murai, from Tokushima University, Japan.*

Reference

- [1] Zhang X, Lian G, Zhang S, Cui D, Wang Q. Boron nitride nanocarpets: controllable synthesis and their adsorption performance to organic pollutants. *Cryst. Eng. Comm.* 2012;14: 4670-4676.
- [2] Nistor LC, Epurescu G, Dinescu M, Dinescu G. Boron nitride nano-structures produced by pulsed laser ablation in acetone. *IOP Conf. Series: Materials Science and Engineering.* 2010;15: 012067.
- [3] Yu J, Li J, Zhang W, Chang H. Synthesis of high quality two-dimensional materials via chemical vapor deposition. *Chem. Sci.* 2015;6: 6705-6716.
- [4] Shao Y, El-Kady MF, Wang LJ, Zhang Q, Li Y, Wang H, Mousavi MF, Kaner RB. Graphene-based materials for flexible supercapacitors. *Chem. Soc. Rev.* 2015;44(11): 3639-3655.
- [5] Zhang LL, Zhao X, Stoller MD, Zhu Y, Ji H, Murali S., Wu Y, Perales S, Clevenger B, Ruoff RS. Highly conductive and porous activated graphene oxide films for high-power supercapacitors. *Nano Lett.* 2012;12(4): 1806-1812.
- [6] Yu A, Roes I, Davies A, Chen Z. Ultrathin, transparent, and flexible graphene films for supercapacitor application. *Appl. Phys. Lett.* 2010;96(25): 253105.
- [7] Ramirez S, Chan K, Hernandez R, Recinos E., Hernandez E, Salgado R, Khitum AG, Garay JE, Balandin AA. Thermal and magnetic properties of nanostructured densified ferromagnetic composites with graphene-graphite fillers. *Materials and Design.* 2017;118: 75-80.
- [8] Sainsbury T, Satti A, May P, Wang Z, McGovern I, Gun'ko YK, Coleman J. Oxygen radical functionalization of boron nitride nanosheets. *J. Am. Chem. Soc.* 2012;134(45): 18758-18771.
- [9] Ma X, Chen M. Electrochemical sensor based on graphene doped gold nanoparticles modified electrode for detection of diethylstilbestrol. *Sensors and Actuators.* 2015;B215: 445-450.
- [10] Yola ML, Eren T, Atar N. A sensitive molecular imprinted electrochemical sensor based on gold nanoparticles decorated graphene oxide: Application to selective determination of tyrosine in milk. *Sensors and Actuators B.* 2015;210: 149-157.
- [11] Nistor LC, Epurescu G, Dinescu M, Dinescu G. Effective surface treatments for enhancing the thermal conductivity of bn-filled epoxy composite. *Applied Polymer Science.* 2011;119(6): 3234-3243.
- [12] Goto T, Iida M, Tan H, Liu C, Mayumi K. Thermally conductive tough flexible elastomers as composite of slide-ring materials and surface modified boron nitride particles via plasma in solution. *Applied Physics Letter.* 2018;112(10): 101901.
- [13] Aydin M. Vibrational and electronic properties of single-walled and double-walled boron nitride nanotubes. *Vibrational Spectroscopy.* 2013;66: 30-42.
- [14] Lu J, Ren Q, Sun L, Yu J, Chen Y, Shen X, Chen Z. Temperature-dependent raman spectra of bamboo-like boron nitride nanotubes. *Applied Physics Express.* 2014;7(2): 022401.

[15] Link S, Furube A, Mohamed MB, Asahi T, Masuhara H, El-Sayed MA. Hot Electron relaxation dynamics of gold nanoparticles embedded in mgso_4 powder compared to solution: The effect of the surrounding medium. *J. Phys. Chem.* 2002;106(5): 945-955.

COMPARATIVE STUDY OF ADSORPTION OF OZONE MOLECULE ON PRISTINE AND SI DOPED SINGLE WALL CARBON NANOTUBE BY DENSITY FUNCTIONAL THEORY

R.G. Atram, M.R. Sonawane*

¹Government Institute of Science, Nagpur 440001, India

*e-mail: smahadev123@gmail.com

Abstract. We report comparative study of ozone adsorption on pristine Single Walled Carbon Nanotube (SWCNT) (8, 0) and Silicon doped Single walled Carbon Nanotube (Si – SWCNT) by density functional theory calculations based on DeMol3 code. Importance is given to the effects of silicon doping in carbon nanotube for comparative study of adsorption of ozone. The results show that silicon doping keeps the semiconducting character of pure carbon nanotubes with reduction in band gap from 0.71 eV to 0.54 eV. The ozone gas molecule is physisorbed with binding energy 0.431eV and minute charge transfer of 0.013 e from pure carbon nanotube, consistent with the strong oxidizing nature of ozone. The binding energy and charge transfer indicate that the ozone adsorption on pure carbon nanotube is gentle and reversible. However, when ozone adsorbs on silicon doped carbon nanotube, a strong chemisorption occurs, leading to relevant structural relaxations and to the formation of a Si-O σ bond with binding energy 3.902 eV and charge transfer of 0.252 e. The band structure and density of states shows that the occupancy state in valence band near Fermi energy is completely altered due to ozone adsorption. The charge density analysis also shows formation of sigma bond between silicon and oxygen atoms. The charge density iso-surface shows the oxidation of silicon atom and dissociation of ozone molecule into silicon - oxide and releasing of oxygen molecule.

Keywords: CNT, Si-CNT, DFT, ozone, adsorption

1. Introduction

Carbon nanotubes (CNT) [1] have been intensively studied due to their unique geometrical, mechanical [2], chemical [3] and electrical [4] properties. Their electronic properties can vary from semiconducting to metallic depending on its molecular structure. The latest research efforts have aimed to improve both efficiency and selectivity of nanotube. More attention has been given, experimentally as well as theoretically to study electronic, thermal properties and their chemical reactivity [5–7]. These outstanding properties exhibited by carbon nanotubes have been made it suitable for applications in nanoelectronics [8], catalysis [9,10], sensors [11,12], energy capacitors and hydrogen storage devices [13].

To achieve the enviable results, many research works have been done on the characterization of nanotube, for example, the modification for the properties of nanotube by adsorption of atoms, molecules or clusters on the exterior walls of carbon nanotubes or by insertion of these species into their hollow interior. This offers a promising way in the design of new nanomaterials [14–16]. Furthermore, carbon nanotubes were exposed to several different gas molecules such as NO₂, O₂, and NH₃ [17,18] and observed the change in the electrical resistance. They have also shown that these molecules are weakly adsorbed on pure CNT due

http://dx.doi.org/10.18720/MPM.4232019_3

© 2019, Peter the Great St. Petersburg Polytechnic University

© 2019, Institute of Problems of Mechanical Engineering RAS

to van der Waal interactions. To improve the functionalization, many research groups are now using chemical doping, local defects, radial deformation and metal assistance [19,20]. The metal assistance is an effective way to functionalize the carbon nanotubes which significantly improves the structural and electronic properties.

Ozone interaction with carbon nanotubes has been studied experimentally [21-23] and theoretically [24,25]. More recently, it has been observed that ozone can react with the surface at defect sites [26]. It can also attack the more reactive end cap, opening it up and making it possible for the physical adsorption of other gases [27]. Ozonolysis can oxidize carbon-carbon double bonds of CNT. It is also observed that ozone exposure induces p-type doping and correspondingly reduces resistance in CNTs. [22,23]. Theoretical studies have shown that the binding energy of ozone on CNT is near about 0.3 eV depending on geometrical variation [22-25]. Since the binding energy was too small to explain ozone exposure effect on the CNT resistance. It was shown that some defects sites would be responsible for the ozone adsorption and the corresponding resistance change [22]. However, side wall defects are generally hard to detect experimentally. It was noticed that carbon nanotubes becoming gradually thicker could be attributed to a large number of defects accidentally, thus resulting in a diameter increase [28]. All above literature survey indicates that the understanding on the ozone interaction with CNT is not well established till today. Latest theoretical investigation shows that the Ozone can react chemically on (6, 6) and (8, 8) carbon nanotube but with less binding energy [29].

Despite these important contributions, the detailed adsorption mechanism of ozone on the CNTs is still less known and to the best of our knowledge; there is no report on the interaction of ozone molecules on Silicon doped carbon nanotube (Si-CNT). Here we performed extensive DFT calculations and studied the interactions of ozone with the semiconducting CNT and Si-CNT using electronic properties like binding energy, band structure, density of states and population analysis and compared adsorption nature on CNT and Si-CNT.

2. Computational Details

Calculations were performed using an all-electron linear combination of atomic orbital density functional theory (DFT) approach, implemented in DMol³ [30,31] code within the generalized gradient approximation (GGA) and with the Perdew, Burke and Ernzerhof (PBE) correlation functional [32]. The chosen basis set was double numerical plus polarization (DNP), where each basis function was restricted to a global cut-off radius of 4.0 Å. The chosen cut-off value leads to atomic energies with an accuracy of 0.1 eV/atom, allowing calculations without significant loss of accuracy. The Brillouin zone k-point sampling was performed in a 1 x 1 x 2 Monkhorst–Pack mesh [33]. The all calculations were performed using periodic boundary conditions with 64-atoms within the supercell. The tetragonal unit cell of 20 x 20 x 8.4 Å dimension with lateral separation of 13.7 Å between tubes was used. This separation is sufficiently large to avoid interaction between the neighboring cells. The Mulliken population analysis was carried out to predict the charge transfer between molecule and nanotubes.

In this study, we used an (8, 0) zigzag CNT and Si-CNT of diameter 6.26 Å as a model to study the adsorption of ozone molecule. We have examined four different possible adsorption sites such as 'target C atom \ Si atom', 'chiral bond', 'axial bond' and 'centroid of hexagon' of CNTs. In all calculations, the nanotubes and isolated ozone molecule were first optimized to minimize their total energies. Further, ozone molecule is kept at four different adsorption sites as mentioned above on each of these individual nanotubes and optimized together to get lowest energy stable structure. The binding energy (E_b) of all ground state structures are calculated by $E_b = - [E_T (\text{adsorbent} + \text{adsorbate}) - E_T (\text{adsorbent}) - E_T (\text{adsorbate})]$, where

$E_{T(\text{adsorbent} + \text{adsorbate})}$ denotes the total energy of molecule and CNT system, $E_{T(\text{adsorbent})}$ denotes the total energy of CNT and $E_{T(\text{adsorbate})}$ is the total energy of isolated gas molecule. To verify the computational accuracy of the model, we have calculated the binding energy of CNTs, density of states and the band gap which are comparable to reported results [34,35].

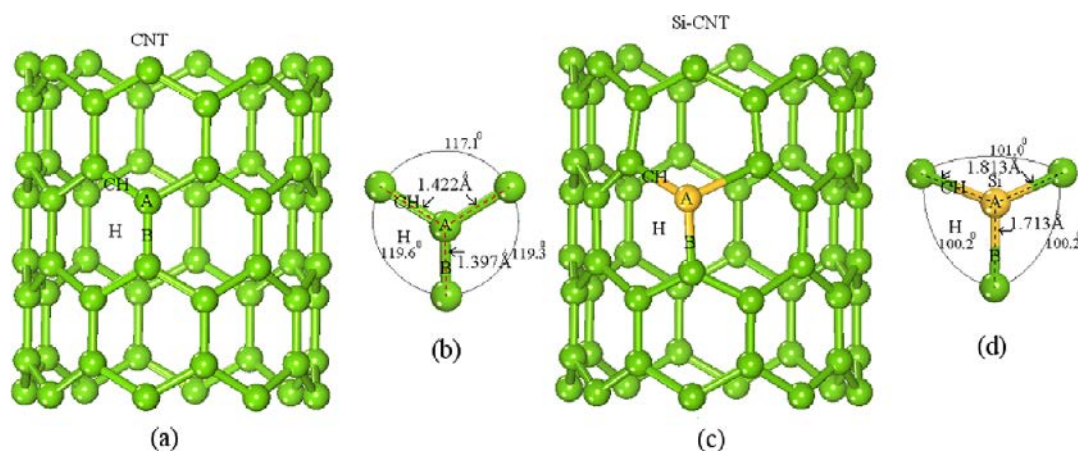


Fig. 1. (a) Ground state geometry of (8, 0) CNT. (b) Structural parameters at target atom. (c) Ground state geometry of (8, 0) Si-CNT. (d) Structural parameters at dopant. The green and yellow color represent carbon and silicon atom

3. Results and Discussion

Structural Properties of CNT and Si-CNT. The optimized ground state geometry of pure CNT is shown in Fig. 1 (a) along with geometrical parameters in Fig. 1 (b). The bond angles between C–C bonds are found to be less than 120° which indicates trigonal structure of bonding and prefers sp^2 hybridization. The stable structure of Si-CNT is shown in Fig. 1 (c) whereas change structural parameter due to doping of silicon atom is shown in Fig. 1 (d). The bond angles between (C-Si-C) bonds for all three combinations are less than 109° , which indicate tetrahedral structure of bonding and prefer sp^3 hybridization. All structural parameters of our result for CNT and Si-CNT are reported in our previous work found to be in good agreement with reported results [34,35]. The structural deformation produced by silicon doping results into a significant change in electronic properties like binding energy, band gap, density of states, charge density and charge transfer.

Electronic Properties of CNT and Si-CNT. The band structure of CNT and Si-CNT are shown in Fig. 2 (a). The doping of silicon atom creates an extra unoccupied energy state at 1.26 eV in the conduction band as observed in plot of band-structure. The additional state reduces the band gap of Si-CNT to 0.54 eV as compared to band gap of pure CNT. The DOS of CNT and Si-CNT are shown in Fig. 2 (b). The DOS analysis also shows same unoccupied state below the conduction band. Such an unoccupied state act as donor like impurity and which plays significant role of capturing center for atoms or molecules. Further, Mulliken Population analysis shows silicon atom acquires positive charge of magnitude 0.0815 e. This clears that the charge is transferred from the silicon to the vicinity carbon atoms. Such charge polarization at dopant site (silicon atom) acts as an affinity center for chemisorption of the molecules or atom. Thus, the doping of the silicon atom increases the p-type conductivity of the CNT and which improves the reactivity of CNT.

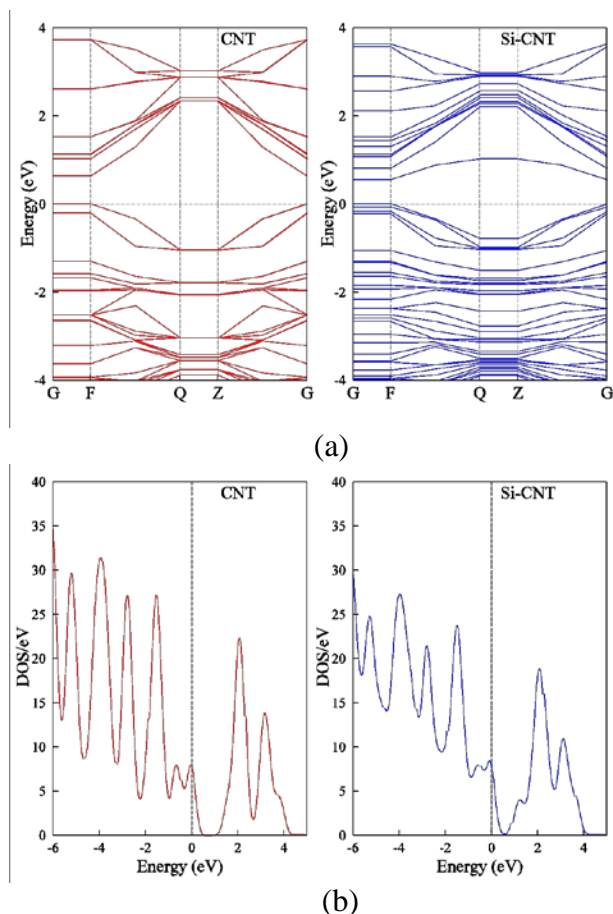


Fig. 2. (a) Band structure plot of CNT and Si-CNT. (b) Density of state of CNT and Si-CNT. The Fermi level is indicated by dotted black line

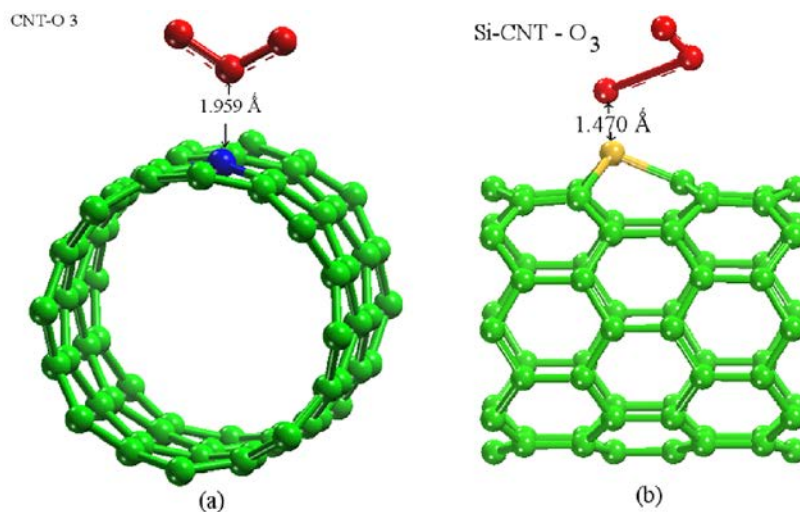


Fig. 3. Ground state geometries of O_3 molecule adsorbed on (a) CNT and (b) Si-CNT. The target carbon atom is shown by blue colour

Structural properties for adsorption of ozone molecule. To understand the mechanisms of ozone interaction with CNT and Si-CNT, we have calculated structural and electronic properties. Ozone molecule is directly located above the target carbon atom (site-A) of CNT as shown in Fig. 3 (a). The ozone molecule is found physisorbed at distance of 1.959 Å. The binding distance also indicates strong physisorption of ozone on CNT. The bond

angle between O-O-O oxygen atoms of ozone is decreased from 118° to 116° . The bond distances between O-O are also decreased from 1.279 \AA to 1.251 \AA . In Si-CNT, ozone molecule is chemisorbed on silicon atom (site A) (see Fig. 3 (b)). The ozone molecule binds to the silicon atom with formation of σ (Si-O) bond and its bond length found to be 1.470 \AA . In this case ozone molecule gets dissociated and single oxygen atom gets attached to silicon by σ bond whereas oxygen molecule is liberated from ozone. The bond lengths between oxygen atoms are 1.089 \AA and 2.871 \AA , whereas bond angle between O-O-O oxygen atoms of ozone is significantly decreased to 96.90° . As shown in Fig. 3 (b), the extended bond length between oxygen atoms of ozone confirms dissociation of ozone molecule.

Electronic properties for adsorption of ozone molecule. The band structure of CNT-O₃ molecule system is shown in Fig. 4 (a). The band structure of O₃ adsorption shows that the energy states in valence band near Fermi level are slightly separated as compared to band structure of CNT. Therefore, band gap of CNT-O₃ system is marginally more (0.63 eV) than the band gap (0.607 eV) of pure CNT. In DOS of CNT-O₃ system the occupancy of partially filled states is slightly increased at Fermi level as shown in Fig. 4 (b). Further, Mulliken Population analysis shows negligible charge 0.013 e transferred from CNT to O₃ molecule. The isosurface shown in Fig. 5 of CNT did not show overlapping of charge density between the O₃ molecule and CNT. Thus, ozone gas molecule is physisorbed with binding energy -0.43 eV and small quantity of charge transfer from carbon nanotube, consistent with the strong oxidizing nature of ozone.

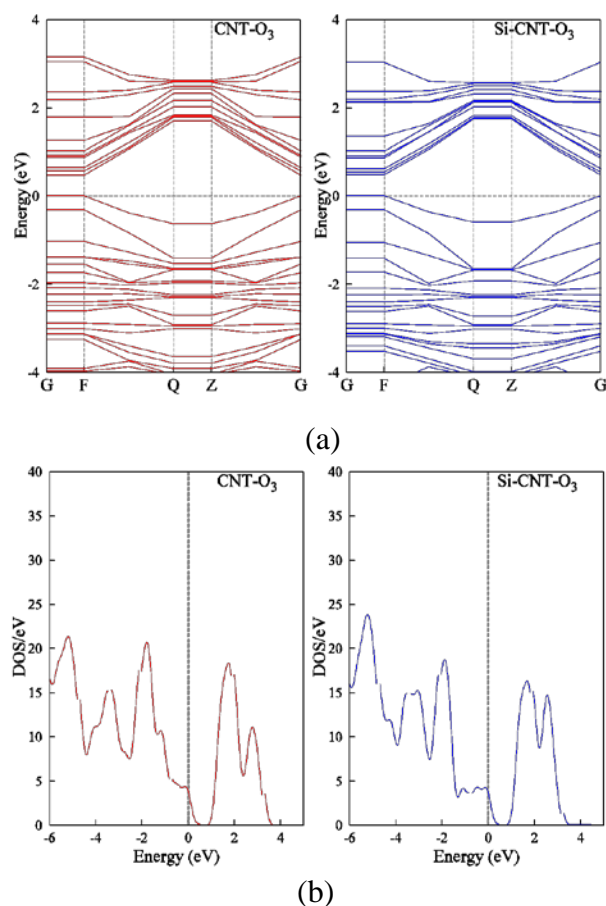


Fig. 4. (a) Band structure plot and (b) Density of state of O₃ molecule adsorbed on CNT and Si-CNT. The Fermi level is indicated by dotted black line

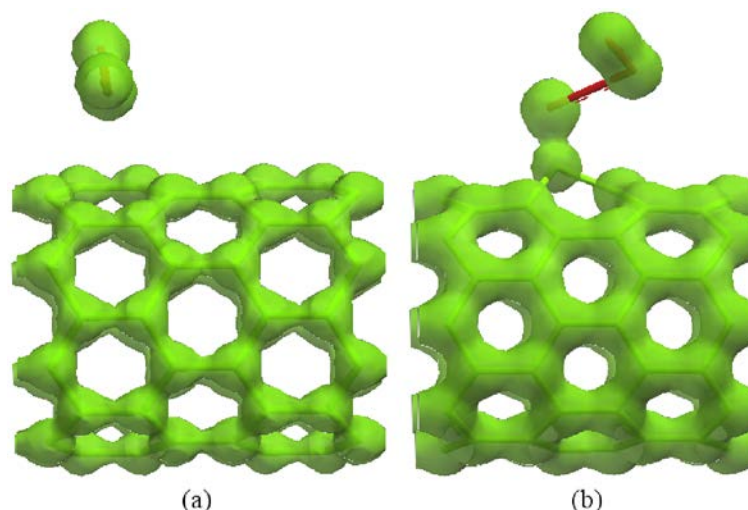


Fig. 5. Isosurface of the charge density of systems for O_3 molecule adsorption on (a) CNT and (b) Si-CNT

The binding energy, charge transfer and isosurface of ozone adsorption on CNT clearly show the character of the interaction can still be classified as physisorption. The adsorption of O_3 on Si-CNT is more pronounced as compared with CNT. However, when ozone adsorbs on Si-CNT, a strong chemisorption occurs, leading to relevant structural relaxations and to the formation of a Si-O σ bond with binding energy - 3.90 eV and charge transfer of 0.252 e. The band structure as shown in Fig. 7 is completely different than band structure of pure Si-CNT. The extra state observed in conduction band of Si-CNT is disappeared and some additional states are observed near Fermi level in valence band. These numbers of states are also clearly observed in DOS as shown in Fig. 8. These additional states reduce band gap of Si-CNT- O_3 system to 0.46 eV from 0.54 eV of Si-CNT. The occupancy of valence band at Fermi energy is completely altered due to ozone adsorption. The charge density analysis shows formation of sigma bond between oxygen and silicon atom. Contradictorily the isosurface of charge density shown in Fig. 5 visualize the dissociation of O_3 molecule and formation of silicon-oxide with Si-CNT, where oxygen molecule is liberated from ozone molecule. Thus, chemisorption of ozone molecule shows oxidization of silicon atom doped in CNT and releasing of oxygen molecule. This result is very important to construct sensors with silicon doped carbon nanotube to capture hazardous pollutant like ozone.

6. Conclusions

Density functional simulations study has been performed for adsorption of ozone gas molecule on pure carbon nanotube and silicon doped carbon nanotube. Our study has been focused on effect of silicon doping for adsorption of ozone molecule on carbon nanotube. Silicon doping creates extra unoccupied state in conduction band which plays important role in adsorption of ozone molecule silicon doped CNT. The ozone adsorption on pure CNTs shows a small binding energy (-0.43 eV) and charge transfer (0.0815 e) indicates the process is most likely of physisorption kind. The extra states in band structure and DOS of Si-CNT plays significant role in ozone adsorption. The large values of binding energy (- 3.90 eV) and charge transfer (0.252 e) shows ozone adsorbs on the Si-CNT is more pronounced as compared to CNT. The bond length between two oxygen atoms in ozone molecule has been increased due to adsorption on Si-CNT. It is observed that ozone molecule gets dissociated and one oxygen atom gets attached to silicon by forming σ bond whereas oxygen molecule is liberated from ozone. The isosurface of charge density visualize the clear dissociation of O_3 molecule and formation of silicon-oxide with Si-CNT and liberation of oxygen molecule

from ozone molecule. Thus Si-CNT captures ozone molecule forming silicon oxide and releasing oxygen molecule. The result gives grate potential to construct sensor which can capture hazardous ozone molecule. This can be an effective strategy to help in the reduction of the concentration of these harmful pollutants in the environment.

Acknowledgements. No external funding was received for this study.

References

- [1] Ijima S. Helical microtubules of graphitic carbon. *Nature*. 1991;354: 56-58.
- [2] Salvetat JP, Bonard JM, Thomson NH, Kulik AJ, Forró L, Benoit W, Zuppiroli L. Mechanical properties of carbon nanotubes. *Appl. Phys. A*. 1999;69(3): 255-260.
- [3] Kong J, Franklin NR, Zhou C, Chapline MG, Peng S, Cho K, Dai H. Nanotube Molecular Wires as Chemical Sensors. *Science*. 2000;287(5453): 622-625.
- [4] Colbert DT, Smalley RE. Fullerene nanobutes for molecular electronics. *Trends Biotechnol*. 1999;17(2):46-50.
- [5] Ajayan PM. Nanotubes from carbon. *Chemical Reviews*. 1999;99(7): 1787-1800.
- [6] Tasis DN, Tagmatarchis A, Bianco, Prato M. Chemistry of Carbon Nanotubes. *Chemical Reviews*. 2006;106(3): 1105-1136.
- [7] Karousis N, Tagmatarchis N, Tasis D. Current Progress on the Chemical Modification of Carbon Nanotubes. *Chemical Reviews*. 2010;110(9): 5366-5397.
- [8] Collins PG, Arnold MS, Avouris P. Engineering Carbon Nanotubes and Nanotube Circuits Using Electrical Breakdown. *Science*. 2001;292(5517): 706-709.
- [9] Groves MN, Chan ASW, Jugroot CM, Jugroot M. Improving platinum catalyst binding energy to graphene through nitrogen doping. *Chem. Phys. Lett*. 2009;481(4-6): 214-219.
- [10] Kong H, Zhou M, Lin GD, Zhang HB. Pt Catalyst Supported on Multi-Walled Carbon Nanotubes for Hydrogenation-De aromatization of Toluene and Tetralin. *Catal. Lett*. 2010;135(1-2): 83-90.
- [11] Ghosh S, Sood AK, Kumar N. Carbon Nanotube Flow Sensors. *Science*. 2003;299(5609): 1042-1044.
- [12] Peng S, Cho K. Ab Initio Study of Doped Carbon Nanotube Sensors. *Nano Lett*. 2003;3(4): 513-517.
- [13] Fruodakis GE. Why Alkali-Metal-Doped Carbon Nanotubes Possess High Hydrogen Uptake. *Nano Lett*. 2001;1(10): 531-533.
- [14] Harris PJF. *Carbon Nanotubes and Related Structures: New Materials for the Twenty-First Century*. Cambridge: University of Ontario Press; 1999.
- [15] Ciraci S, Dag S, Yildirim T, Gulseren O, Senger RT. Funcionalized carbon nanotubes and device applications. *J. Phys. Condens. Matter*. 2004;16(29): 901-960.
- [16] Zakharova GS, Volkov VL, Ivanovskaya VV, Ivanovskii AL. Nanotubes and related nanostructures of d-metal oxides: synthesis and computer design. *Russ. Chem. Rev*. 2005;74(7): 587-618.
- [17] Collins PG, Bradley K, Ishigami M, Zettl A. Extreme Oxygen Sensitivity of Electronic Properties of Carbon Nanotubes. *Science*. 2000;287(5459): 1801-1804.
- [18] Kong J, Franklin NR, Zhou C, Chapline MG, Peng S, Cho K, Dai H. Nanotube Molecular Wires as Chemical Sensors. *Science*. 2000;287(5453): 622-625.
- [19] Kong J. Functionalized Carbon Nanotubes for Molecular Hydrogen Sensors. *Adv. Mater*. 2001;13(18): 1384-1386.
- [20] Peng S, Cho K. Ab Initio Study of Doped Carbon Nanotube Sensors. *Nano. Lett*. 2003;3(4): 513-517.

- [21] Mawhinney DB, Naumenko V, Kuznetsova A, Yates JT, Liu Smalley J. Infrared Spectral Evidence for the Etching of Carbon Nanotubes: Ozone Oxidation at 298 K. *J. Am. Chem. Soc.* 2000;122(10): 2383-2384.
- [22] Picozzi S, Santucci S, Lozzi L, Cantalini C, Baratto C, Sberveglieri G, Armentano I, Kenny JM, Valentini L, Delley BJ. Ozone adsorption on carbon nanotubes: Ab initio calculations and experiments. *Vac. Sci. Technol. A.* 2004;22(4): 1466-1470.
- [23] Wongwiriyapan W, Honda S, Konishi H, Mizuta T, Ikuno T, Ohmori T, Ito T, Shimazaki R, Maekawa T, Suzuki K, Ishikawa H, Oura K, Katayama M. Itrasensitive Ozone Detection Using Single-Walled Carbon Nanotube Networks. *Jpn. J. Appl. Phys.* 2006;45(4B): 3669-3671.
- [24] Yim WL, Liu ZF. A reexamination of the chemisorption and desorption of ozone on the exterior of a (5,5) single-walled carbon nanotube. *Chem. Phys. Lett.* 2004;398(4-6): 297-303.
- [25] Akdim B, Kar T, Duan X, Pachter R. Density functional theory calculations of ozone adsorption on sidewall single-wall carbon nanotubes with Stone-Wales defects. *Chem. Phys. Lett.* 2007;445(4-6): 281-287.
- [26] Mawhinney DB, Naumenko V, Kuznetsova A, Yates Jr JT, Liu J, Smalley RE. Surface defect site density on single walled carbon nanotubes by titration. *Chem. Phys. Lett.* 2000;324(1-3): 213-316.
- [27] Kuznetsova A, Yates Jr JT, Simonyan VV, Johnson JK, Huffman CB, Smalley RE. Optimization of Xe adsorption kinetics in single walled carbon nanotubes. *J. Chem. Phys.* 2001;115(14): 6691-6698.
- [28] Charlier JC, Ebbesen TW, Lambin Ph. Structural and electronic properties of pentagon-heptagon pair defects in carbon nanotubes. *Phys. Rev. B.* 1996;53(16): 11108.
- [29] Abbasi A, Jaber Sardroodi J, Ebrahimzadeh AR, Yaghoobi M. Theoretical study of the structural and electronic properties of novel stanene-based buckled nanotubes and their adsorption behaviors. *Applied Surface Science.* 2018;435: 733-742.
- [30] Delley B. An all-electron numerical method for solving the local density functional for polyatomic molecules. *J. Chem. Phys.* 1990;92(1): 508-517.
- [31] Delley B. From molecules to solids with the DMol³ approach. *J. Chem. Phys.* 2000;113(18): 7756-7764.
- [32] Perdew JP, Burke K, Ernzerhof M. Generalized Gradient Approximation Made Simple. *Phys. Rev. Lett.* 1996;77(18): 3865-3868.
- [33] Monkhorst HJ, Pack JD. Special points for Brillouin-zone integrations. *Phys. Rev. B.* 1976;13(12): 5188-5192.
- [34] Guanlun G, Fang W. Reactivity of silicon doped carbon nanotubes toward small gaseous molecules in the atmosphere. *Int. J. Quantum Chemistry.* 2008;108(2): 203-212.
- [35] Haihui J, Dongju Z, Ruoxi W. Silicon-doped carbon nanotubes: a potential resource for the detection of chlorophenols/chlorophenoxy radicals. *Nanotechnology.* 2009;20(14): 145501-145507.

EFFECT OF WARM ROLLING ON MICROSTRUCTURE, POROSITY, AND HARDNESS OF A SPRAY-FORMED LM25 ALUMINUM ALLOY

Bandi Venkata Ramana Reddy*, S.R. Maity, K.M. Pandey

Department of Mechanical Engineering, National Institute of Technology, Silchar, Assam, 788010, India

*e-mail: reddymeta.iitr@gmail.com

Abstract. The LM25 aluminum alloy was obtained using the spray deposition method at an optimum pressure of approximately 10 bar, a deposition distance of approximately 41 cm. and an inclination angle of 0°. The central portion of the spray deposit was warm rolled to obtain various thickness reductions, i.e., 0%, 20%, 40%, 60%, and 80% at 100°C; it was found that the number of pores decreased as the thickness reduction increased. It was observed that the fine microstructure and secondary phase in the samples with a larger percentage of thickness reduction was due to the expediting cooling and freezing rate of the molten metal. The porosity and mechanical properties were better in the spray deposited and warmed rolled LM 25 substrate than the cast LM25 alloy.

Keywords: spray forming, warm rolling, microstructure, porosity, hardness

1. Introduction

LM25 alloys are widely used in the various applications, such as aviation [1], aerospace, bearing materials, electronic devices, shipping, and valve spring retainer industries, due to their high strength-to-low-weight ratio, their ease of casting, their high mechanical strength [2], and their high corrosion resistance. Adding 6% silicon (Si) to aluminum (Al) enhances the strength and the mechanical and metallurgical properties of the alloy. Various methods, such as the ingot method, powder metallurgy, spinning, stir casting [3], and the spray deposition technique [4], have been used to produce an LM25 deposit. While the LM25 alloy can be processed using conventional methods, the production costs are high, processing steps are required, and it is not possible to obtain the expected microstructure [5]. To overcome these issues, an LM25 alloy can be prepared using the spray forming technique [6]. In the spray forming technique, the major influencing parameters of the atomization processes [7] are pressure, the temperature during the warm rolling process to eliminate the porosity [8], and the gas-to-metal flow ratio. These must be minimized to obtain the desired microstructure and the respective material properties. The main problem with the spray deposition process is associated with the porosity due to the rapid pouring of the molten metal during the process. However, mechanical processes, such as rolling, extrusion, and forging, may be the solution to reduce the porosity and to improve the mechanical, metallurgical, and tribological properties of the LM25 alloy. Singer defined the basic principle of the spray deposition technique at the University College of Swansea, in the United Kingdom (UK) [9,10], in an attempt to establish the process for making the deposit strips based on the amalgamation of metal powder production vestige by inert gas atomization of liquid metals coupled with a consolidation step. Asish et al. [11] reported the processing of the Cu-Al-Ni alloy using the spray atomization and deposition process; they reported that the appropriate shape of the deposit was obtained at a pressure of 1 MPa, using argon gas and a rotor apex angle of 20°. That study also reported that there was no integration with the powder

http://dx.doi.org/10.18720/MPM.4232019_4

© 2019, Peter the Great St. Petersburg Polytechnic University

© 2019, Institute of Problems of Mechanical Engineering RAS

particles during the spray process. Ojha et al. [12] reported the shape and mechanical behavior of spray-deposited hypoeutectic Al-Si alloys; they found that the shape of the deposit was obtained by controlling the rotation and inclination of the substrate based on the spray axis. The uniformity of the deposit was achieved at a disposition of 30° inclination angle of the substrate around the spray axis. Rashmi Mittal et al. [13] reported on spray cast and cold rolled Al-Si alloys; they found that, as the rolling percentage increased, the porosity decreased, and hardness increased. However, no previous study has investigated the warm rolling effects on the microstructure and mechanical properties of alloys. The present study selected the warm rolled temperature from the phase diagram of the Al-Si alloy presented in [14]. In the present paper, the LM25 alloy was processed using the spray deposited technique, rolled at the warm rolling temperature, and the metallurgical and mechanical properties of the spray-deposited LM25 alloy were analyzed and compared with the properties of the cast LM25 alloy.

2. Experimental Procedure

To analyze the mechanical and metallurgical properties of the spray deposited and warm rolled samples in the central portion of the spray deposit, it is necessary to cast the 6% Al-Si substrate using emerging technology, i.e., the spray-forming technique. The schematic representation of the spray forming process is shown in Fig. 1. First, about 1 kg of 6% Al-Si alloy (Kovai Metal Mart, Coimbatore, Chennai, India) was placed in a crucible and heated to the super-heated temperature in a resistance heating furnace. The graphite crucible, compressor, induction furnace, atomizer, spray chamber ties with the delivery tube and the copper substrate are placed near the rotor, which is located 410 mm from the tip of the delivery tube. Then, the inert gas (nitrogen) is released through an atomizer, the pressure is adjusted to 10 bar, and the molten metal is instantly poured. This enables semi-solid droplets to rapidly form over the copper substrate after the preformed deposition is removed from the substrate. Then, the dimensions, such as thickness and diameter, are measured. The processing parameters used during the experiment are presented in Table 1.

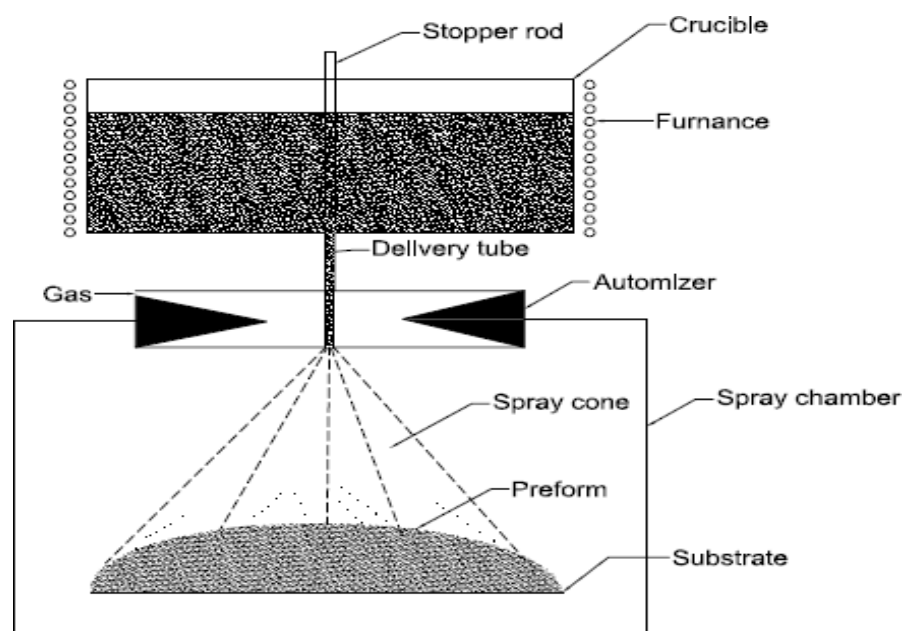


Fig. 1. Spray deposition process

Table 1. Processing Parameters

Pressure (bar)	Type of inert gas	Spray deposition distance (cm)	Inclination (Theta)	Melting point (Degrees)
10	Nitrogen	41	0	1450

The sample of size (20 mm×20 mm) is cut from the center of the spray deposit, heated at 100°C in the resistance heating furnace, and rolled with the help of a warm rolling machine to obtain different thickness reductions, such as: 0%, 20%, 40%, 60%, and 80% represented in Table 2.

Table 2. Warm Rolling Conditions

Iteration No.	Initial thickness of the sample (mm)	Final thickness of the sample (mm)	% of thickness reduction	Warm rolling temperature (°C)
1	20	20	0	100
2	20	16	20	100
3	16	10.50	40	100
4	10	4.2	60	100
5	4.2	0.84	80	100

Samples measuring 10 mm × 10 mm were cut down from rolled samples and prepared as per the metallographic ASTM E3-95 standards to analyze the rolling direction and microstructural behavior. The warm rolled samples initially underwent abrasive grinding (to remove unnecessary particles over the surface and edges) and were then mounted by using Bakelite as the adhesive agent. The mounted samples underwent paper polishing with an emery paper of 1/0, 2/0, 3/0 and 4/0 specifications and were then cleaned with kerosene. An emulsion powder of alumina suspended in H₂O was used to perform wheel cloth polishing (rotational speed of the wheel less than 250 rpm) of the samples. Then, the samples were dried using a drier and etched with Keller's reagent (190 ml of distilled water, 5 ml of nitric acid, 3 ml of HCl and 2 ml of HF). After the completion of the above steps, the samples were systematically examined with Leitz optical microscope. Image analyses were performed to determine the percentage of surface porosity present in the warm rolled samples for various percentage reductions in thickness, i.e., 0%, 20%, 40%, 60% and 80% from the center of the deposit. For this, an optical microscope "Olympus model PM-3-311U" and a computer having an image analysis software from "De-Winter materials plus" were used. To determine total porosity, the densities of the samples prepared as per the ASTM B328-96 standards were measured by using Archimedes' principle. The samples are developed as per the ASTM E92 standard to determine the degree of hardness. The hardness value for all samples is calculated via Vickers test mode HPO 250 at 16 kg load by moving the indenter to various locations of the specimen and then estimating the average hardness value.

3. Results and discussion

Shape. It was observed that the obtained shape of the spray deposit (Al-6%Si) is in the form of a Gaussian curve having a thickness of 20 mm and a diameter of 200 mm (Fig. 2). It was obtained at an angle of inclination of 0°, distance of 410 mm and pressure of 10 bar.

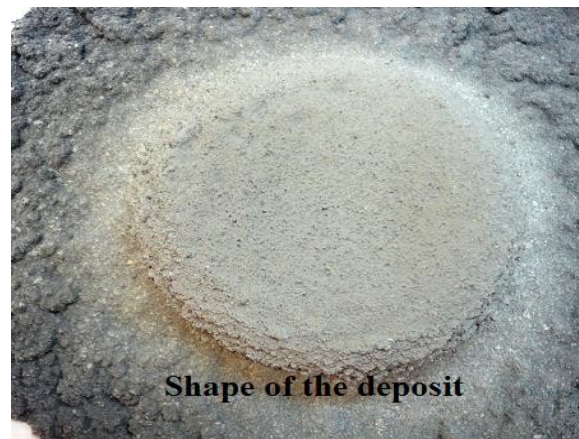


Fig. 2. Shape of the deposit

The deposit shape depended on factors like pouring time, deposition distance, diameter of the delivery tube and inclination angle of the rotor. It is essential that the molten metal must be poured within 20 s to 50 s to prevent its solidification in the delivery tube that can lead to irregular shape of the deposit. It was observed that the shape also depends on the distance (deposition distance between the tip of the delivery tube and rotor). In the initial trial, when the distance was maintained at less than 400 mm, the shape was flat and uniform. In the second trial, when the distance was more than the 420 mm, the shape obtained was similar to that of a spray cone. In the third trial, when the distance was maintained at 410 mm, the desired shape was obtained. The diameter of the delivery tube also affects the shape obtained. It was observed that the desired shape was obtained at the optimum diameter of tube, i.e., 3 to 4 mm. If the diameter is more than 4 mm, the molten metal passage is very high and fallen down maximum at the center portion of the substrate, which is lying over the rotor. The maximum inclination of the rotor is 0° for obtaining the Gaussian shape of the deposit. It was observed that for other inclinations like 30° , 45° and 60° , the proper spray cone was not obtained. Therefore, it was concluded that the shape of the deposit is obtained at pouring time of 30 s, distance of 410 mm, delivery tube diameter of 4 mm, rotor inclination angle of 0° and pressure of about 10 bar.

Microstructural Analysis. Microstructural pictographs of LM25 alloy before and after warm rolling were observed for comparing the microstructural features as shown in Fig. 3. From Fig. 3a. it has found that after spray forming and before warm rolling, the Si phase is distributed along the grain boundaries of the Al matrix. The EDS analysis confirmed that the grey region belongs to the Si region and the white region belongs to Aluminum. Grain size was calculated for each rolled and unrolled specimen as per ASTM E-112 (intercept method) specifications. Fig. 3a shows that the average grain size of Al before warm rolling is different at 20-23 μm and Si is about 7-6 μm . The pores of 15-20 μm are obtained during the pouring of the molten metal, which is called casting porosity. From Fig. 3b-e, it can be observed that the grains elongated along the rolling direction and length of the grain is increased with the reduction in thickness. This is due to dynamic recrystallization temperature of the material that leads to rapid movement of the molecules. In comparison with cold rolled specimens, the warm rolled specimens showed elongation in width direction as represented in Table 3.

Table 3. Average length of the grains

Grain size (μm)	Cold rolled Al-6Si	Warm rolled Al-6Si alloy
% of rolling		
0	20	24
20	22.5	28
40	30	33.5
60	38	41
80	42	48

Therefore, there are two types of porosity in the samples: crack porosity due to rolling and casting porosity due to pouring. Decreased casting porosity accounted for up to 60% thickness reduction in Fig. 3b-d, casting porosity almost eliminated for 80% thickness reduction. It was also observed that the porosity was lower in warm rolled samples than the cold rolled and unrolled samples because the grains elongated rapidly with increasing temperature.

Porosity. As mentioned in the previous sections, two types of porosity were found: 1. casting porosity; 2. cracking porosity. The casting porosity mainly presented inside the rolled samples; the reduction in thickness occurred along the rolling direction of the samples (Fig. 3b-e). The graph drawn between thickness vs. porosity in the sample is depicted in Fig. 4. In the initial stage of warm rolling, i.e., from 0 to 40% reduction, the passage of the molten metal into LM 25 alloy is in the rolling direction. Rearrangement and restocking of the sprayed particles resulted in the removal of porosity. As the rolling percentage increased from 40% to 80%, plastic deformation is the dominant mechanism during warm rolling. As a result, pores elongated rapidly due to the movement of molecules in the rolling direction. This led to their fragmentation into several tiny pores. This process of fragmentation and elongation continued during the warm rolling process. In this process, the width of the elongated grains is very less, and the opposite faces of the pores are almost eliminated, and the casting porosity is removed. If the oxide layer is formed inside the pores, it can be ruptured by the deviatoric stress. The crack porosity is due to the rolling process. The initial globular shape of sprayed particles was transformed into plastically deformed grains. This results in cracks due to the presence of porosity and internal cavities existing in the sprayed structure. These pores and cavities are covered with the oxide layer, disallowing the closure of those upon application of compressive pressure.

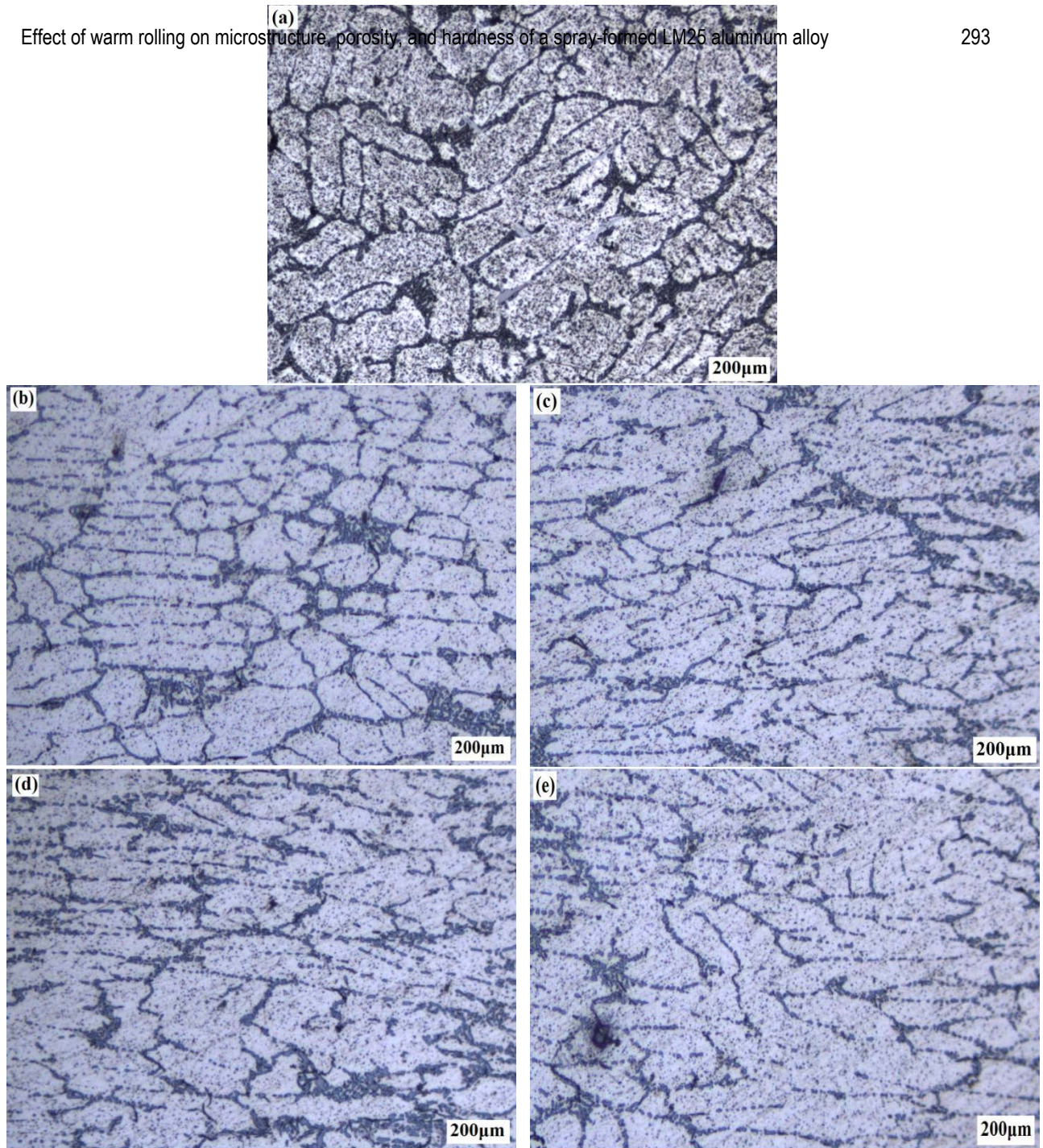


Fig. 3. Optical micrographs of spray deposited and warm rolled LM25 alloy at a thickness reduction of (a) 0%, (b) 20%, (c) 40%, (d) 60% and (e) 80%

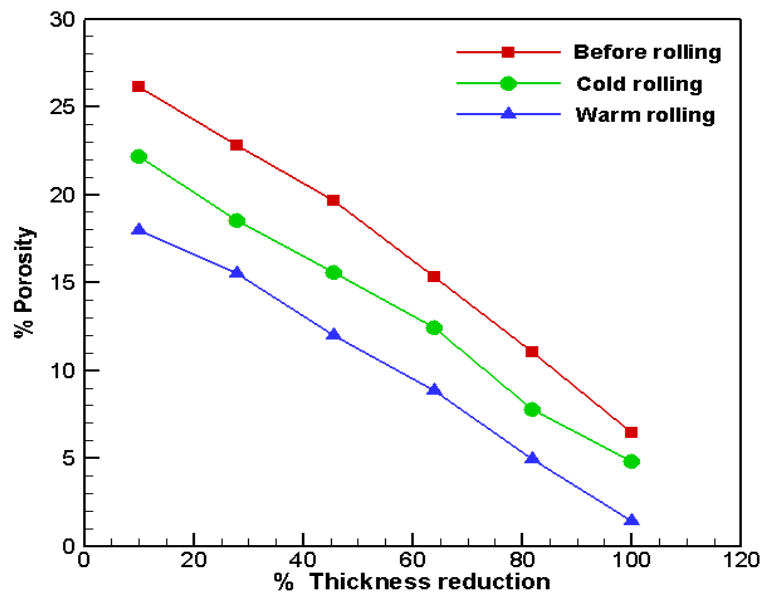


Fig. 4. Variation in porosity with reduced thickness in samples of LM25 alloy

Hardness. The Vickers hardness value of LM25 alloy was calculated before and after warm rolling. Before rolling, i.e., 0% thickness reduction, the samples had hardness values in the range of 50-90 VHN as represented in Fig. 5. After warm rolling, the Vickers hardness value increased to 60-140 VHN. As the thickness reduction increased in the samples, the hardness value also increased, as represented in Fig. 5. The hardness values of warm rolled samples were observed to be better than the cold rolled and spray deposited samples because of sudden expansion and compaction in the samples.

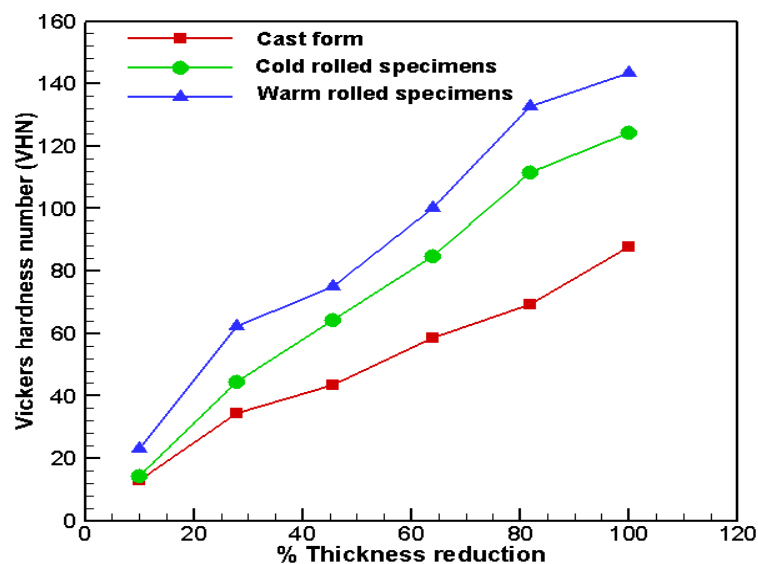


Fig. 5. Variation in VHN number with thickness reduction samples of LM25 alloy

4. Conclusions

Following conclusions were drawn on the basis of experimentation:

1. In trial 1 and trail 2 with deposition distances of 400 mm and 410 mm, respectively, the obtained shape of the deposits were non-uniform. As the deposition distance increased to 420 mm in trail 3, the thickness of the deposits became uniform.
2. The average grain size of spray deposited alloy without rolling was 20-24 μm , cold rolled samples was 20-42 μm and warm rolled samples was 24-48 μm . Warm rolled

samples possessed fine microstructure than other rolled samples due to higher elongation length and lower width of the grains.

3. Two porosities were present in the samples, i.e., casting and crack porosities. Casting porosity was removed by rearrangement and restocking of the spray deposited LM alloy. Crack porosity was reduced by the warm rolling process. 80% thickness was reduced for samples possessing almost negligible porosity. Hardness values of warm rolled samples (60-140 VHN) are more than that of casted (50-90 VHN) and cold rolled (50-120 VHN) samples because of lower porosity and rapid movement of molecules in warm rolled samples.

Acknowledgements. No external funding was received for this study.

References

- [1] Zhang Q, Zhang C, Lin J, Zhao G, Chen L, Zhang H. Microstructure analysis and low-cycle fatigue behavior of spray-formed Al–Li alloy 2195 extruded plate. *Materials Science and Engineering: A*. 2019;742: 773-787.
- [2] Zhang X, Chen Y, Hu J. Recent advances in the development of aerospace materials. *Progress in Aerospace Sciences*. 2018;97: 22-34.
- [3] Ran G, Zhou JE, Xi S, Li P. Microstructure and morphology of Al–Pb bearing alloy synthesized by mechanical alloying and hot extrusion. *Journal of alloys and compounds*. 2006;419(1-2): 66-70.
- [4] Li L, Wei L, Xu Y, Mao L, Wu S. Study on the optimizing mechanisms of superior comprehensive properties of a hot spray formed Al-Zn-Mg-Cu alloy. *Materials Science and Engineering: A*. 2019;742: 102-108.
- [5] Raju K, Harsha AP, Ojha SN. Effect of processing techniques on the mechanical and wear properties of Al-20Si alloy. *Transactions of the Indian Institute of Metals*. 2011;64(1-2): 1-5.
- [6] Mauduit D, Dusserre G, Cutard T. Influence of temperature cycles on strength and microstructure of spray-deposited Si-Al CE9F alloy. *Mechanics of Materials*. 2019;131: 91-101.
- [7] Cui C, Schulz A, Schimanski K, Zoch HW. Spray forming of hypereutectic Al–Si alloys. *Journal of Materials Processing Technology*. 2009;209(11): 5220-5228.
- [8] Jia Y, Cao F, Scudino S, Ma P, Li H, Yu L, Eckert J, Sun J. Microstructure and thermal expansion behavior of spray-deposited Al–50Si. *Materials & Design*. 2014;57: 585-591.
- [9] Singer AR. Principles of spray rolling of metals. *Metals Materials*. 1970;4(6): 246-250.
- [10] Singer AR. Aluminum and aluminum alloy strip produced by spray deposition and rolling. *J. Inst. Met*. 1972;100: 185-190.
- [11] Agrawal A, Dube RK. Processing of Cu–Al–Ni Alloy by Spray Atomization and Deposition Process. *Transactions of the Indian Institute of Metals*. 2018;71(10): 2541-2552.
- [12] Ojha KV, Tomar A, Singh D, Kaushal GC. Shape, wear & mechanical properties of spray formed hypoeutectic Al-Si alloys. *Transactions of the Indian Institute of Metals*. 2008;61(2-3): 139-143.
- [13] Mittal R, Singh D. Dry Sliding Wear Behavior of Cold Rolled Spray Cast Al–6Si Alloy. *Transactions of the Indian Institute of Metals*. 2014;67(4): 551-557.
- [14] Vander Voort GF, Asensio-Lozano J. The Al-Si phase diagram. *Microscopy and Microanalysis*. 2009;15(S2): 60-61.

COUPLED THERMO-ELECTRO-MECHANICAL MODELING OF THERMAL FATIGUE OF SINGLE-CRYSTAL CORSET SAMPLES

A.V. Savikovskii^{1*}, A.S. Semenov¹, L.B. Getsov²

¹SPBPU, Polytechnicheskaya 29, Russia

²NPO CKTI, Polytechnicheskaya 24, Russia

*e-mail: temachess@yandex.ru

Abstract. The possibilities of predicting thermal fatigue durability for single crystal on the base of coupled thermo-electro-mechanical finite-element modeling with using of deformational criterion and microstructural models of inelastic deformation are investigated. Results of thermal and stress-strain state simulations of single-crystal corset specimens under cyclic electric heating and cooling are presented and discussed. Comparison of computational results with experimental data for various single-crystal nickel-based superalloys demonstrates a good accuracy in the prediction of the number of cycles for the macrocrack initiation. The influence of maximum / minimum values of temperature in cycle and delay duration on the number of cycles for the macrocrack initiation are analyzed. The simplified analytic approximation for thermal fatigue durability curves is proposed.

Keywords: thermal fatigue, single-crystal nickel based superalloy, deformation criterion, corset sample, thermo-electric problem, finite element modeling

1. Introduction

Single-crystal nickel based superalloys [1] are used for manufacturing of blades of gas turbine engines (GTE). These materials have a pronounced anisotropy of properties and sensitivity to crystallographic orientation. The thermal fatigue strength of single crystal superalloys for various crystallographic orientations is not studied very well. For investigation of thermal fatigue durability under a wide range of temperatures with and without intermediate delays the experiments are carried out on corset (plane) specimen on the installation developed in NPO CKTI [2] (see Fig. 1). Fixed in axial direction by means of two bolts with a massive foundation a corset sample (see Fig. 2) is heated cyclic by passing electric current through it. During cycling the maximum and minimum temperatures are automatically maintained constant.

The aims of the study are: (I) to investigate numerically a process of heating and cooling of the corset sample and to obtain analytical approximation of this process, (II) to study numerically a stress-strain state of the sample during cyclic heating and cooling due to its clamping and (III) to study systematically the effect of delay at maximum temperature on the thermal fatigue durability on the base of the deformation criterion [3-5] of thermal-fatigue failure for single crystal superalloys using the results of finite element (FE) simulation of full-scale experiments. The results of simulation and their verification are obtained for the different single-crystal nickel-based superalloys: VZhM4, VIN3 and ZhS32.

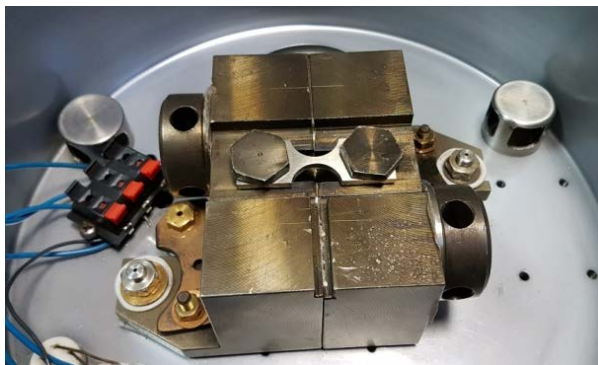


Fig. 1. Testing setup for thermal fatigue experiments

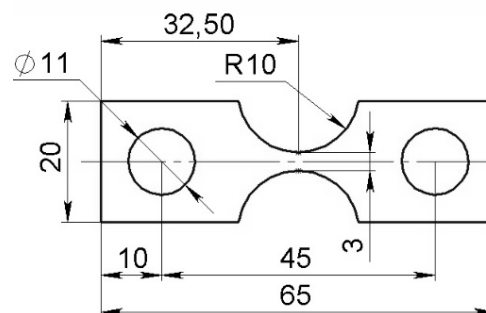


Fig. 2. Geometrical parameters of the corset sample

2. Results of numerical thermo-electric nonstationary analysis and analytical approximation for temperature changing during time

Modeling of a heating process by an electric current and a cooling process without an electric current of the corset sample has been performed with help of the FE program ANSYS with taking into account a temperature dependence of all material properties, thermos-electric contacts between the sample and an equipment, nonstationary Joule heating, convective heat exchange and radiative heat transfer between the sample and the environment. The full-scale FE model ($\frac{1}{4}$ due to symmetry) of experimental object including discrete models of the specimen and equipment is presented in Fig. 3.

The simulations have been performed for single-crystal superalloys VZhM4, VIN3 and ZhS32. The properties of three alloys were accepted the same because of lack of information about nickel alloys properties dependence on temperature.

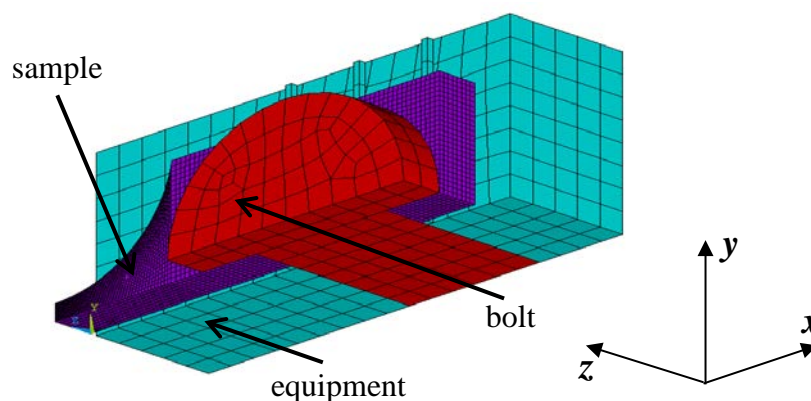


Fig. 3. Finite-element model of the corset sample with taking into account of equipment for the solution of thermo-electric problem

Modeling of heating and cooling processes of sample is carried out for five loading regimes (modes), which will be denoted further by indicating the minimum and maximum temperature of the cycle:

- 100÷800°C, a heating time is 19 s, a cooling time is 46 s;
- 150÷900°C, a heating time is 42 s, a cooling time is 59,5 s;
- 250÷1000°C, a heating time is 80 s, a cooling time is 10 s;
- 500÷1050°C, a heating time is 14 s, a cooling time is 10 s;
- 700÷1050°C, a heating time is 8 s, a cooling time is 7 s.

The material properties used in FE simulations for the single crystal nickel superalloy sample and for the steel equipment were taken from literature [6-9] (see also Tables 1-2). While specifying the properties of nickel alloy and steel the implementation of the Wiedemann-Franz's law was controlled: $\lambda \cdot \rho_e = LT$, where λ is the thermal conductivity, ρ_e is the specific electrical resistance, T is the temperature in K, $L = 2.22 \cdot 10^{-8} \text{ W} \cdot \Omega \cdot \text{K}^{-2}$ is the Lorentz's constant.

Table 1. Thermo-electric properties of nickel superalloy used in simulations

T	$^{\circ}\text{C}$	20	200	400	800	1000	1150	Ref.
ρ	Kg/m^3	8550	8500	8450	8350	8330	8310	[7]
C_p	$\text{J}/(\text{kg} \cdot \text{K})$	440	520	520	570	590	600	[7]
λ	$\text{W}/(\text{m} \cdot \text{K})$	7.4	11.2	14.1	19.8	26.7	36.7	[6]
ρ_e	$\Omega \cdot \text{m}$	$8.7 \cdot 10^{-7}$	$9.3 \cdot 10^{-7}$	$1 \cdot 10^{-6}$	$1.2 \cdot 10^{-6}$	$1 \cdot 10^{-6}$	$8.9 \cdot 10^{-7}$	[6]

Table 2. Thermo-electric properties of pearlitic steel used in simulations

T	$^{\circ}\text{C}$	27	127	327	527	927	1127	Ref.
ρ	Kg/m^3	7778	7772	7767	7762	7754	7751	[8]
C_p	$\text{J}/(\text{kg} \cdot \text{K})$	469	506	521	660	577	530	[8]
λ	$\text{W}/(\text{m} \cdot \text{K})$	48	47	41	37	23	12	[8]
ρ_e	$\Omega \cdot \text{m}$	$2 \cdot 10^{-7}$	$2.6 \cdot 10^{-7}$	$4.2 \cdot 10^{-7}$	$6.4 \cdot 10^{-7}$	$1.16 \cdot 10^{-6}$	$1.4 \cdot 10^{-6}$	[9]

The coupled three-dimensional transient thermo-electrical analysis has been performed. Due to the symmetry in respect to the xz and yz planes, a quarter of the structure is considered in simulations. Thermal and electric contacts between the sample and bolts, between the sample and the foundation are taken into account. The initial temperature for the sample and the equipment is set to 30°C . For the free surface of sample the boundary condition of convective heat transfer is used:

$$q_n = h(T - T_0), \quad (1)$$

where q_n is the heat flux density, $h = 20 \frac{\text{W}}{\text{m}^2\text{K}}$ is the coefficient of convective heat transfer, T_0 is the ambient temperature.

The condition of radiative heat transfer is also set on the surfaces of central (high temperature) part of the sample (10 mm length):

$$q_n = \varepsilon \sigma_{SB}(T^4 - T_0^4), \quad (2)$$

where $\varepsilon = 0.8$ is the black factor of the body, $\sigma_{SB} = 5.67 \cdot 10^{-8} \text{ Wm}^{-2}\text{K}^{-4}$ is the coefficient of Stefan-Boltzmann.

In order to realize an analytical approximation for the curve of temperature change in time, we consider the problem of mathematical physics of heating the sample with a constant cross-section. For example, the sample has a length and a depth the same with the corset sample 32.5 mm and 3 mm respectively, but the sample with a constant cross section has width is equal to 10 mm (Fig. 4).

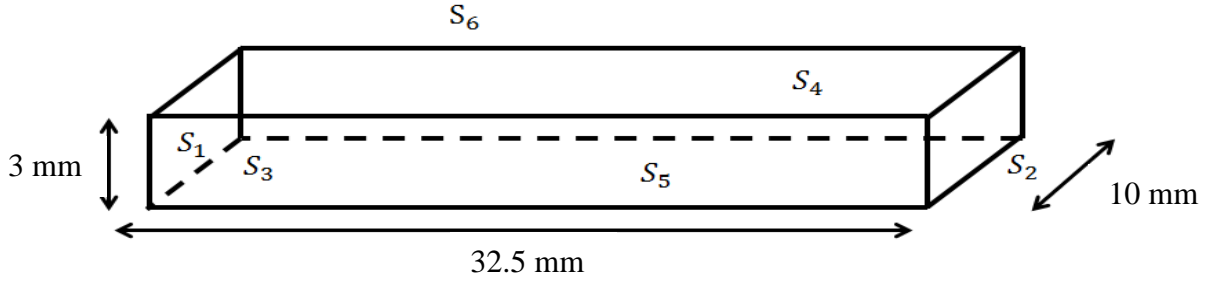


Fig. 4. The statement of simplified thermal problem

The aim of our analogy is to simplify a task of heating the corset sample to one-dimensional problem with equivalent boundary conditions. The isolation boundary conditions are set on surfaces S_3, S_4, S_5, S_6 . On the surface S_2 is fixed the temperature, on the surface S_1 boundary condition of convection with a convective heat transfer coefficient h is equal to $20 \frac{W}{m^2K}$. The sample in the thermal problem is heating by electric current that's why boundary condition of heat generation is set on the sample is equal to some constant Q , which does not depend on time. The equation of unsteady thermal conductivity can be represented as [10]:

$$\Delta T - \frac{\partial T}{\partial \tau} = -\frac{Q}{\lambda}, \quad (3)$$

where T is the temperature, Δ is the Laplace operator, $\tau = \frac{\lambda t}{C\rho\rho}$ is the slow time, Q is the heat generation, $\lambda, C\rho, \rho$ are the conductive coefficient, the specific heat and the density respectively. Considering that boundary conditions in the axis y and z are a lack of heat flux and overwriting the Laplacian in Cartesian coordinates, we come to the equation:

$$\frac{d^2 T}{dx^2} - \frac{\partial T}{\partial \tau} = -\frac{Q}{\lambda}, \quad (4)$$

where x is the axial coordinate along the sample. Representing T as a sum of two functions $T_1(x)$ and $T_2(x, \tau)$, we come to two equations. One of these equations has two variable, coordinate x and time τ :

$$\frac{\partial^2 T_2}{\partial x^2} - \frac{\partial T_2}{\partial \tau} = 0. \quad (5)$$

Using Fourier method [10], we put two equations with variables $X(x)$ and $\Omega(\tau)$ respectively. The equation for the variable X is:

$$X'' + \beta X = 0, \quad (6)$$

where β is the arbitrary constant. Boundary conditions for the equation (6) are a convective boundary condition in the middle of the sample and temperature is equal to zero on the edges. Also the equation with a variable Ω is:

$$\Omega' + \beta\Omega = 0. \quad (7)$$

Finding a solution of equation (6) as a sum of sinus and cosine with constants and substituting boundary conditions we put a transcendental equation:

$$\text{tg } \gamma_n = -\frac{\lambda \gamma_n}{hl}, \quad (8)$$

where $\gamma_n = \sqrt{\beta_n}l, h = 20 \frac{W}{m^2K}, l = 32.5 \text{ mm}$. General solution of equation (7) is $\Omega = Ce^{-\beta_n \tau}$,

where β_n is the eigenvalue and $\beta_n = \frac{\gamma_n^2}{l^2}$. As a result, we get $T_2(x, \tau) = C \cdot X(x) \cdot e^{-\frac{\gamma_n^2}{l^2} \tau}$, where γ_n can be found from an equation (8). We use simple approximation for temperature changing in time for a heating and cooling as one exponential with exponent $-\frac{\gamma_n^2}{l^2}$ with constants. Returning to usual time t , we can rewrite an analytical approximation for heating as:

$$T = A - B \cdot e^{-\frac{\gamma_n^2}{l^2} \frac{\lambda}{C\rho\rho} t}, \quad (9)$$

where A and B are constants, which are selected from conditions of equality in the beginning of the heating to minimum temperature in the cycle and in the end of the heating to maximum temperature in the cycle, γ_n can be found from a transcendental equation (8), l is the length of the sample. For a process of the cooling of the sample the similar analytical approximation is introduced:

$$T = C + D \cdot e^{-\frac{\gamma_n^2 \lambda}{l^2 c \rho} t}. \quad (10)$$

Signs before constants B and D in (9) and (10) provide positive values of B and D .

Material constants λ , c , ρ are set to $20 \frac{W}{mK}$, $550 \frac{J}{kg \cdot K}$ and $8400 \frac{Kg}{m^3}$ respectively. Comparison of experimental data, computational results and analytical approximation for temperature changing in time are presented in Fig. 5 for loading regimes $100 \div 800$, $150 \div 900$, $500 \div 1050$ and $700 \div 1050$ °C.

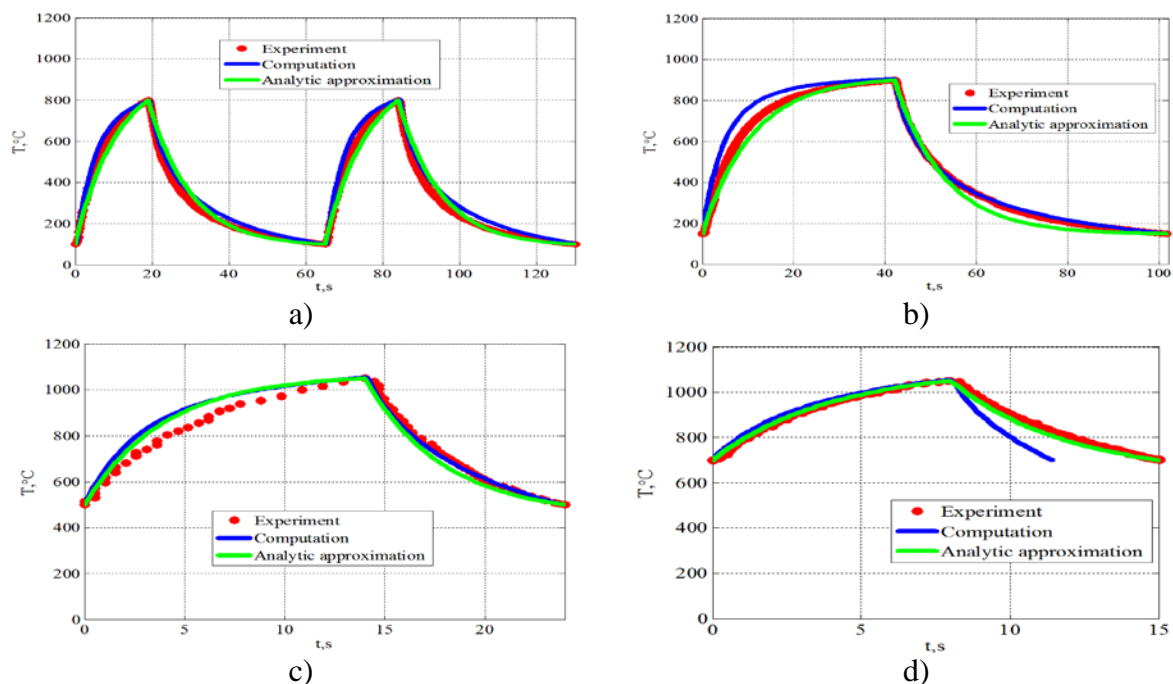


Fig. 5. Comparison of experimental data, simulation results and analytical approximation for temperature modes:

- a) $100 \div 800$ °C, a heating time is 19 s, a cooling time is 46 s;
- b) $150 \div 900$ °C, a heating time is 42 s, a cooling time is 60 s;
- c) $500 \div 1050$ °C, a heating time is 14 s, a cooling time is 10 s;
- d) $700 \div 1050$ °C, a heating time is 8 s, a cooling time is 7 s

Comparison of experimental data and computational results for temperature distribution along the corset sample at cycle phase with maximum temperature and also for the different times for loading regimes $150 \div 900$, $250 \div 1000$, $500 \div 1050$ and $700 \div 1050$ °C are shown in Fig. 6.

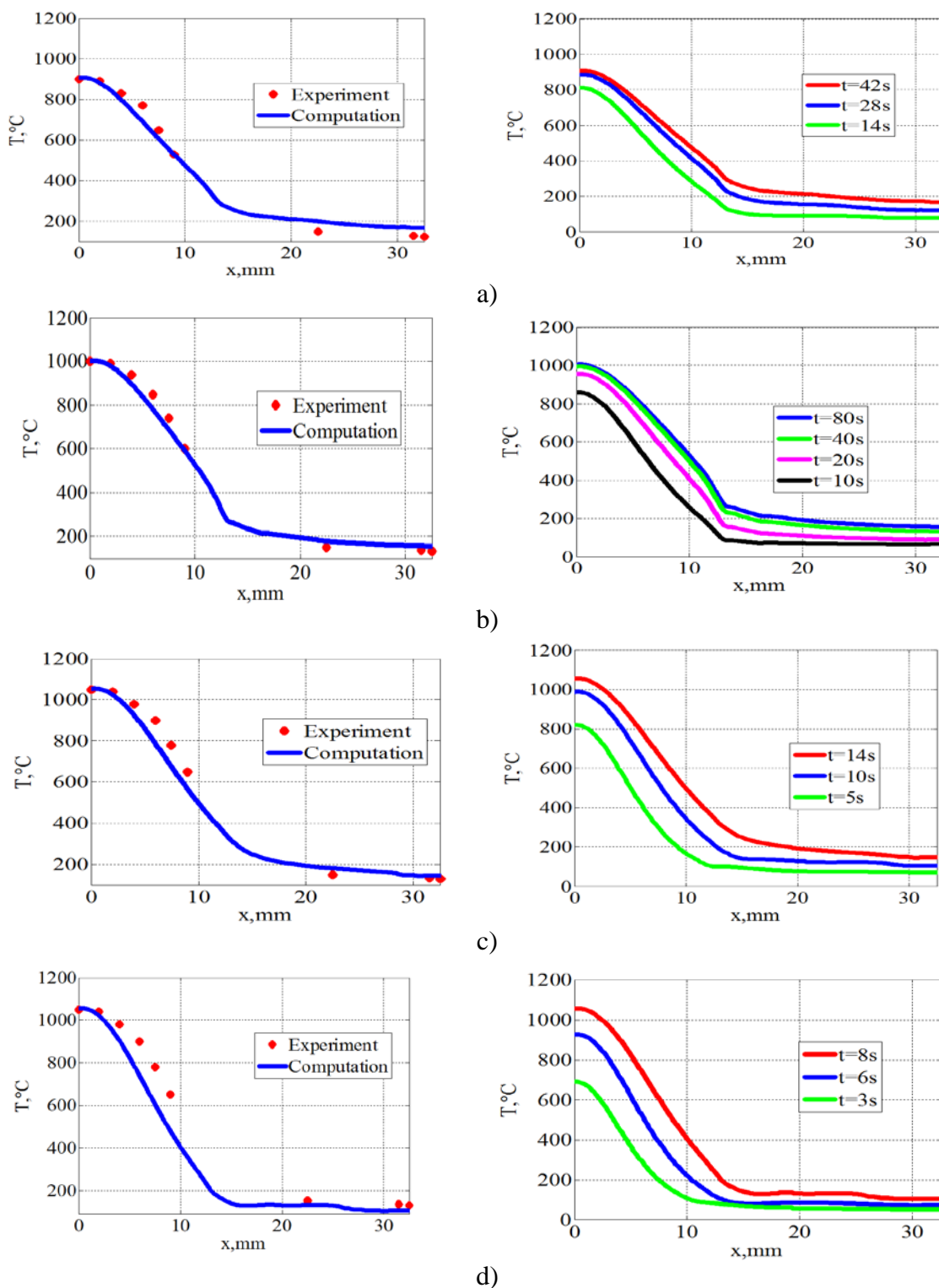


Fig. 6. Temperature distribution along the corset sample at cycle phase with maximum temperature (left) and also for the different times (right) for loading regimes: a) 150÷900°C, a heating time is 42 s, b) 250÷1000°C, a heating time is 80 s; c) 500÷1050°C, a heating time is 14 s, d) 700÷1050°C a heating time is 8 s

Temperature field distributions for cycle phase with maximum temperature for loading modes 100÷800, 150÷900, 250÷1000 and 700÷1050°C are presented in Fig. 7.

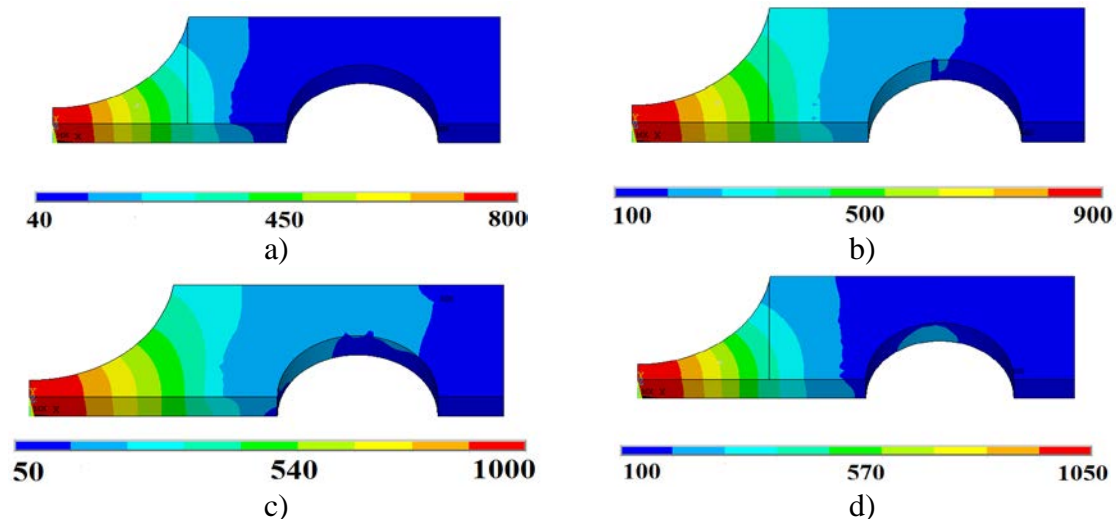


Fig. 7. Temperature field distributions for maximum temperature for loading regimes:
 a) 100÷800°C; b) 150÷900°C; c) 250÷1000°C; d) 500÷1050°C

The results of thermo-electric problem simulations in form spatial and temporal distribution of the temperature field are the base for the strain and stress field computation within the framework of thermo-elasto-visco-plastic problem.

3. Results of thermo-elasto-visco-plastic analysis

The axial fixing of the corset specimen under heating leads to the high axial stress and inelastic strain appearance. The local strain and stress concentration is observed in the central part of the corset sample. The numerical simulation is required for the computation of inhomogeneous stress and inelastic strain fields in sample. Modeling and simulation of inelastic cyclic deformation of corset samples has been performed by means of the FE programs ANSYS and PANTOCRATOR [11], which allows to apply the micromechanical (microstructural, crystallographic, physical) models of plasticity and creep for single crystals [12,13]. The micromechanical plasticity model accounting 12 octahedral slip systems with lateral and nonlinear kinematic hardening [12] is used in the FE computation for the simulation single crystal superalloy behavior under cyclic loading. The Norton power-type law is used to describe creep properties.

Modeling of inelastic deformation in the corset samples has been performed with taking into account of the temperature dependence of all material properties, anisotropy of mechanical properties of single crystal sample, inhomogeneous nonstationary temperature field, mechanical contacts between bolt and the specimen, between specimen and foundation, friction between the contact surfaces, temperature expansion in the specimen and foundation. The viscous properties are taken into account because of high temperature despite a quick time of heating and cooling of the corset samples.

The two FE formulations for the thermo-mechanical problem have been considered:

- FE model with taking into account equipment;
- FE model without taking into account equipment (simplified formulation [14] for the sample only).

Using of the second formulation provides significant saving computational time due to reduction in the number of degrees of freedom and refusal to solve a contact problem. It is very actual for the numerous multivariant computations for different regimes of loading and the crystallographic orientations. One of the aims of the investigations is the selection of the equivalent (effective) length of the sample for the simplified formulation. The validity of the

simplified formulation is based on the comparison with the results of full-scale formulation (with taking into account equipment), as well as on the comparison with the relative displacements of two markers measured in experiments.

In the general case there is no symmetry in the problem (Fig. 8b) due to anisotropy of mechanical properties of single crystal sample. However in the important for practice case of [001] crystallographic orientation of sample the symmetry in respect to planes xz and yz (see Fig. 8a) can be introduced. Equipment and bolts are modeled by linear elastic material (steel), and for the sample elasto-visco-plastic model of material is used. The problem is solved in a three-dimensional quasi-static formulation. As boundary conditions the symmetry conditions are set: zero displacements on the y -axis on the xz plane and zero displacements on the x -axis on the yz plane. On the lower side of the equipment zero displacements along the x and z axes are set. On the bolt cap the pressure of 100 MPa has been applied that is equivalent to the tightening force of the bolt. The temperature boundary conditions are set from the experimental data at maximum and minimum temperature with linear interpolation in time. The mechanical properties for the alloys VZHM4 and VIN3 are taken from the papers [15,16] and for ZHS32 from [17] are presented in Tables 3-5. The mechanical properties of bolts are taken for pearlitic steel [9].

Table 3. Mechanical properties of VZHM4 used in simulations [15]

T	$^{\circ}\text{C}$	20	700	800	900	1000	1050
E_{001}	MPa	130000	101000	96000	91000	86000	82000
ν	-	0.39	0.42	0.422	0.425	0.428	0.43
α	1/K	$1.11 \cdot 10^{-5}$	$1.68 \cdot 10^{-5}$	$1.74 \cdot 10^{-5}$	$1.87 \cdot 10^{-5}$	$2.1 \cdot 10^{-5}$	$2.3 \cdot 10^{-5}$
σ_{Y001}	MPa	846	950	-	-	-	820
n	-	8	8	8	8	8	8
A	$\text{MPa}^{-n} \text{s}^{-1}$	$1 \cdot 10^{-42}$	$3 \cdot 10^{-31}$	$1 \cdot 10^{-29}$	$1 \cdot 10^{-28}$	$2 \cdot 10^{-27}$	$1 \cdot 10^{-26}$

Table 4. Mechanical properties of VIN3 used in simulations [16]

T	$^{\circ}\text{C}$	20	500	700	900	1000	1050
E_{001}	MPa	126000	110000	104000	89000	80000	75000
ν	-	0.39	0.41	0.42	0.42	0.425	0.428
α	1/K	$1.21 \cdot 10^{-5}$	$1.33 \cdot 10^{-5}$	$1.4 \cdot 10^{-5}$	$1.5 \cdot 10^{-5}$	$1.57 \cdot 10^{-5}$	$1.6 \cdot 10^{-5}$
σ_{Y001}	MPa	555	800	930	910	645	540
n	-	8	8	8	8	8	8
A	$\text{MPa}^{-n} \text{s}^{-1}$	$1 \cdot 10^{-42}$	$4 \cdot 10^{-34}$	$1.5 \cdot 10^{-30}$	$5.8 \cdot 10^{-27}$	$3.5 \cdot 10^{-25}$	$1.5 \cdot 10^{-24}$

Table 5. Mechanical properties of ZHS32 used in simulations [17]

T	$^{\circ}\text{C}$	20	700	800	900	1000	1050
E_{001}	MPa	137000	110000	105000	99800	94800	92300
ν	-	0.395	0.4248	0.4284	0.4317	0.4347	0.4361
α	1/K	$1.24 \cdot 10^{-5}$	$1.6 \cdot 10^{-5}$	$1.7 \cdot 10^{-5}$	$1.81 \cdot 10^{-5}$	$2.22 \cdot 10^{-5}$	$2.42 \cdot 10^{-5}$
σ_{Y001}	MPa	919	904	901	895	670	580
n	-	8	8	8	8	8	8
A	$\text{MPa}^{-n} \text{s}^{-1}$	$1 \cdot 10^{-42}$	$2.5 \cdot 10^{-31}$	$8.5 \cdot 10^{-30}$	$2 \cdot 10^{-28}$	$6 \cdot 10^{-27}$	$7 \cdot 10^{-26}$

In simplified formulation (see Fig. 8c) we consider only the sample without equipment, in which zero displacements on the symmetry planes xz and yz are set, the outer face of the sample parallel to the symmetry plane xz was fixed in the direction of the axis x . To exclude solid body motions, a number of points on this face are also fixed in the direction of the y and z axes.

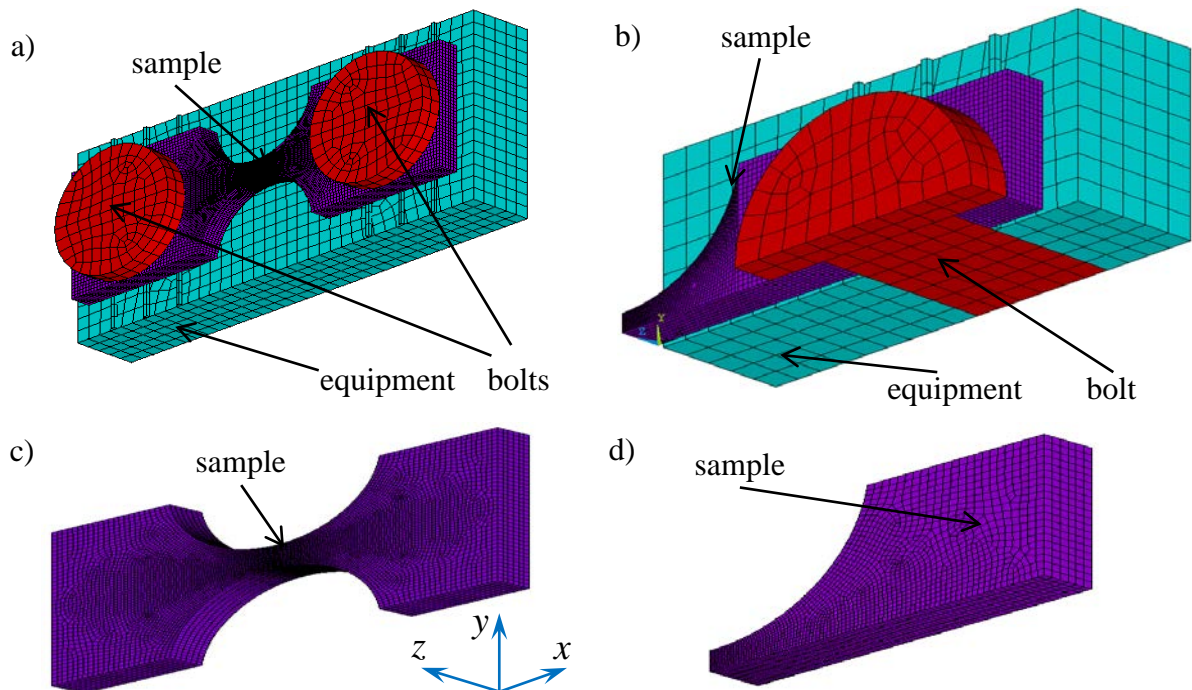


Fig. 8. FE models of the corset sample for thermo-elasto-visco-plastic problem solution:
 a) full model with taking into account equipment (no symmetry),
 b) model ($1/4$ due to symmetry) with taking into account equipment,
 c) simplified model without taking into account equipment (no symmetry),
 d) simplified model ($1/4$ due to symmetry) without taking into account equipment

Figure 9 shows distributions of plastic strain intensity field for three nickel superalloys and three different temperature modes after 7 cycles (for VZHM4 and VIN3 the effective length of the sample is 42 mm, for ZHS32 is 50 mm) obtained with using the FE model ($1/4$ due to symmetry) with taking into account equipment (Fig. 8b).

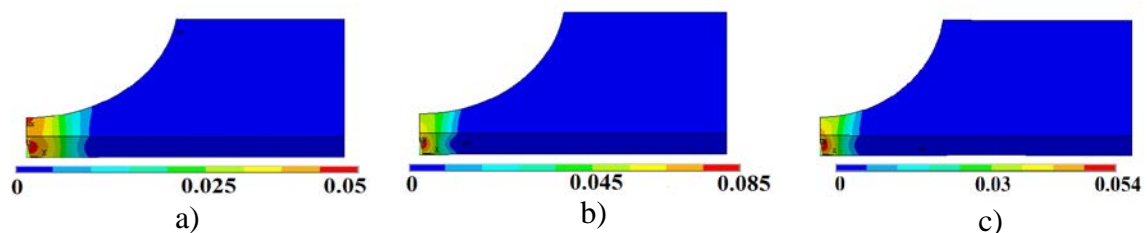


Fig. 9. Distributions of plastic strain intensity field after 7 cycles in the corset sample for:
 a) super alloy VZhM4, loading regime $700\div 1050^{\circ}\text{C}$;
 b) super alloy VIN3, loading regime $500\div 1050^{\circ}\text{C}$;
 c) super alloy ZhS32, loading regime $150\div 900^{\circ}\text{C}$

The Table 6 shows the equivalent (effective) length of the sample for the simplified formulation for different alloys, which has been found by the comparison with full model using the condition of equality of the inelastic strain ranges. FE simulations show that the

effective length doesn't depend on the type of hardening (isotropic and kinematic) and doesn't depend on temperature mode. In the FE simulations with acceptable engineering accuracy can be used the value 40 mm. Effective length takes into account the compliance of equipment and its variation in considered range has no appreciable on the results.

Table 6. The equivalent length of the corset sample for different alloys

VZHM4	VIN3	ZHS32
34-42 mm	38-46 mm	40-52 mm

4. Influence of the delay on the thermal fatigue durability

FE computations are carried out for a part of a corset sample (simplified FE model with effective length of sample equal 40 mm, see Fig. 8d). The temperature fields are set from the experimental data at maximum and minimum temperature cycle phase with using linear interpolation in time.

The influence of the delay at maximum temperature on the number of cycles to the formation of macrocrack is analyzed in the range from 1 min to 1 hour for the cyclic loading regimes with:

- maximum temperature of 1100°C and a temperature range of 900°C;
- maximum temperature of 1050°C and a temperature range of 550°C;
- maximum temperature of 1050°C and a temperature range of 350°C;
- maximum temperature of 1000°C and a temperature range of 750°C;
- maximum temperature of 900°C and a temperature range of 750°C.

The heating times in the cycle are 24s, 7s, 18 s, 28s, the cooling time are 15s, 15s, 40s, 52s for VZhM4. The heating time in the cycle is 10 s, the cooling time is 16s for VIN3. The heating times in the cycle is 25 s, the cooling time is 75s for ZhS32.

The mechanical properties for the alloys VZhM4 and VIN3 were taken from the papers [15], [16] and for ZhS32 from [17] (see also Tables 3-5).

The problem is solved in a quasi-static 3-dimensional formulation. The FE model is shown in Fig. 8d. The boundary conditions are zero displacements in the direction of the x -axis on two side faces of the sample with the normal along the x -axis. To exclude rigid body motions, a number of points on these faces in the direction of the y and z axes are also fixed.

Temperature evolutions in central point of sample with and without delay for loading regimes 700÷1050°C, 500÷1050°C, 250÷1000°C and 150÷900°C are presented schematically in Fig. 10.

Damage calculation and estimation of the number of cycles for the macrocrack initiation are made on the basis of four-member deformation criterion [3-5]:

$$D = \sum_{i=1}^N \frac{(\Delta \varepsilon_{eq_i}^p)^k}{C_1(T)} + \sum_{i=1}^N \frac{(\Delta \varepsilon_{eq_i}^c)^m}{C_2(T)} + \max_{0 \leq t \leq t_{\max}} \frac{\varepsilon_{eq}^p}{\varepsilon_r^p(T)} + \max_{0 \leq t \leq t_{\max}} \frac{\varepsilon_{eq}^c}{\varepsilon_r^c(T)}, \quad (11)$$

where the first term takes into account the range of plastic strain within the cycle, the second term deals with the range of creep strain within the cycle, the third term is unilaterally accumulated plastic strain (ratcheting), the fourth term is unilaterally accumulated creep strain. The number of cycles to initiate macrocrack N is determined from the condition $D = 1$. The equivalent strain for single crystal is defined by maximum shear strain in the slip system with normal to the slip plane $\mathbf{n}_{\{111\}}$ and the slip direction $\mathbf{l}_{\langle 011 \rangle}$:

$$\varepsilon_{eq} = \mathbf{n}_{\{111\}} \cdot \boldsymbol{\varepsilon} \cdot \mathbf{l}_{\langle 011 \rangle}. \quad (12)$$

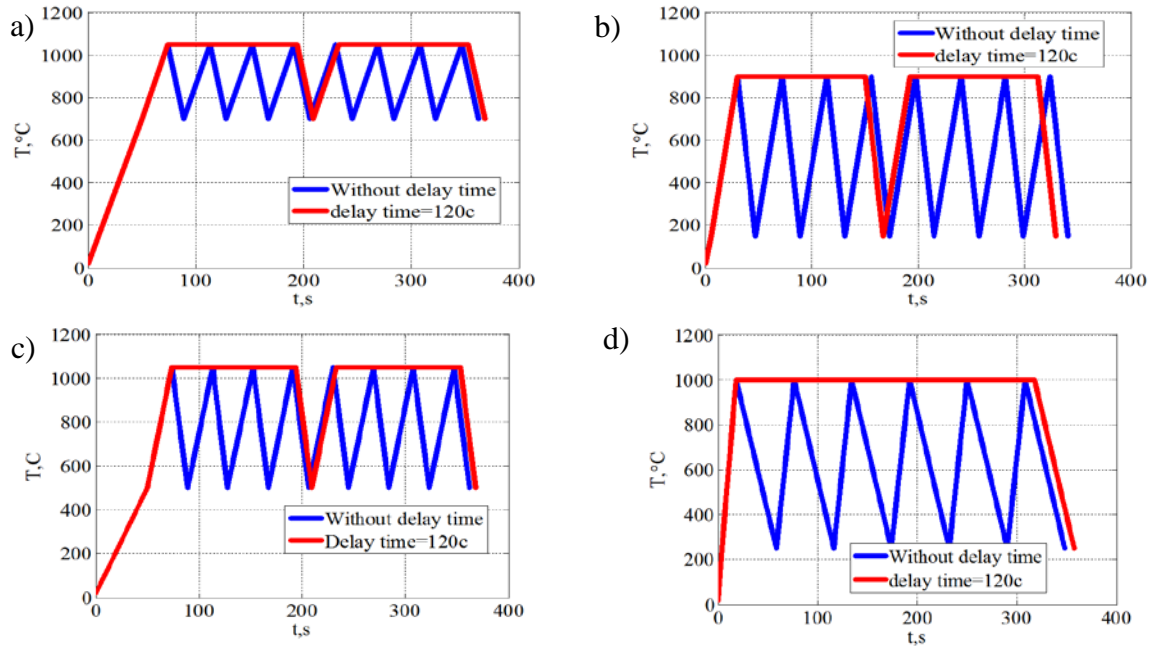


Fig. 10. Schematic presentations of temperature evolutions in central point of sample for loading regimes with and without delay:
a) 700÷1050°C; b) 150÷900°C; c) 500÷1050°C and d) 250÷1000°C

Usually it takes in (11) the values of constants: $k = 2$, $m = \frac{5}{4}$, $C_1 = (\varepsilon_r^p)^k$, $C_2 = (\frac{3}{4}\varepsilon_r^c)^m$, where ε_r^p and ε_r^c are ultimate strains of plasticity and creep under uniaxial tension. In the FE computations the values of ultimate strains $\varepsilon_r^p = \varepsilon_r^c = 17\%$ are used the same for all considered alloys. Improvement of the prediction accuracy of the delay time influence on durability can be achieved by the refinement of the constant strains ε_r^p on the basis of data without delay.

An analytical approximation of delay time influence in thermal fatigue strength has been proposed in the form:

$$N = N_{\min} + (N_0 - N_{\min}) \cdot e^{-t_{\text{delay}}/\tau}, \quad (13)$$

where N is the number of cycles to crack initiation as function of delay time t_{delay} , N_0 is the computational number of cycles in case without delay time, N_{\min} is the number of cycle in case with delay time is equal to 1 hour, τ is a constant (50 s for all considered materials). Comparison of results of FE simulations with experimental data for single-crystal superalloys VZhM4, VIN3 and ZhS32 is given in Fig. 11. The good agreement between computational and experimental results is observed.

Comparison of results of FE simulations and analytical approximation (13) concerning the effect of the delay time at the maximum temperature on the thermal fatigue durability for single-crystal superalloys VZhM4, VIN3 and ZhS32 is given in Fig. 12. Small deviations are observed only in the vicinity of the region of maximum curvature.

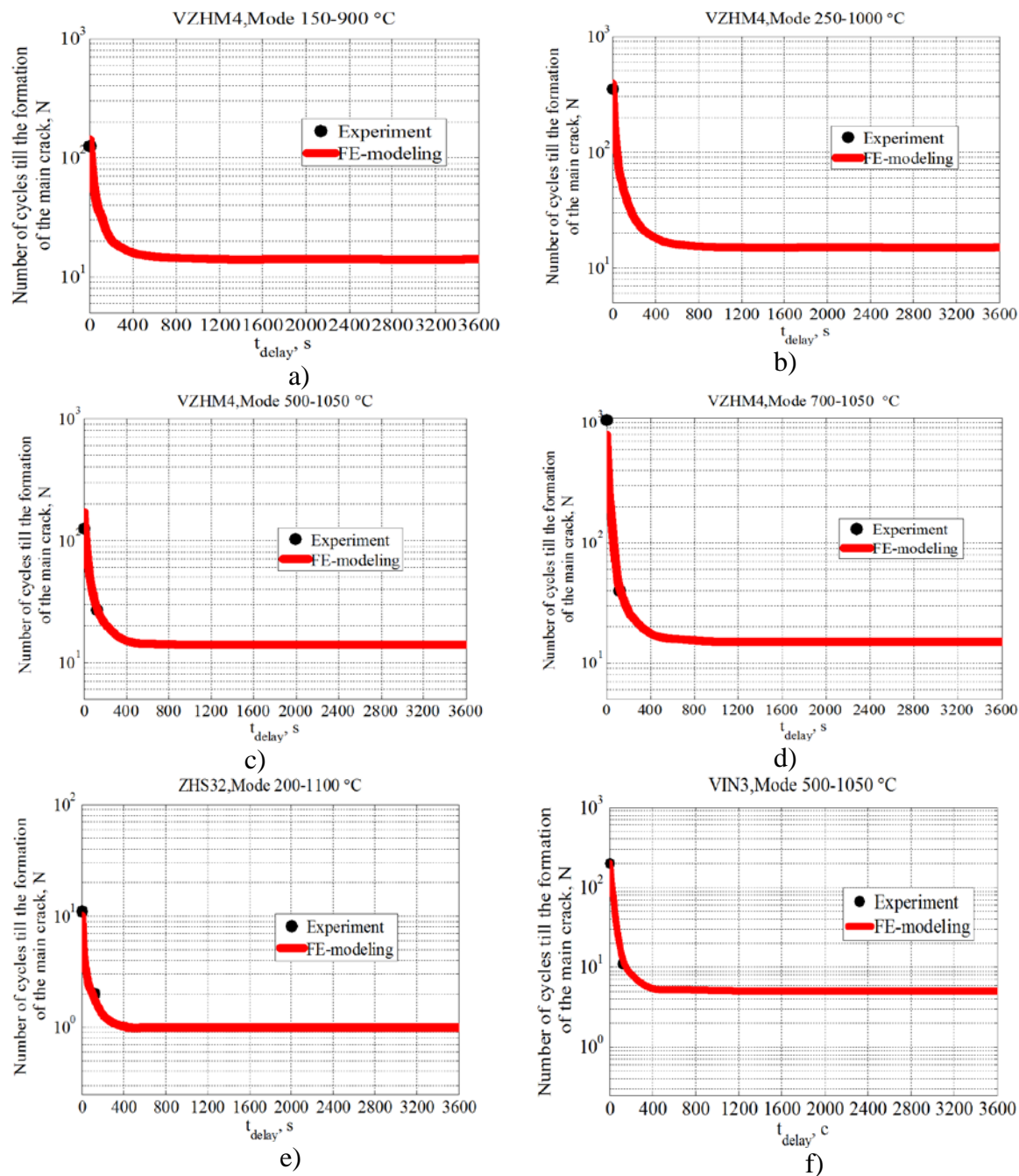


Fig. 11. Comparison of results of FE simulations and experimental data for alloys:

- VZhM4, loading regime 150÷900°C, a heating time is 28 s, a cooling time is 52 s;
- VZhM4, loading regime 250÷1000°C, a heating time is 18 s, a cooling time is 40 s;
- VZhM4, loading regime 500÷1050°C, a heating time is 24 s, a cooling time is 15 s;
- VZhM4, loading regime 700÷1050°C, a heating time is 7 s, a cooling time is 15 s;
- ZhS32, loading regime 200÷1100°C, a heating time is 25 s, a cooling time is 75 s;
- VIN3, loading regime 500÷1050°C, a heating time is 10 s, a cooling time is 16 s

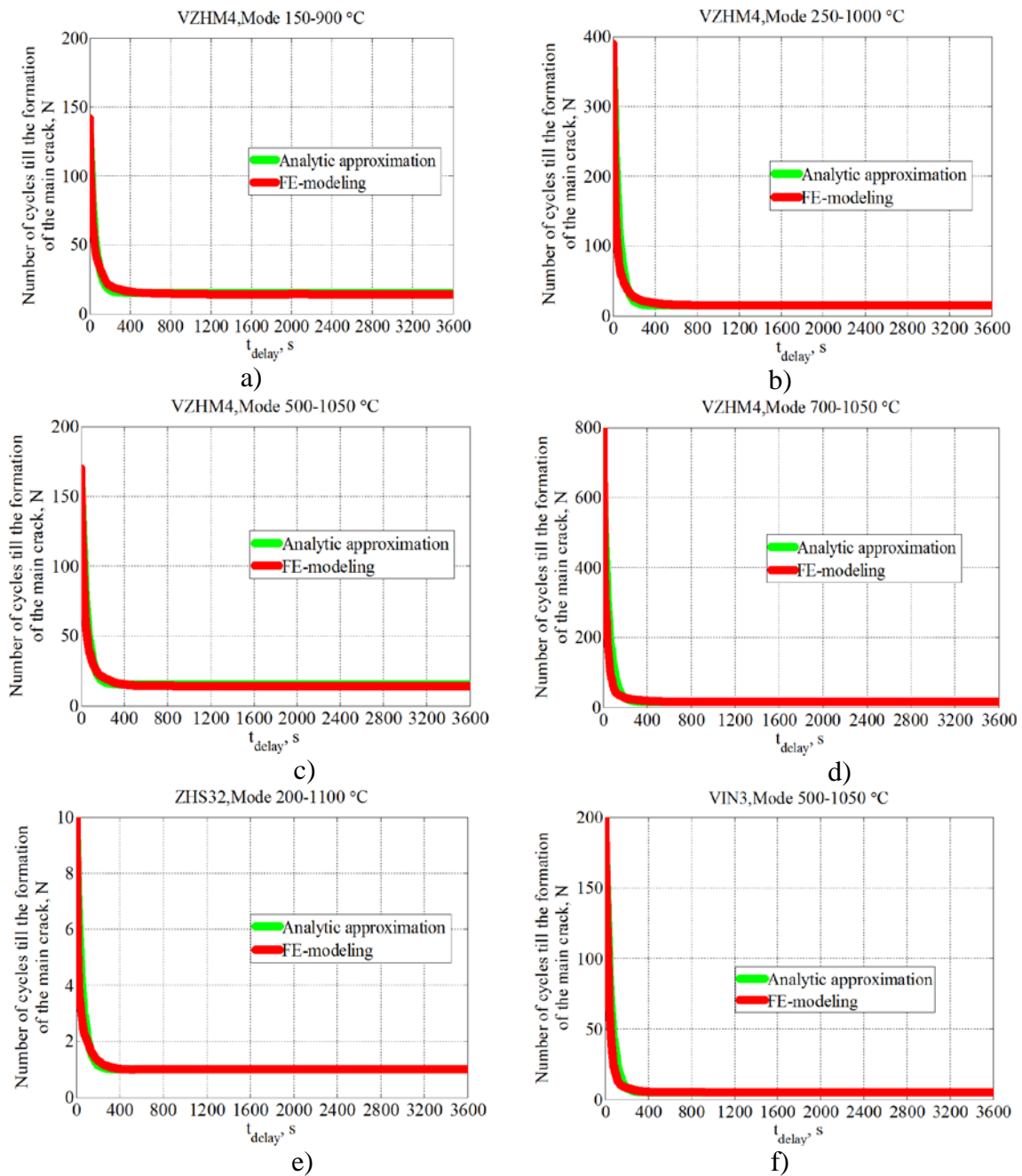


Fig. 12. Comparison of results of FE simulations and analytical approximation (13) for alloys:

- VZhM4, loading regime 150÷900°C, a heating time is 28 s, a cooling time is 52 s;
- VZhM4, loading regime 250÷1000°C, a heating time is 18 s, a cooling time is 40 s;
- VZhM4, loading regime 500÷1050°C, a heating time is 24 s, a cooling time is 15 s;
- VZhM4, loading regime 700÷1050°C, a heating time is 7 s, cooling time is 15 s;
- ZhS32, loading regime 200÷1100°C, a heating time is 25 s, a cooling time is 75 s;
- VIN3, loading regime 500÷1050°C, a heating time is 10 s, a cooling time is 16 s

5. Conclusions

The results of thermal and stress-strain state simulations for single-crystal corset specimens under cyclic electric heating show a good agreement with the experimental data for a wide range of temperature alteration and different single-crystal nickel based superalloys. Obtained results point out on the possibility of predicting thermal fatigue durability for single crystal by

means of thermo-electro-mechanical finite-element simulation with using of four-member deformational criterion of damage accumulation and microstructural models of inelastic deformation.

A systematic numerical analysis of the delay effect at maximum temperature on thermal fatigue durability was carried out for various single-crystal superalloy samples in wide range temperatures. The simplified analytic approximation for durability curves are proposed on the base of results of multivariate computational experiments.

Acknowledgments. Research was conducted under the financial support of the Russian Science Foundation, Grant no. 18-19-00413.

References

- [1] Shalin RE, Svetlov IL, Kachanov EB, Toloraiya VN, Gavrilin OS. *Single crystals of nickel heat-resistant alloys*. Moscow: Mashinostroenie; 1997. (In Russian)
- [2] Getsov LB. *Materials and strength of gas turbine parts*. Rybinsk: Gazoturbinnye Tekhnologii; 2010. (In Russian)
- [3] Getsov LB, Semenov AS. Criteria of fracture of polycrystalline and single crystal materials under thermal cyclic loading. In: *Proceedings of CKTI. Vol. 296*. 2009. p.83-91.
- [4] Semenov AS, Getsov LB. Thermal fatigue fracture criteria of single crystal heat-resistant alloys and methods for identification of their parameters. *Strength of Materials*. 2014;46(1): 38-48.
- [5] Getsov LB, Semenov AS, Staroselsky A. A failure criterion for single-crystal superalloys during thermocyclic loading. *Materials and technology*. 2008;42(1): 3-12.
- [6] Petrushin NO, Logunov AV, Kovalev AI, Zverev AF, Toropov VM, Fedotov NH. Thermophysical properties of Ni₃Al-Ni₃Nb directly crystallized eutectic composition. *High temperature thermophysics*. 1976;14(3): 649-652.
- [7] Zinoviev VE. *Thermo-physical properties of metals at high temperatures*. Moscow: Metallurgia; 1989. (In Russian)
- [8] Chirkin VS. *Thermophysical properties of nuclear materials*. Moscow: Atomizdat; 1968. (In Russian)
- [9] Maslenkov SB, Maslenkova EA. *Steels and alloys for high temperatures*. Moscow: Metallurgia; 1991. (In Russian)
- [10] Courant R, Hilbert D. *Methods of mathematical physics. Vol. 2*. Leningrad: GTTI; 1945.
- [11] Semenov AS. PANTOCRATOR – finite-element program specialized on the solution of non-linear problems of solid body mechanics. In: *Proc. of the V-th International. Conf. "Scientific and engineering problems of reliability and service life of structures and methods of their decision"*. Saint Petersburg: Izd-vo SPbGPU; 2003. p.466-480.
- [12] Cailletaud GA. Micromechanical approach to inelastic behaviour of metals. *Int. J. Plast.* 1991;8(1): 55-73.
- [13] Semenov AS. Identification of anisotropy parameters of phenomenological plasticity criterion for single crystals on the basis of micromechanical model. *Scientific and technical sheets SPbGPU. Physical and mathematical Sciences*. 2014;2(194): 15-29. (In Russian)
- [14] May S, Semenov AS. Modeling of inelastic cyclic deformation of monocrystalline specimens. In: *Proc. of the XXXIX week of science of SPbPU. Vol. 5*. 2010. p.73-74. (In Russian)
- [15] Kablov EN, Petrushin NO, Svetlov IL, Demonis IM. Nickel casting heat-resistant alloys of the new generation. In: *The jubilee nauch.-tech. sat. Aviation materials and technologies*. Moscow: Proceedings of VIAM; 2012. p.36-52. (In Russian)
- [16] Semenov SG, Getsov LB, Semenov AS, Petrushin NV, Ospennikova OG, Zhivushkin AA. The issue of enhancing resource capabilities of nozzle blades of gas turbine

engines through the use of new single crystal alloy. *Journal of Machinery Manufacture and Reliability*. 2016;4: 30-38.

[17] Getsov LB, Semenov AS, Tikhomirova EA, Rybnikov AI. Thermocyclic and static failure criteria for single crystal superalloys of gas turbine blades. *Materials and technology*. 2014;48(2): 255-260.

NUMERICAL METHOD OF SINGLE-CRYSTAL TURBINE BLADE STATIC STRENGTH ESTIMATION TAKING INTO ACCOUNT PLASTICITY AND CREEP EFFECTS

Boris Vasilyev^{*}, Alexander Selivanov

CIAM, Moscow, 2, Aviamotornaya street, Russia

BMSTU, Moscow, 5, Baumanskaya 2-ya street, Russia

*e-mail: bevasilev@ciam.ru

Abstract. To increase the reliability of single-crystal blade durability estimations a phenomenological model of single crystal superalloy plasticity based on the use of an “equivalent” direction and its software implementation has been developed. The relative orientation between principal stresses and single-crystal (SX) axes is considered by this direction. In order to study the effect of crystallographic orientation (CO) on the characteristics of a single-crystal material, a series of tests was carried out at various temperatures under tension under conditions of short-term and long-term loading. The possibility of using linear interpolation to determine the characteristics of plasticity and creep for intermediate CO has been confirmed. An example is given of using the developed calculation method in the Finite Element Analysis Software CalculiX using the model blade as an example.

Keywords: single-crystal, crystallographic orientation, anisotropy, stress-strain state, plasticity, creep

1. Introduction

The production of new gas-turbine engines for aviation is largely determined by the development of new heat-resistant materials with enhanced strength characteristics. The engine thrust, characteristics of its efficiency and weight and dimensions primarily depend on the turbine inlet gas temperature. This requires an increase in the performance characteristics of the engine part materials, turbine blades in particular.

Turbine blades are increasingly being made of single crystal nickel-based superalloys (SCNBS). These superalloys were developed to provide superior creep, stress rupture, melt resistance, and thermomechanical fatigue capabilities over polycrystalline alloys previously used in the production of turbine blades and vanes.

To adequately define the stress-strain state (SSS) of blades, it is essential to perform strength calculations taking material anisotropy and the physical and geometrical non-linear effect into account. There are two main ways to obtain elastic-plastic SSS of single crystal (S) superalloys. Comparison of those ways can be found in [1].

The first one is a "crystallographic approach" based on Schmid's law according to which when the resolved shear stress on a slip system reaches a critical value, plastic strains occurs [2-9].

The second approach is based on the use of different phenomenological models. The best known theory for anisotropic materials is the Hill plasticity model that was proposed in 1947 for orthotropic materials and implemented in well-known Finite Element

Analysis (FEA) Software (ANSYS, ABAQUS, MSC Nastran, etc). Hill's yield criterion, which can be considered a generalization of the von Mises criterion, relates yield strength in different directions to a reference yield stress. Creep response can also be described using the Hill model. A detailed description is given in [10-13].

There are no plasticity and creep models of SC material in the popular FEA software. The goal of this study was to develop one. Such models have to be physically-based and readily implementable, but also should not be expensive or time-consuming while obtaining the necessary experimental data.

2. Methods

This paper focused on the following topics:

- Experimental investigation of alloy behavior.
- Plasticity and creep model development and their program implementation.
- Single Crystal blade calculation.

Experimental Studies. In order to study the effect of CO on the characteristics of a SCNBS, a series of tests was carried out at various temperatures for a Russian alloy: tensile test under conditions of short-term and long-term loading. Additionally, torsion tests were conducted at room temperature.

All experiments were carried out for four different COs: [001], [011], [111], [012]. It should be noted that samples with intermediate orientation [012] were tested to check the hypothesis of piecewise linear interpolation of properties, which will be described in more detail later. Fig. 1, 2 show a view of SCNBS specimens.



Fig. 1. Specimens for tensile test

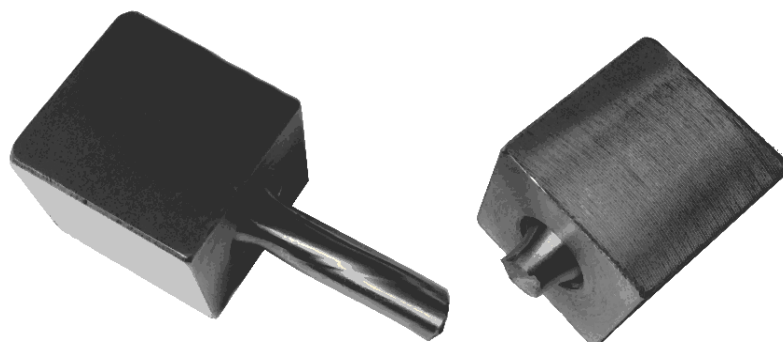


Fig. 2. Specimen after torsion test

Plasticity and Creep Models and Their Program Implementation. SX are characterized by a cubic symmetry of properties, i.e. the crystallographic lattice has three mutually orthogonal planes of symmetry (Fig. 3). One can distinguish three mutually perpendicular directions for which the properties are equal. There are three main families of Crystallographic directions that are vertices of a stereographic triangle: $\langle 001 \rangle$, $\langle 011 \rangle$,

$\langle 111 \rangle$ (Fig. 3).

The suggested approach incorporates the cubic symmetry of SX using the generalized Hooke's law:

$$\{\sigma\} = [C]\{\varepsilon\} \text{ or } \{\varepsilon\} = [S]\{\sigma\}, \quad (1)$$

where $\{\sigma\}$, $\{\varepsilon\}$ are tensors of stress and strains and $[C]$, $[S]$ are 4th order tensors of stiffness and compliance.

The elastic properties of SCNBS exhibit cubic symmetry, also described as cubic syngony. The elastic properties of materials with cubic symmetry can be described with three independent constants of the elastic stiffness matrices, C_{11} , C_{12} , ..., C_{44} or the elastic compliances S_{11} , S_{12} , ..., S_{44} (After transition from the tensor notation to the matrix one).

$$[C] = \begin{bmatrix} C_{11} & C_{12} & C_{12} & 0 & 0 & 0 \\ C_{12} & C_{11} & C_{12} & 0 & 0 & 0 \\ C_{12} & C_{12} & C_{11} & 0 & 0 & 0 \\ 0 & 0 & 0 & C_{44} & 0 & 0 \\ 0 & 0 & 0 & 0 & C_{44} & 0 \\ 0 & 0 & 0 & 0 & 0 & C_{44} \end{bmatrix}.$$

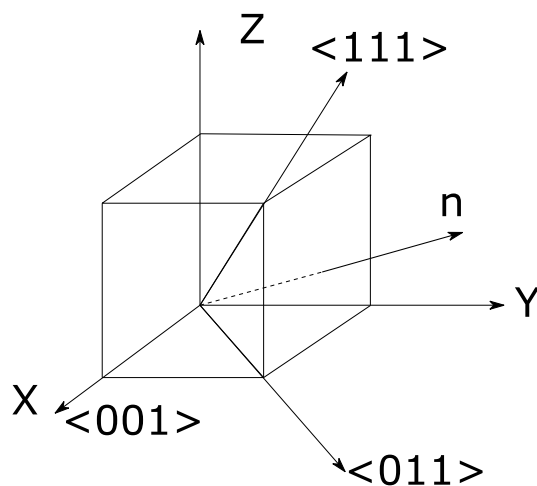


Fig. 3. Single Crystal Axes

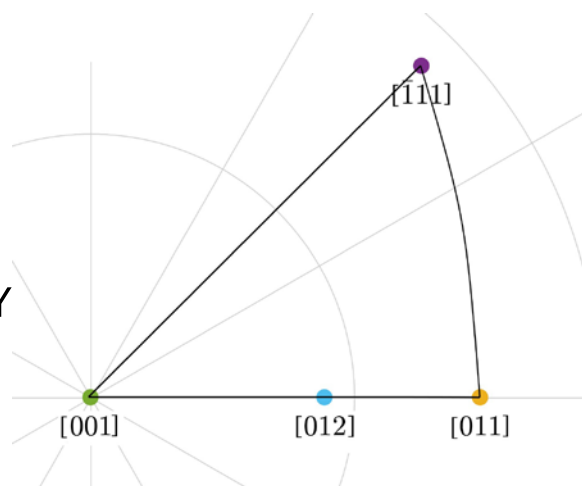


Fig. 4. Stereographic triangle

To determine the elastic modulus in an arbitrary crystallographic direction \vec{n} , the dependence is used:

$$E_n = \frac{1}{S_{11} - 2\left(S_{11} - S_{12} - \frac{1}{2}S_{44}\right)L}, \quad (2)$$

where L characterizes the direction of \vec{n} with respect to the axes of the SX (Fig. 2) and is equal to zero in the directions $\langle 001 \rangle$ and reaches a maximum value of $\frac{1}{3}$ in the $\langle 111 \rangle$ direction.

$$L = l_1^2 l_2^2 + l_2^2 l_3^2 + l_3^2 l_1^2, \quad (3)$$

where, $l_1 = \cos(\vec{n} \wedge X)$, $l_2 = \cos(\vec{n} \wedge Y)$, $l_3 = \cos(\vec{n} \wedge Z)$ - direction cosines. This dependence can be shown as a graph (Fig. 5).

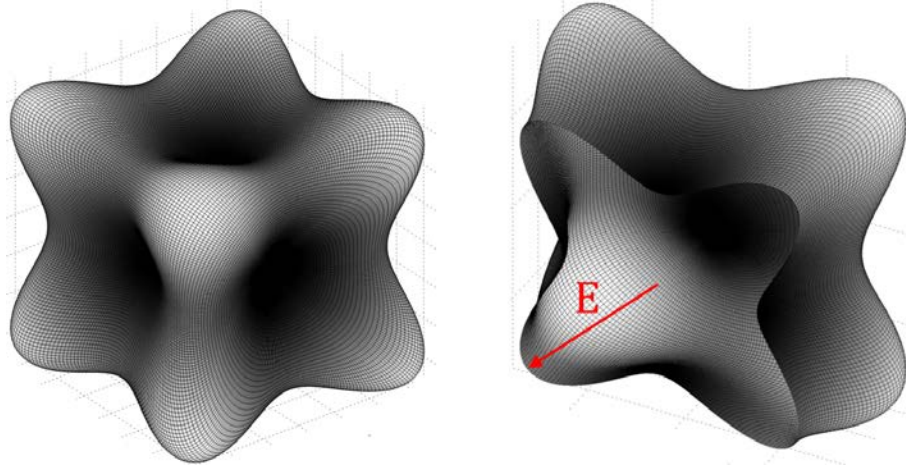


Fig. 5. The glyph represented elastic anisotropy

A yield surface is a map in stress space, in which an inner envelope is drawn to demarcate elastic regions from yielded regions. The yield criterion for polycrystalline material could be written as follows:

$$f = \sigma_e - \sigma_Y(T), \quad (4)$$

where σ_e is the equivalent stress and σ_Y represents the yield strength. A whole range of multiaxial yield criteria exist. The most commonly used criterion in engineering practice, particularly for FE computational analysis, is that of von Mises and Tresca.

For anisotropic materials, the yield surface is much more complicated than for isotropic materials. It is necessary to consider the orientation of the stress state relative to the axes of SX and mechanical properties in different directions. This could be written as follows:

$$F = f(\sigma_1, \sigma_2, \sigma_3, \sigma_Y, \alpha, \beta, \gamma) = 0, \quad (5)$$

where α , β , and γ are the angles characterizing the position of the principal stress axes relative to the main coordinate system. There are number of yield criterion of anisotropic bodies, but their distinctive feature is the complexity of the yield surface (i.e, a function of the equivalent stress).

For the calculations of the elastic-plastic stress-strain state (SSS) by the finite element method for a single-crystal alloy, the authors proposed [1] a plasticity criterion:

$$f = \sigma_e - \sigma_Y(\gamma, T), \quad (6)$$

where γ is the relative orientation between principal stresses and SX axes, T is the temperature, σ_e is equivalent stresses. Stresses by von Mises, Tresca, and unifying them, the Hosford, could be considered as equivalent.

The value of the orientation factor L (3) of the equivalent direction \vec{T} (Fig. 6), determined by (7), is taken in the present study as parameter γ .

$$\vec{T} = \sigma_1 \vec{e}_1 + \sigma_2 \vec{e}_2 + \sigma_3 \vec{e}_3. \quad (7)$$

Using this value, the yield strength, as well as other mechanical properties (ultimate tensile strength, elongation) defining the deformation curve for the given SSS and temperature (Fig. 7), is calculated for temperature T . The use of piecewise linear dependence is suggested in this study. Elastic modulus is calculated by (2). After determination of the specified parameters, a deformation curve is constructed. It should be noted that tangent modulus is the function of yield strength, ultimate tensile strength, elongation and therefore depends on L .

Many studies have been done on tension/compression asymmetry in the mechanical characteristics of SCNBS [7,14], where authors have shown that this difference can be significant. The suggested approach assigns a sign to equivalent stresses by the sign of mean

normal stress:

$$\sigma_m = \frac{(\sigma_1 + \sigma_2 + \sigma_3)}{3}. \quad (8)$$

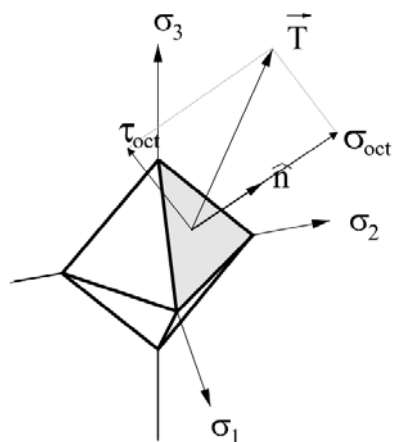


Fig. 6. Equivalent direction

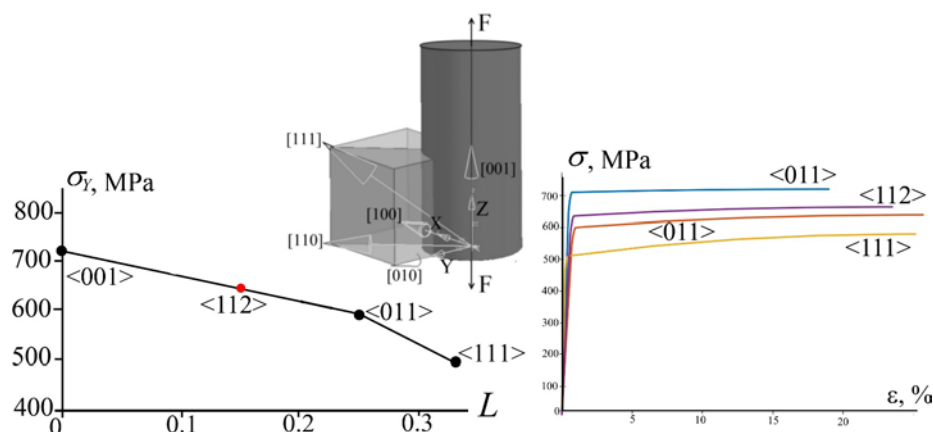


Fig. 7. Yield strength dependence on L

In order to consider tension/compression asymmetry, the suggested approach allows us to input asymmetry coefficient as a function of temperature and crystallographic direction. It

is an experimentally determined ratio $k_{ac} = \frac{\sigma_Y^{tens}}{\sigma_Y^{compr}}$.

Developed approach allows us to consider the effects of variations of the relative orientation between crystal axes and blades axes on SSS. This approach can be easily reduced to the level of isotropic materials. The computational procedure of SX turbine blade SSS determination using the proposed approach consists of the following steps:

- mechanical FEA produces trial stresses and strains;
- the routine computes the equivalent direction \bar{T} (7) and its orientation factor L (3) in every integration point of FEM;
- by the value of L , the routine computes material properties defining the deformation curve (yield and ultimate strength, elongation) at every integration point of FEM with its temperature;
- the routine computes the sign of mean normal stress (8);
- in case of a negative value of mean normal stress, the routine adjusts the values of the yield strength (in the case of available data on the characteristics of asymmetry);

- the routine checks the yield criterion (6) for every integration point of FEM;
- the routine constructs the deformation curve $\sigma = f(\varepsilon)$ for integration points where $\sigma_e \geq \sigma_Y$;

- the routine determines the elastic-plastic SSS.

Results of experimental and numerical checking of this approach shown good feasibility [16].

Developed creep subroutine deals with the anisotropy in similar way. By linear interpolation between values for the main CO (<001>, <011>, <111>) routine constructs creep curve for temperature, stress, accumulated state variable, and relative orientation between crystal and blade axes.

Construction of creep curves is carried out using Larson-Miller curves at every integration point with the temperature T and stress σ_e .

$$P_{LM} = T(\log_{10} t + C), \quad (9)$$

where C – material constant, usually 20; t – life, hr.

For isotropic materials, results of this model were compared with experimentally obtained results of High Pressure Turbine (HPT) blade damage and deformation. It was shown that numerical predictions were correct [15].

A feature of this material model is the need to identify the starting point on the creep curve for the calculation of creep. Such an identifier is the accumulated equivalent plastic strain at the stage of elastoplastic calculation. That is, plastic and creep strain are related quantities.

The proposed plasticity and creep models were implemented in the open-source FEA software CalculiX. Modifications were made to the program modules responsible for the physical nonlinearity of the material [16].

Single Crystal blade calculation. The calculations of SSS and static strength on the design mode of the HPT SX model blade with and without anisotropy were carried out for the comparison of strength characteristics. All strength calculations were carried out by three-dimensional finite element method. Operation time on design mode is 100 hours.

Figure 8 shows FEM of the model blade. Figure 9 shows temperature distribution along blade.

The strength calculations of the blade were carried out step by step: at the first stage, the SSS was determined in the elastic-plastic formulation considering the anisotropy of the elastic and plasticity characteristics; at the second, the problem of determining the kinetics of the SSS due to creep (stress relaxation) was solved.

The blade was fixed on the contact edges of the shank. The safety factor value of long-term static strength (K_m) can be determined by the equation:

$$K_m = \frac{\sigma_r(T, t, \bar{T})}{\sigma_{eqv}^t}, \quad (10)$$

where σ_r – creep strength, determined for a given temperature, duration and equivalent direction; σ_{eqv}^t – equivalent in time stress. This stress leads to the same damage as constantly changing due to creep stress.

One of the issue when equation (10) is used is to take into account equivalent direction changing due to creep. Below we will compare results for two variants of calculation of safety factor with and without consideration of the changes in L . Average integral is being used for such purpose.

It should be noted that K_m is connected to the lifetime safety factor according to

formula $K_t = (K_m)^m$, where m – is the parameter characterizing the slope of the long-term static strength curve.

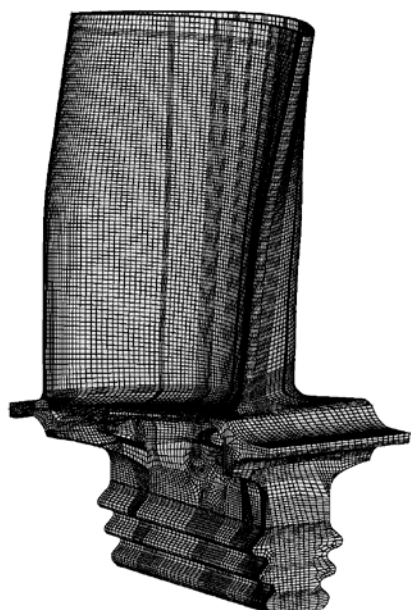


Fig. 8. FE Model

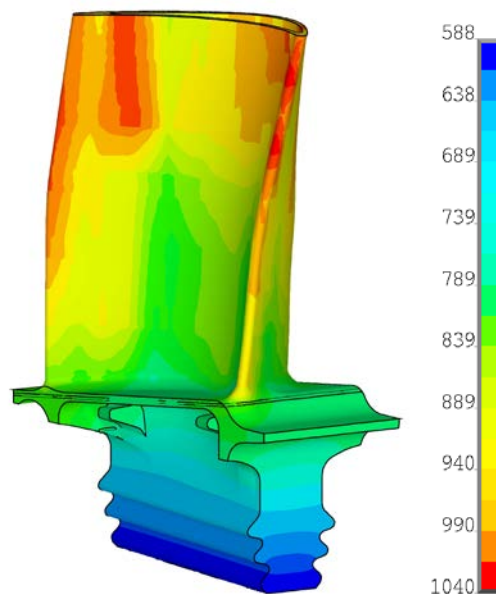


Fig. 9. Temperature distribution, °C

3. Results

Experimental Studies. Torsion and tension experiments of smooth cylindrical specimens of various COs ([001], [011], [111], [012]) were carried out. The deformation curves are presented in Figs. 10, 11. There is a strong anisotropy of the properties of both tensile and torsion during the transition from one CO to another (Table 1).

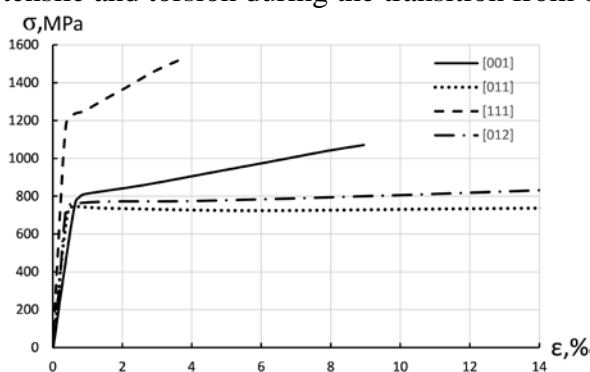


Fig. 10. Deformation Curve at 20°C

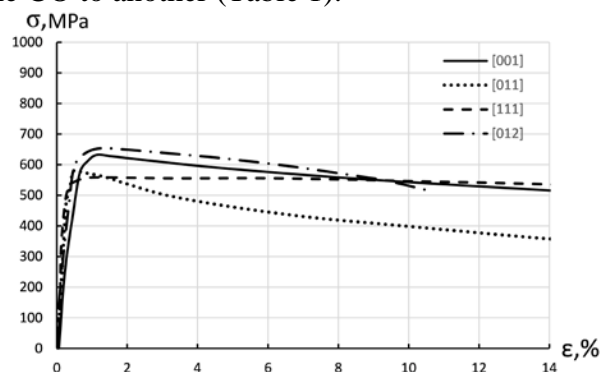


Fig. 11. Deformation Curve at 1000°C

Table 1. Experimental results

CO	E, GPa	G, GPa
[001]	130	77
[011]	236	41
[111]	325	42
[012]	246	53

Creep strength anisotropy was experimentally investigated for the same SCNBS in this study. The investigation was carried out in a wide range of stresses and temperatures. As expected, creep characteristics are highly dependent on CO. Figure 12 shows some of the results of creep tests. Figure 13 shows Larson-Miller curves.

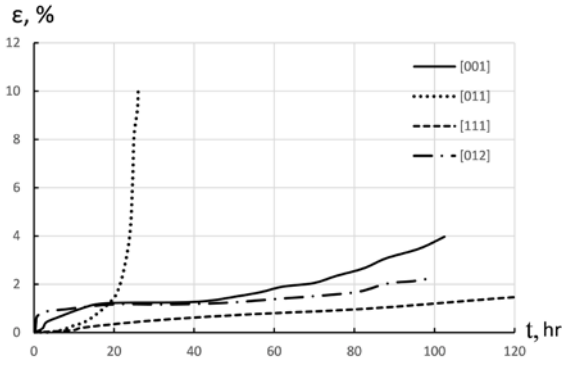


Fig. 12. Creep Curves at $T=950^{\circ}\text{C}$, $\sigma=314\text{ MPa}$

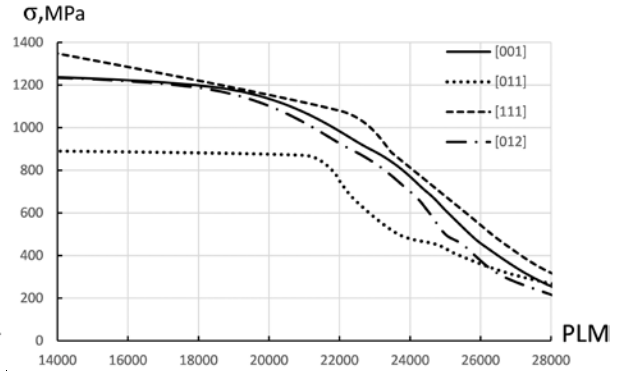


Fig. 13. Larson-Miller curves

Analysis of the results showed that CO [011] is the least favorable in terms of strength characteristics.

Proposed models based on the hypothesis of the possibility of using piecewise linear interpolation of properties in stereographic triangle using orientation factor L . The validity of the accepted hypothesis was tested. Figures 14, 15 show the dependence of yield and ultimate strengths on the orientation factor (L), where the values are 0.0, 0.16, 0.25, 0.33, corresponding to the [001], [012], [011], [111] orientations, respectively.

It is shown that the data for the yield strength and ultimate stress for the intermediate orientation [012] ($L = 0.16$) are in satisfactory agreement with the hypothesis of linear interpolation of properties between the main CO ([001], [011], [111]), nevertheless it is recommended to obtain material properties in intermediate COs.

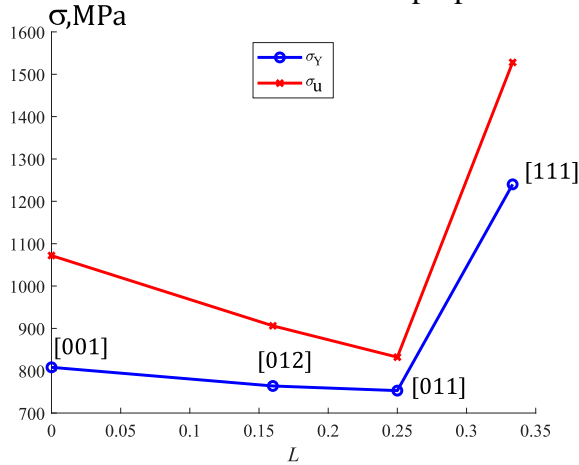


Fig. 14. The value of yield strength dependence on L for 20°C

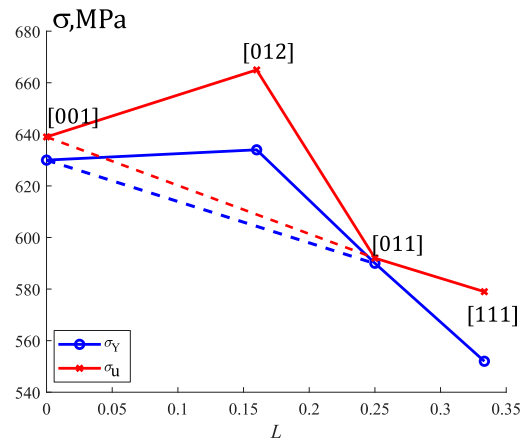


Fig. 15. The value of yield strength dependence on L for 1000°C

Finite Element Analyses of Turbine Blade. Figures 16, 17 show distribution on the isotropic blade von Mises stress and the local safety factor. "Dangerous" zones with low values of safety factor values are marked by numbers 1,2. First zone is the zone with maximal temperature, second zone is the zone with minimal safety factor value.

After the calculations, the processing of their results was carried out and the magnitudes of changes in the values of stresses and safety factors were found in case of taking into account anisotropy. To do this, we used the following relationship.

$$\Delta\sigma_{eqv}^{-t} = \frac{\sigma_{eqv}^{iso_t} - \sigma_{eqv}^{aniso_t}}{\sigma_{eqv}^{iso_t}}, \tag{11}$$

$$\overline{\Delta K}_m = \frac{K_m^{iso} - K_m^{aniso}}{K_m^{iso}}. \tag{12}$$

A negative value means a decrease in magnitude in case of anisotropy consideration.

Figures 18, 19 show distribution on the blade differences of the results. Table 1 shows results for two calculation with and without anisotropy consideration in "dangerous" zones, where σ_0 – von Mises stress at the end of elastoplastic strain; σ_{end} – von Mises stress after 100 hr of working on regime; σ_{eqv}^t – equivalent in time von Mises stress.

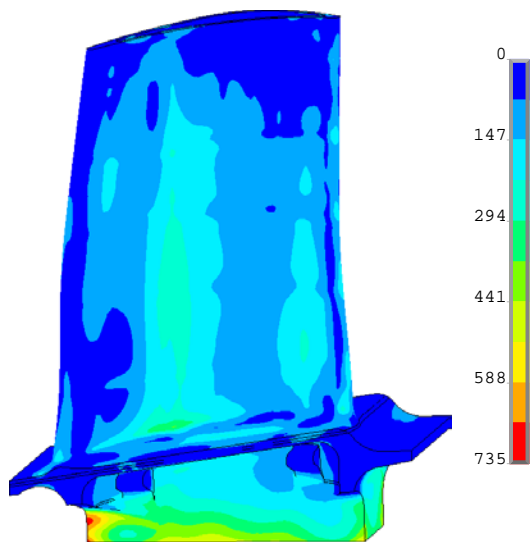


Fig. 16. Distribution of σ_0 , MPa

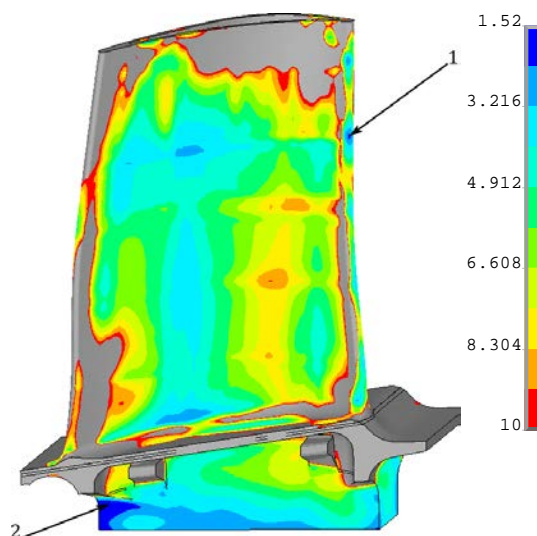


Fig. 17. Distribution of K_m

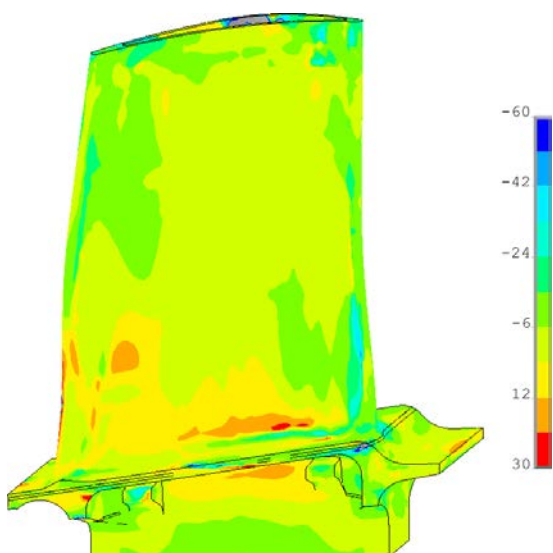


Fig. 18. Distribution of $\Delta\sigma_{eqv}^t$, %

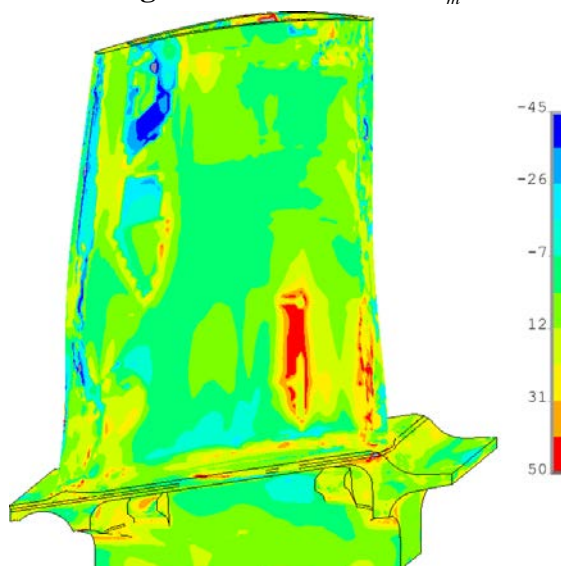


Fig. 19. Distribution of $\overline{\Delta K}_m$, %

Analysis of the results showed that when anisotropy is taken into account, the values of the estimated safety margins decreases by 20-30%. That means underestimation of the estimated life by 300-400%. It is also worth noting that the change in safety factor values is more significant than the change in stress values.

Table 2. Calculation results

Model	Zone, #	T, °C	L	σ_0 , MPa	σ_{end} , MPa	σ'_{eqv} , MPa	σ_r , MPa	K_m	Δ , %
Iso	1	1032	0.20	163	63	96	255	2.65	-
Aniso			0.19	178	71	104	288	2.76	4
Aniso*			0.10				256	2.46	-7
Iso	2	722	0.19	584	567	569	992	1.74	-
Aniso			0.20	697	628	641	813	1.27	-27
Aniso*			0.20				814	1.27	-27

*equivalent direction changing due to creep consideration

Figures 20, 21 show relaxation curve for zone #1, 2.

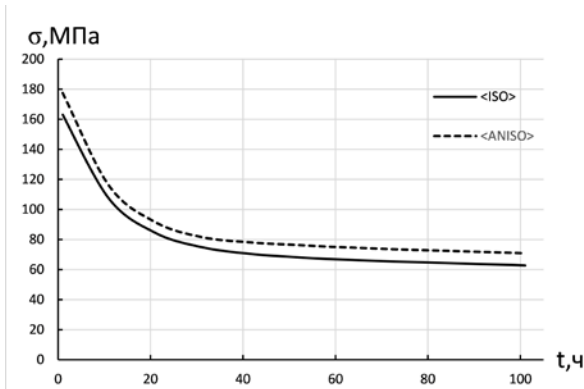


Fig. 20. Relaxation curve (zone #1)

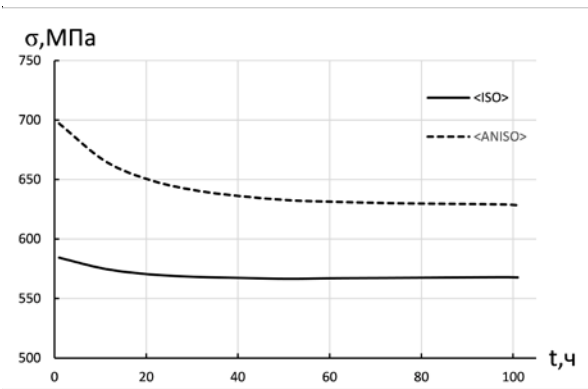


Fig. 21. Relaxation curve (zone #2)

4. Discussion

The analysis of the results showed that blade needs to be considered anisotropic. Figure 20 shows histogram of $\Delta \bar{K}_m$. For the considered blade under the given conditions and loads, it was shown that ignoring the anisotropy can lead to an underestimation of the estimated durability by 300-400%.

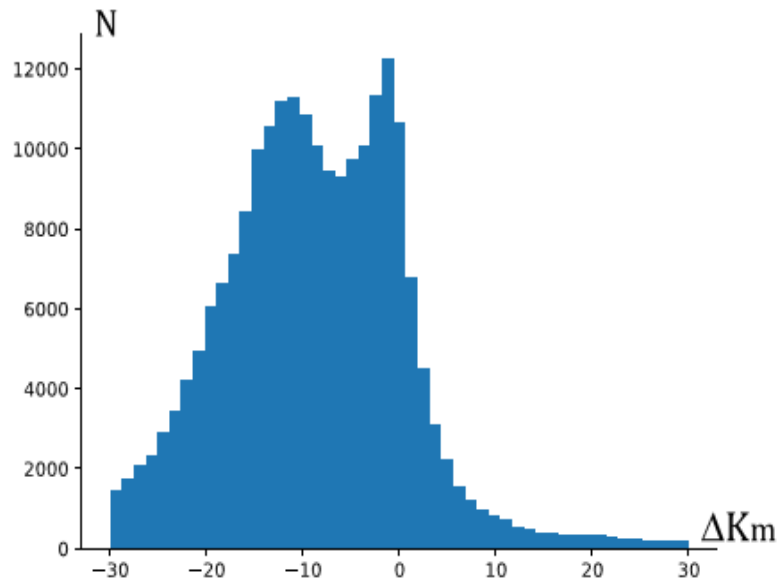


Fig. 22. Histogram of $\Delta \bar{K}_m$, %

It should be noted that this blade is characterized by a relatively simple cooling system

and a relatively simple stress state. When considering blades with a more complex cooling system, the difference in results may be even more significant. The direction of further research is the development of a method for assessing the cyclic durability of single-crystal turbine blades.

5. Conclusions

Based on the research results, the importance of taking into account the anisotropy of characteristics and the complex stress state when calculating the static strength of SX turbine blades is shown. To consider this a phenomenological model based on equivalent direction of stress state is proposed. Changing of equivalent direction due to creep should be considered.

In addition, necessity of obtaining characteristics in intermediate CO's is shown.

Acknowledgements. Authors wishing to acknowledge assistance of colleagues that helped with experimental investigation: Mikhail Volkov, Alexander Demidov and Elena Bredikhina.

References

- [1] Vasilyev BE. Stress-Strain State Prediction of High-Temperature Turbine Single Crystal Blades Using Developed Plasticity and Creep Models. In: *Proceedings of the GT201425229 ASME Turbo Expo 2014*. American Society of Mechanical Engineers; 2014. p. V07AT29A005|V07AT29A005.
- [2] Tinga T. *Multiscale modelling of single crystal superalloys for gas turbine blades*. Eindhoven: Technische Universiteit Eindhoven; 2009.
- [3] Ramaglia AD, Villari P. Creep and Fatigue of Single Crystal and Directionally Solidified Nickel-Base Blades via a Unified Approach Based on Hill48 Potential Function: Part 1 - Plasticity and Creep. In: *GT201394675 ASME Turbo Expo 2013: Turbine Technical Conference and Exposition*. American Society of Mechanical Engineers; 2013. p. V07AT27A004-V07AT27A004.
- [4] Meric L, Poubanne P, Cailletaud G. Single Crystal Modeling for Structural Calculations: Part 1 – Model Presentation. *Journal of Engineering Materials and Technology*. 1991;113(1): 162-171.
- [5] Meric L, Cailletaud G. Single Crystal Modeling for Structural Calculations: Part 2 – Finite Element Implementation. *Journal of Engineering Materials and Technology*. 1991;113(1): 171-182.
- [6] Milligan WW, Antolovich SD. Yielding and deformation behavior of the single crystal superalloy PWA 1480. *Metallurgical Transactions*. 1987;18(1): 85-95.
- [7] Allan CD. *Plasticity of Nickel-based Single Crystal Superalloy*. Ph.D. thesis. Massachusetts Institute of Technology; 1995.
- [8] Raabe D, Klose P, Engl B, Imlau KP, Friedel F, Roters F. Concepts for integrating plastic anisotropy into metal forming simulations. *Advanced Engineering Materials*. 2002;4(4): 169-180.
- [9] Leidermark D. *Crystal plasticity and crack initiation in a single-crystal nickel-base superalloy: Modelling, evaluation and applications*. Ph.D. thesis. Sweden: Linköping University; 2011.
- [10] Semenov AS, Gestov LB, Semenov SG, Grishchenko AI. Soprotivlenie deformirovaniyu i razrusheniju monokristallicheskih zharoprochnykh splavov pri staticheskom i ciklicheskom nagruzhenii. *Vestnik samarskogo gosudarstvennogo ajerokosmicheskogo universiteta imeni akademika S.P. Koroleva*. 2014;5(47): 70-79. (In Russian)
- [11] Getsov LB, Semenov AS, Besschetnov VA, Grishchenko AI, Semenov SG. Long-term strength determination for cooled blades made of monocrystalline superalloys. *Thermal Engineering*. 2017;64(4): 280-287.

- [12] Getsov LB, Semenov AS, Tikhomirova EA, Rybnikov AI. Thermocyclic and static-failure criteria for single-crystal superalloys of gas-turbine blades. *Materials and Technology*. 2014;48(2): 255-260.
- [13] Nozhnitsky YA, Doulnev RA, Soundyrin VG. Damage mechanisms for thermomechanical fatigue of aircraft engines materials. In: *Proc. AGARG Conference 569 "Thermal mechanical fatigue of aircraft engines materials"*. NATO; 1995. p.1-12.
- [14] Tsuno N, Shimabayashi S, Kakehi K, Rae CMF, Reed RC. Tension/compression asymmetry in yield and creep strengths of Ni-based superalloys. In: *Proceedings of the International Symposium on Superalloys*. TMS; 2008: p.433-442.
- [15] Vasilyev BE. Prediction of the kinetics of the 3D stress-strain state of high-temperature gas turbine blades with limited experimental data. In: *28th Congress of the International Council of the Aeronautical Sciences 2012*. ICAS; 2012. p.3.
- [16] Simo JC, Hughes TJR. *Computational inelasticity*. New York: Springer; 1998.

IDENTIFICATION OF MICRO-MECHANICAL CHARACTERISTICS OF MONOCLINIC TUNGSTEN TRIOXIDE MICROPARTICLES BY NANOINDENTATION TECHNIQUE

A.B.D. Nandiyanto^{1*}, F. Triawan², R. Firly³, A.G. Abdullah⁴, Y. Aono³,
K. Inaba⁵, K. Kishimoto⁵

¹Departemen Kimia, Universitas Pendidikan Indonesia, Jl. Dr. Setiabudi no 229, Bandung 40154, Indonesia

²Faculty of Engineering and Technology, Sampoerna University, Jl. Raya Pasar Minggu, Kav. 16, Pancoran, Jakarta, Indonesia

³Department of Mechanical Engineering, School of Engineering, Tokyo Institute of Technology, 2-12-1 Okayama, Meguro, Tokyo 152-8552, Japan

⁴Departemen Teknik Elektro, Universitas Pendidikan Indonesia, Jl. Dr. Setiabudi no 229, Bandung 40154, Indonesia

⁵Department of Transdisciplinary Science and Technology, Tokyo Institute of Technology, 2-12-1 Ookayama, Meguro-ku, Tokyo 152-8552 Japan

*e-mail: nandiyanto@upi.edu

Abstract. Tungsten trioxide (WO_3) has excellent mechanical properties, making them to be applied in various applications. However, researches on the mechanical properties of WO_3 in the micrometer scale are limited. Here, the purpose of this study was to demonstrate nanoindentation technique in an attempt to study the micro-mechanical characteristics of monoclinic WO_3 microparticles that were previously synthesized using a direct heat treatment of ammonium tungstate pentahydrate powder at a temperature of 800°C . The experiment comprises a measurement by load controlled nanoindentation test on the particle sample to obtain force and displacement relationship. The results exhibited variability on the force-displacement curves for similar applied load. This could be due to the micro-mechanical effects generated by the existence of inclusions, precipitates, and oxides inside the micron WO_3 particles. The present study demonstrates the importance of understanding the micro-mechanical characteristics of WO_3 for clarifying the inhomogeneity effects on its macro-mechanical properties.

Keywords: tungsten trioxide, micro-mechanical characteristics, nanoindentation, porous material

1. Introduction

Recently, tungsten trioxide (WO_3) has been grown for being used in a variety of engineering applications due to its excellent performance (i.e., high mechanical strength, relatively harmless, active under visible light with good photostability, chemical and thermal stable, as well as chemical and biological inertness) [1,2]. Therefore, no question argues that WO_3 is still attractive to date, and numerous of the applications rely on its behaviors[3].

Despite the quality improvement of WO_3 over the years, this challenging material still suffers from the understanding information regarding mechanical properties of WO_3 particles. Although several reports regarding the mechanical properties of WO_3 have been published [4-7], they are limited to the specific size, specifically in the bulk or nanometer size. Further, there is almost no report on the analysis of mechanical properties of WO_3 in the micrometer scale.

Reports on the mechanical properties of WO_3 in the micron scale are still interesting since mostly WO_3 are applied in this size range. In fact, this micron-scaled mechanical properties data is vital, in which this dimension may reach larger impacts when the material is restructured into bulk or even smaller scale[8]. Further, micron scale WO_3 is typically disregarded, while it has been largely used since it has possessed excellent properties in applications that are different from bulk and nanometer sizes[1,2]. Thus, understanding the mechanical properties of WO_3 in the micron scale is inevitable.

Based on our previous studies regarding the synthesis of WO_3 particles [1,2,9-15] and analysis of mechanical strength of various structures [16-19], the purpose of this study was to demonstrate a nanoindentation technique in an attempt to study the micro-mechanical characteristics of WO_3 particles. The experiment comprises a systematic measurement of load controlled nanoindentation technique to obtain force and displacement relationship. Nanoindentation, or ultra-low load indentation, is used as one of the standard techniques over the last decade. This technique has been utilized for probing the mechanical properties of materials even at very small scales [20]. One of the great benefits of the technique is the ability in determining mechanical properties only by analyzing the indentation load-displacement data alone.

2. Materials and Methods

Specimen. This study used WO_3 microparticles as a specimen, which were produced using the similar method reported in literature [1,2,13]. In short, the particles were prepared by heating 2 grams of ammonium tungstate pentahydrate (ATP; >99%; Kanto Chemical Co., Inc., Japan). The heating process was done using a commercial electrical furnace under a fixed condition (a heating rate of 50 °C/min and a holding time at 800°C for 30 min) in the atmospheric condition. To gain WO_3 with a monoclinic phase, the heating process was subsequently followed by a cooling process to room temperature (a cooling rate of 50°C/min).

In addition, in order to obtain the properties of the specimen, physical observation was performed using a Scanning Electron Microscope (SEM; SEM, JSM-6360LA; JEOL Ltd., Japan) and a Transmission Electron Microscope (TEM, JEOL JEM-1400, JEOL Ltd., Japan). Then, the resulted images were applied into Feret analysis to obtain the particle outer diameter and morphology. In order to analyze the chemical composition and the crystal structure of the specimen, a Fourier Transform Infrared Spectroscopy (FTIR; FTIR-4600, Jasco Corp., Japan) and a powder X-ray diffraction (XRD; XRD; PANalytical X'Pert PRO; Philips Corp., The Netherland) were utilized, respectively.

Nanoindentation Technique. In order to evaluate the elastic modulus and micro-hardness, the WO_3 specimen was tested by a nanoindentation test technique (TriboScope®, Hysitron, US) based on Oliver and Pharr Method[21]. The nanoindentation test equipment was completed with portable add-on equipment to scanning probe microscope (SPM, SPM-9500J3, Shimadzu Corp., Japan). It uses a capacitive force/displacement transducer that generates the loading force and measures both force and displacement data.

Before mounting the specimen to the SPM plate, the specimens were diluted into the methanol and spread out into the specimen holder. Force penetrations were located on

several arbitrary particle surfaces in order to get technically statistical data. Prior to every test, calibration is conducted using an air indent method.

In order to obtain the force and displacement relationship, the indenter was first loaded to the peak load by certain time both set up by the user and then unloaded according to the defined profile. Loading rate for all testing was kept constant at $2 \mu\text{N/s}$. Force control-type input was employed. The max load for each specimen was determined based on the preliminary tests which show the most suitable force and displacement curve. Each maximum load measurement was done at least 6 times at different locations. In addition, as a standard analysis, aluminum bulk plate was used. Using the same procedure, we also examined the mechanical properties of ATP particles.

3. Results and Discussion

Figure 1 shows the physicochemical properties of WO_3 used as the specimen in this study. The physical appearance of the specimen is a yellowish green powder (Fig. 1(a)), which is different from its originated ATP (white powder) [13]. The SEM image in Fig. 1(b) confirmed that the prepared particles were in the micrometer range with mean sizes of about $60 \mu\text{m}$. The high-magnified SEM image (Fig. 1(c)) confirmed the rough surface, indicating the aggregated of crystal structure inside the particles. To verify the aggregate structure, Fig. 1(d) presents the TEM image of the particles. The TEM image identified that the particles are relatively dense (no porous structure).

The FTIR analysis in Fig. 1(e) showed that the particles were tungsten-related materials, in which this was detected by the appearance of peaks at wavenumber of less than 1000 cm^{-1} [13]. The XRD analysis in Fig. 1(f) also verified the structure of monoclinic-type WO_3 material, based on the joint committee for the powder diffraction system (JCPDS) no. 72-1465[2].

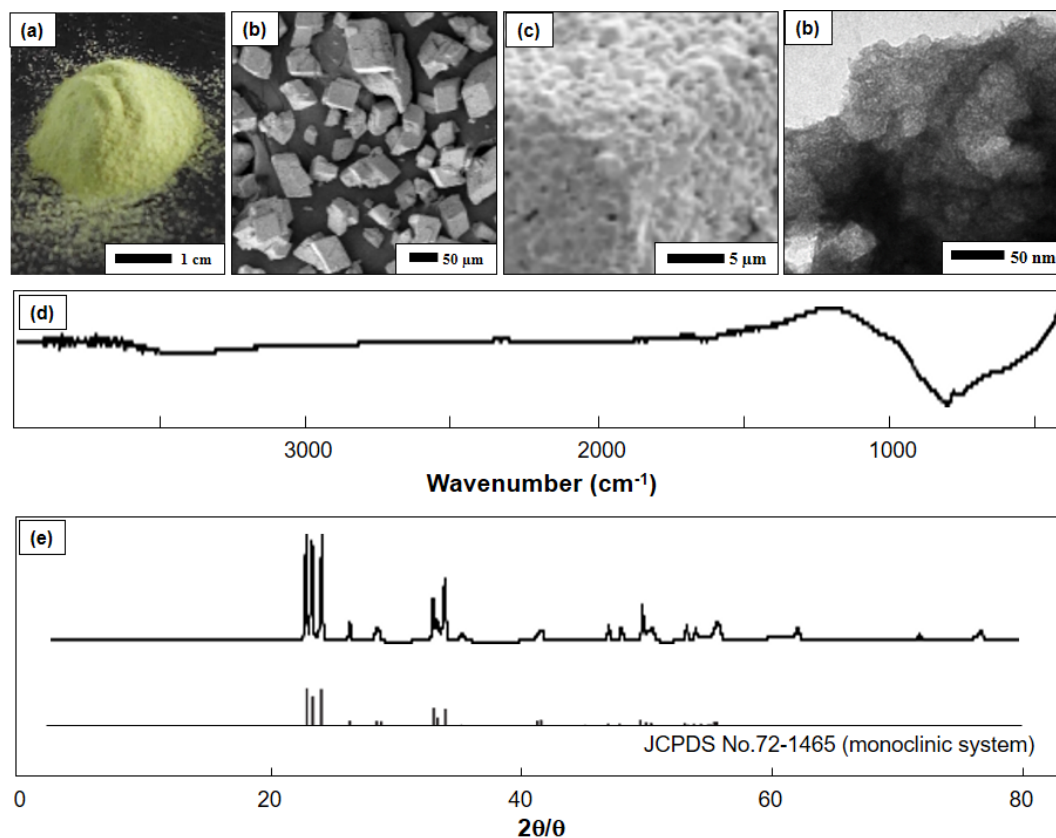


Fig. 1. (a) the photograph image, (b) the low-magnified SEM image, (c) the high-magnified SEM image, (d) the TEM image, (e) FTIR analysis, and (f) XRD results of WO_3 specimen

The typical nanoindentation test results of the WO_3 microparticles are shown in Fig. 2. As a comparison, we also analyzed the initial ATP particles. The results showed force-displacement curve for nanoindentation of WO_3 particles on 6 different locations with constant controlled maximum load (i.e., 200 μN) and loading rate. The final displacement after unloading for one and other data varies as far as more than 2000 nm. This is still less than 10% of the average particle diameter. Moreover, the loading slope of one and other curves has some discrepancies. This result implies that WO_3 particles have the inhomogeneity characteristics. This could be due to inclusions, precipitates, or oxides that present on the specimen at micro-scale (see Fig. 1(c)). However, in overall, all force-displacement curves showed similar tendency.

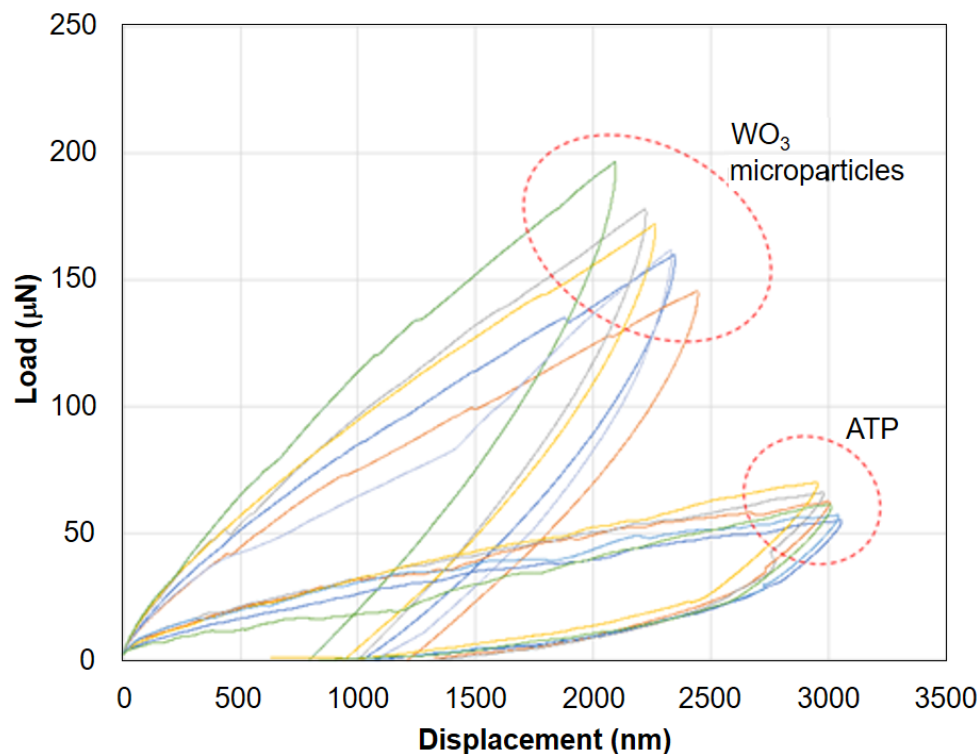


Fig. 2. Typical force-displacement curves of ATP and WO_3 microparticles obtained from nanoindentation tests

By Oliver and Pharr method[21], analysis on the elastic modulus and micro-hardness of ATP and WO_3 particles were conducted. Figure 3 shows the measurement results. Here, the measured elastic modulus is the effective value which still contains some effects from the substrate as well as the indenter (Berkovich indenter). Because in this study the same substrate and indenter were used for every test, therefore, the measured value can be compared to evaluate the mechanical properties' tendency. However, if the true value is required, we need to extract the effect of substrate and indenter from the measured value.

Based on the measurement results, it is obvious that WO_3 particles (produced after heating ATP at 800°C) shows a significant increase in the values of elastic modulus and micro-hardness by 10 and 40 times, respectively. This indicates the measurement was able to show the different mechanical properties from each specimen. As a validation, the same test was also done on Aluminum bulk specimen with maximum load of 1000 μN . The result demonstrated good accuracy for analyzing the values of elastic modulus and micro-hardness of WO_3 materials as also reported in the literatures [6].

The above mechanical properties data revealed that the micrometer-sized WO_3 particles have excellent mechanical properties. The mechanical properties in elastic modulus

and micro hardness increased compared to the initial ATP raw material. We believe that this data can inform that the use of micrometer-sized WO_3 particles is potentially used for various processes involving extreme conditions such as high pressure reaction.

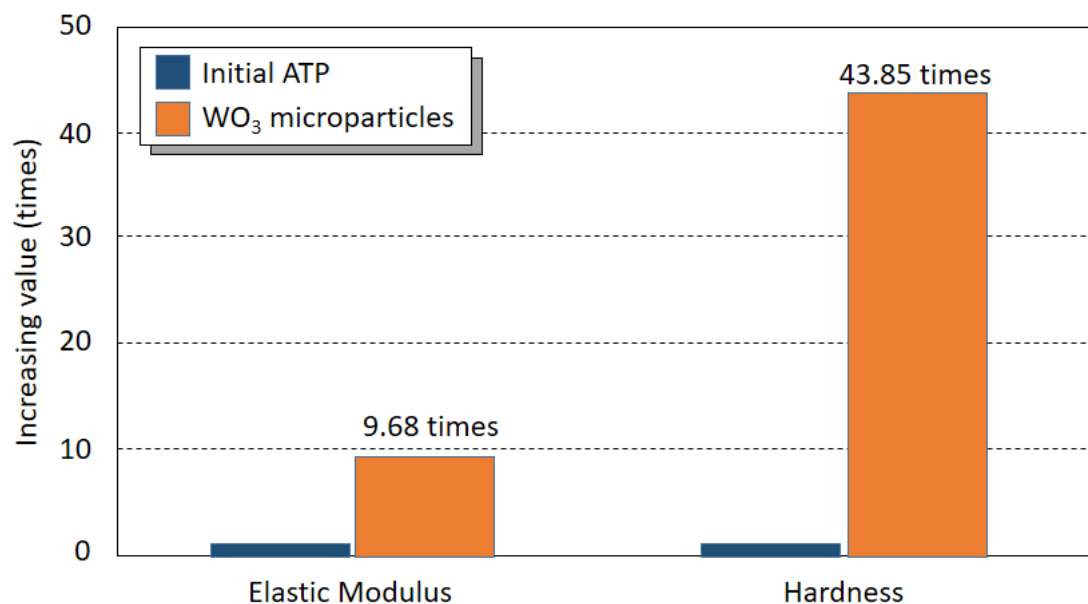


Fig. 3. Increases in Elastic Modulus and Hardness values of ATP and WO_3 microparticles

4. Conclusion

Micromechanical characteristics of WO_3 micron particles have been investigated using a nanoindentation test technique from which the elastic modulus and micro-hardness values were evaluated and compared with ATP particles. Although in overall the measured force-displacement curve showed similar tendency, we found an important phenomenon that revealed the inhomogeneity characteristics of WO_3 particles as indicated by the variety of force-displacement curve. This could be caused by the micro-scale characteristics of the specimen due to the existence of inclusions, precipitates, and oxidizes generated during the synthesis of WO_3 . The results also confirmed that the elastic modulus and hardness values of WO_3 are in a good agreement with literature, demonstrating that the present results gives additional information for further studies in mechanical properties of WO_3 material. Furthermore, it was also revealed that the WO_3 micron particles have significantly higher values of elastic modulus and hardness compared with that of ATP particles.

Acknowledgements. A.B.D.N. acknowledged RISTEK DIKTI for grant-in-aid Penelitian Terapan Unggulan Perguruan Tinggi (PTUPT), Penelitian Terapan (PT), and World Class Research (WCR).

References

- [1] Nandiyanto ABD, Oktiani R, Ragadhita R, Sukmafritri A, Zaen R. Amorphous content on the photocatalytic performance of micrometer-sized tungsten trioxide particles. To be published in *Arabian Journal of Chemistry*. 2018. Available from: doi.org/10.1016/j.arabjc.2018.07.021.
- [2] Nandiyanto ABD, Zaen R, Oktiani R. Correlation between crystallite size and photocatalytic performance of micrometer-sized monoclinic WO_3 particles. To be published in *Arabian Journal of Chemistry*. Available from: doi.org/10.1016/j.arabjc.2017.10.010.

- [3] Triawan F, Adachi T, Kishimoto K, Hashimura T. Study on elastic moduli of aluminum alloy foam under uniaxial loading and flexural vibration. *Journal of Solid Mechanics and Materials Engineering*. 2010;4(8): 1369-1380.
- [4] Parreira N, Carvalho N, Cavaleiro A. Synthesis, structural and mechanical characterization of sputtered tungsten oxide coatings. *Thin Solid Films*. 2006;510(1-2): 191-196.
- [5] Ahangarkani M, Zangeneh-Madar K, Borji S. Microstructure evolution and formation of needle-like WO_3 nanowire during sintering of submicron tungsten particles. *International Journal of Refractory Metals and Hard Materials*. 2018;70: 93-100.
- [6] Maillé L, Sant C, Aubert P, Garnier P. Morphological and mechanical properties study of $[\text{WO}_3/\text{W}]_n$ nanoscale multilayers. *Thin Solid Films*. 2005;479(1-2): 201-206.
- [7] Hasan M, Haseeb A, Masjuki H. Structural and mechanical properties of nanostructured tungsten oxide thin films. *Surface Engineering*. 2012;28(10): 778-785.
- [8] Triawan F, Kishimoto K, Adachi T, Inaba K, Nakamura T, Hashimura T. The elastic behavior of aluminum alloy foam under uniaxial loading and bending conditions. *Acta Materialia*. 2012;60(6-7): 3084-3093.
- [9] Nandiyanto ABD, Arutanti O, Ogi T, Iskandar F, Kim TO, Okuyama K. Synthesis of spherical macroporous WO_3 particles and their high photocatalytic performance. *Chemical Engineering Science*. 2013;101: 523-532.
- [10] Arutanti O, Ogi T, Nandiyanto ABD, Iskandar F, Okuyama K. Controllable crystallite and particle sizes of WO_3 particles prepared by a spray-pyrolysis method and their photocatalytic activity. *AIChE Journal*. 2014;60(1): 41-49.
- [11] Arutanti O, Nandiyanto ABD, Ogi T, Iskandar F, Kim TO, Okuyama K. Synthesis of composite WO_3/TiO_2 nanoparticles by flame-assisted spray pyrolysis and their photocatalytic activity. *Journal of Alloys and Compounds*. 2014;591: 121-126.
- [12] Arutanti O, Nandiyanto ABD, Ogi T, Kim TO, Okuyama K. Influences of porous structurization and Pt addition on the improvement of photocatalytic performance of WO_3 particles. *ACS Applied Materials and Interfaces*. 2015;7(5): 3009-3017.
- [13] Nandiyanto ABD, Munawaroh HSH, Kurniawan T, Mudzakir A. Influences of temperature on the conversion of ammonium tungstate pentahydrate to tungsten oxide particles with controllable sizes, crystallinities, and physical properties. *Indonesian Journal of Chemistry*. 2016;16(2): 124-129.
- [14] Nandiyanto ABD, Okuyama K. Influences of size and amount of colloidal template and droplet diameter on the formation of porous-structured hyaluronic acid particles. *Indonesian Journal of Science and Technology*. 2017;2(2): 152-165.
- [15] Munawaroh H, Nandiyanto A, Gumilar G, Widi A, Subangkit M. Effect of oral administration of tungsten trioxide (WO_3) particles on hispathological feature of liver and kidney in rat. *IOP Conference Series: Materials Science and Engineering*. 2017;180(1): 012097.
- [16] Budiman BA, Triawan F, Adziman F, Nurprasetio IP. Modeling of stress transfer behavior in fiber-matrix composite under axial and transverse loadings. *Composite Interfaces*. 2017;24(7): 677-690.
- [17] Nurprasetio IP, Budiman BA, Triawan F. Failure investigation of plastic shredding machine's flange coupling based on mechanical analysis. *Indonesian Journal of Science and Technology*. 2017;2(2): 124-133.
- [18] Inoue K, Triawan F, Inaba K, Kishimoto K, Nishi M, Sekiya M, Sekido K, Saitoh A. Evaluation of interfacial strength of multilayer thin films polymer by nanoindentation technique. *Mechanical Engineering Journal*. 2019;6(1): 18-00326.

- [19] Triawan F, Nandiyanto ABD, Abdullah AG, Aziz M. Plasma nitriding time on the hardness and crystal structure/phase of SUS403 and SCS6 martensitic stainless steels: an analytical study. *Journal of Engineering Science and Technology*. 2018;13(8): 2369-2378.
- [20] Pharr G. Measurement of mechanical properties by ultra-low load indentation. *Materials Science and Engineering A*. 1998;253(1-2): 151-159.
- [21] Oliver WC, Pharr GM. Measurement of hardness and elastic modulus by instrumented indentation: Advances in understanding and refinements to methodology. *Journal of Materials Research*. 2004;19(1): 3-20.

SUPERCOMPUTING ANALYSIS OF FAN-SHAPED WAVES IN THE EARTH'S CRUST AT THE DEPTH OF SEISMIC ACTIVITY

V.M. Sadovskii*, O.V. Sadovskaya

Institute of Computational Modeling SB RAS, Akademgorodok 50/44, Krasnoyarsk, Russia

*e-mail: sadov@icm.krasn.ru

Abstract. The high-speed process of tectonic faults formation in zones of seismic activity of the Earth's crust is analyzed in a plane strain state based on the model of elastic blocks interacting through a domino-structure under conditions of strong hydrostatic compression. Numerical simulation of the dynamics of emerging fan-shaped waves is performed by means of the developed computational algorithm and computer program for multiprocessor supercomputers of cluster architecture.

Keywords: shear rupture, extremely high speed, Tarasov's fan-shaped mechanism, edge dislocation, dynamics, elasticity, high-performance computations

1. Introduction

Along with slowly growing cracks, in hard rocks at great depths shear ruptures are observed, which grow with an abnormally high speed, comparable to or even exceeding the velocity of transverse waves. This phenomenon is widely discussed in contemporary seismology and is the subject of a number of theoretical and experimental studies [1-5]. To explain a high-speed motion of shear ruptures, Professor B.G. Tarasov from the University of Western Australia proposed an original mechanism [6]. According to his ideas, at the rupture tip a fan-shaped structure, consisting of domino-slabs, is formed. These slabs rotate when relatively low tangential stresses appear in the surrounding rock mass and, what is most important, preserve their integrity during rotation. Schematically, the process of formation and propagation of a fan-structure is shown in Fig. 1. The slabs exfoliate from the hard rock because of the high confining pressure, tending to change the direction of propagation of the main crack. At the same time, an abnormally low friction is created at the rupture head due to the weak resistance to separation of the domino-slabs, continuously supplementing the fan-shaped system, and the fan moves like a wave extremely fast.

To illustrate the fan-shaped mechanism, Tarasov created a laboratory model simulating the motion of a fan in a system of elastically bonded slabs on a flat surface [6]. Corresponding mathematical model was developed, the analysis of which with using numerical and analytical methods makes possible to describe main qualitative features of the phenomenon under consideration [7,8]. On the basis of the mathematical model, the dependence of fan speed on the resistance of separation was studied, the influence of viscous and dry friction was analyzed, the multiplicative power interaction of the slabs in a fan-shaped system was shown, which contribute to the fast motion of the fan.

The static problem of the equilibrium of two infinite elastic blocks interacting through a thin interlayer (a fan-structure) in the plane formulation was studied in [9]. As a result, the fields of stresses and displacements were obtained in the blocks in the vicinity of a formed fan, which play the role of initial data under solution of dynamic problem.

http://dx.doi.org/10.18720/MPM.4232019_8

© 2019, Peter the Great St. Petersburg Polytechnic University

© 2019, Institute of Problems of Mechanical Engineering RAS

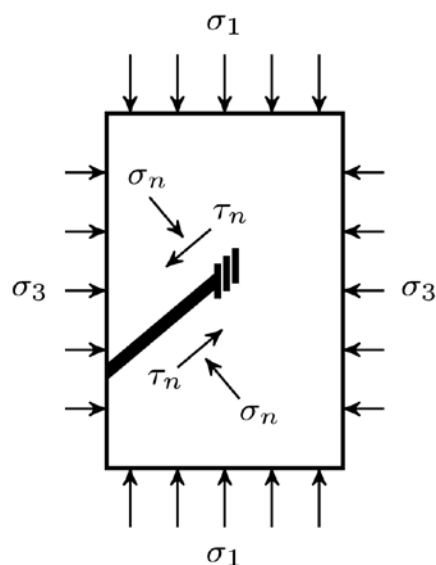


Fig. 1. The scheme of formation of a fan domino-structure

In the present paper, the process of starting and subsequent motion of a fan-shaped system between two elastic blocks is analyzed on the basis of dynamic equations of a plane strain state by use of supercomputers of cluster architecture.

2. Mathematical model

Analysis of the static solution shows that a fan-structure, formed under the action of natural or technogenic processes, with the slabs height of 0.1 m significantly changes the hydrostatic stress state in the surrounding rock. These changes extend over a distance of the order of the fan's length, which is tens of meters, in the direction of the rupture and over a distance of 5 – 10 m in the normal direction. For direct numerical simulation of the dynamic processes taking place, the dimensions of each of two interacting blocks must be at least 5 m · 50 m, and the step of squared difference grid must be approximately 0.01 m, which is ten times smaller than the height of slabs. Thus, we obtain a computationally complex problem that requires resources of RAM and runtime that are characteristic for a supercomputer of average performance of a cluster or hybrid architecture. For solution of this problem, the technology of parallelization on the basis of decomposition of computational domain is applied. Blocks interacting through a fan are uniformly distributed between the cluster nodes, and necessary data exchange over the boundaries takes place. We use previously developed author's program code [10] for the analysis of dynamic processes in a multi-blocky medium with thin interlayers.

Equations of a blocky medium. The plane strain state of blocks (rectangles with sides parallel to the axes of a Cartesian coordinate system) is described by the system of equations of a homogeneous isotropic elastic medium:

$$\rho \dot{v}_1 = \sigma_{11,1} + \sigma_{12,2}, \quad \rho \dot{v}_2 = \sigma_{12,1} + \sigma_{22,2}, \quad \dot{\sigma}_{12} = \rho c_2^2 (v_{2,1} + v_{1,2}), \tag{1}$$

$$\dot{\sigma}_{11} = \rho c_1^2 (v_{1,1} + v_{2,2}) - 2\rho c_2^2 v_{2,2}, \quad \dot{\sigma}_{22} = \rho c_1^2 (v_{1,1} + v_{2,2}) - 2\rho c_2^2 v_{1,1}.$$

Here ρ is the density, c_1 and c_2 are the velocities of longitudinal and transverse elastic waves, respectively. The dot over a symbol denotes partial derivative with respect to time and the indices after a comma denote partial derivatives with respect to spatial variables. The conventional notations of tensor analysis are used. Internal boundary conditions at the

interblock artificial boundaries between computational nodes are the conditions of continuity of the velocity vector v and the stress vector \vec{l} on respective areas.

For obtaining numerical solution of the system (1) with given initial data and boundary conditions, a parallel computational algorithm was developed, in which a two-cyclic splitting method with respect to spatial variables is realized [11]. Systems of 1D equations in blocks are solved on the basis of implicit finite-difference scheme constructed in [12]. The algorithm proposed in this paper makes it possible to perform computations with large time steps, exceeding the maximum permissible value of the step according to the Courant–Friedrichs–Lewy condition for explicit schemes by many times. It can be applied both in the simplest case of the contact interaction between blocks of the type of continuity condition, and in the case of nonlinear internal boundary conditions of a sufficiently general form.

Modeling of a fan. When modeling the dynamics of a fan-shaped system, one of the horizontal interlayers in a blocky massif is assumed to be a tectonic fault – an extended rectilinear zone of small thickness with a fan-structure. A separate fragment of such structure, in accordance with the Tarasov model, can be considered as an absolutely rigid slab with the height a of a unit cross section. Position of the slab relative to horizontal axis at the initial time moment is given by the angle φ_0 . Formation and further propagation of the fan is accompanied by rotation of the slab with a change of angle from φ_0 to $\varphi_1 = \pi - \varphi_0$.

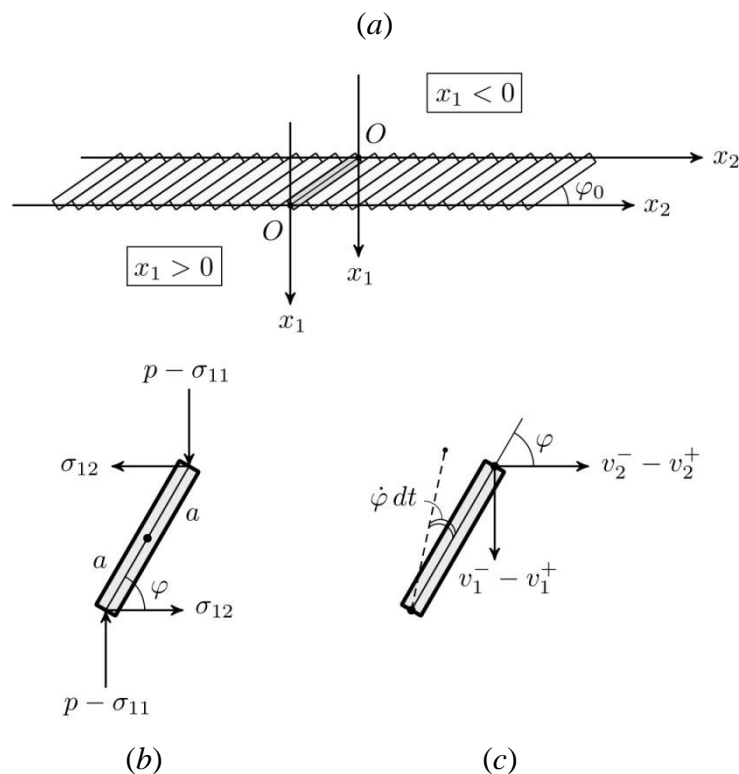


Fig. 2. Coordinate systems in the blocks (a), scheme of loading for a slab (b), and kinematic scheme (c)

Under formulation of boundary conditions in the fan zone, the coordinate systems in blocks, shown in Fig. 2 a, are identified. The loading scheme for the slab oriented at the angle φ ($\varphi_0 \leq \varphi \leq \varphi_1$) is represented in Fig. 2 b. It includes the normal and tangential stresses acting from the side of upper and lower adjacent blocks, and the rotational moment due to the contact interaction with neighboring slabs. Under the assumption of the smallness of inertial forces and moments, the equilibrium conditions are valid:

$$\sigma_{11}^+ = \sigma_{11}^- \equiv \sigma_{11}, \quad \sigma_{12}^+ = \sigma_{12}^- \equiv \sigma_{12}, \quad M + \sigma_{11} a \cos \varphi + \sigma_{12} a \sin \varphi = 0, \quad (2)$$

where superscripts " \pm " are related to the boundaries of interacting blocks. In accordance with the kinematic scheme in Fig. 2 c, the following equations are satisfied:

$$v_1^+ - v_1^- = a \dot{\varphi} \cos \varphi, \quad v_2^+ - v_2^- = a \dot{\varphi} \sin \varphi. \quad (3)$$

Contact interaction of fragments is described by the variational inequality:

$$(M + \eta \dot{\varphi})(\tilde{\varphi} - \varphi) \geq 0, \quad \varphi_0 \leq \tilde{\varphi} \leq \varphi_1. \quad (4)$$

Here $\tilde{\varphi}$ is an arbitrary admissible variation of the angle, η is the coefficient of viscous friction. If $\varphi = \varphi_0$, then from the variational inequality it follows that the moment M is nonnegative, and if $\varphi = \varphi_1$, then it is nonpositive. If $\varphi_0 < \varphi < \varphi_1$, then, because of the arbitrariness of variation, it follows from (4) that M is equal to the moment of viscous friction forces. This corresponds exactly to the loading scheme.

The algorithm of numerical realization of the conditions for interaction of blocks through a fan interlayer, based on the relationships (2) – (4), was implemented by means of the equations for predictor step obtained in [12]. These equations are approximations of the equations on characteristics for 1D systems in adjacent cells of the neighboring blocks. According to them

$$z_1^+ v_1^+ + \sigma_{11}^+ = P^+, \quad z_2^+ v_2^+ + \sigma_{12}^+ = S^+, \quad z_1^- v_1^- - \sigma_{11}^- = P^-, \quad z_2^- v_2^- - \sigma_{12}^- = S^-, \quad (5)$$

where z_1^\pm and z_2^\pm are the difference analogues for the acoustic impedances of longitudinal and transverse waves, P^\pm and S^\pm are the analogues of Riemann invariants corresponding to these waves.

After simple transformations, the inequality (4) takes the following form:

$$((A + \eta) \dot{\varphi} - B)(\tilde{\varphi} - \varphi) \geq 0, \quad \varphi_0 \leq \tilde{\varphi} \leq \varphi_1,$$

$$A = z_1 a^2 \cos^2 \varphi + z_2 a^2 \sin^2 \varphi, \quad B = (P^+ - P^-) a \cos \varphi + (S^+ - S^-) a \sin \varphi, \quad 1/z_k = 1/z_k^+ + 1/z_k^-.$$

Approximation of the derivative by time leads to the discrete variational inequality:

$$(\hat{\varphi} - \bar{\varphi})(\tilde{\varphi} - \hat{\varphi}) \geq 0, \quad \bar{\varphi} = \varphi + \Delta t B / (A + \eta),$$

the solution of which $\hat{\varphi}$ ($\varphi_0 \leq \hat{\varphi} \leq \varphi_1$), related to a new time layer, is defined as the projection $\bar{\varphi}$ onto constraints: $\hat{\varphi} = \varphi_0$ if $\bar{\varphi} < \varphi_0$, or $\hat{\varphi} = \bar{\varphi}$ if $\varphi_0 \leq \bar{\varphi} \leq \varphi_1$, or $\hat{\varphi} = \varphi_1$ if $\varphi_1 < \bar{\varphi}$. Further, the angular velocity is calculated by the formula $\dot{\varphi} = (\hat{\varphi} - \varphi) / \Delta t$, and using equations (2), (3), (5) the velocities and stresses at the interlayer boundaries are found. These values are necessary for the subsequent realization of the algorithm for calculating velocities and stresses in adjacent blocks.

3. Results of computations

By means of the described algorithm the computations of fan-shaped waves in an interlayer between two homogeneous blocks of hard rock were performed. It was assumed that at the initial time moment these blocks are in equilibrium under the action of confining pressure $\sigma_{11} = \sigma_{22} = -p$ and static stresses, which are formed around the fan. Motion occurs due to the additional tangential stress $\sigma_{12} = \tau$, increasing monotonically with time or being applied abruptly.

In the initial state the fan was set near the left boundary. To trace its motion over a long distance, the length of both blocks was taken as 80 m, and the step of a grid – as 0.01 m. Computations were performed on 80 nodes of the MVS–1000 supercomputer of the Institute of Computational Modeling SB RAS. The size of computational domain for each node of a cluster was 10 m \times 1 m. The acting pressure $p = 250$ MPa and the maximum value of tangential stress $\tau = 100$ MPa were chosen based on the model representations about

geological processes occurring at the depth about 10 km [6]. Elasticity parameters of the blocks: $\rho = 2700 \text{ kg/m}^3$, $c_1 = 6000$ and $c_2 = 3300 \text{ m/s}$.

Starting of a fan-shaped system. The motion of a fan system is counteracted by frictional forces and, first of all, by the force of resistance to separation of slabs in the head of the fan. Therefore, the fan starts not immediately, but only when a certain limit of tangential stress τ_* is reached in the blocks. In order to characterize the dependence of a limit stress on friction forces, the computations of the problem, in which all domino-slabs are forcibly held in a fixed state, were made. Calculated velocities in this case must be zero, and the stress fields should not depend on time. The obtained results fully satisfy this criterion. Figure 3 a shows the level surfaces of tangential stress around the forcibly held fan, which are consistent with the results of [9].

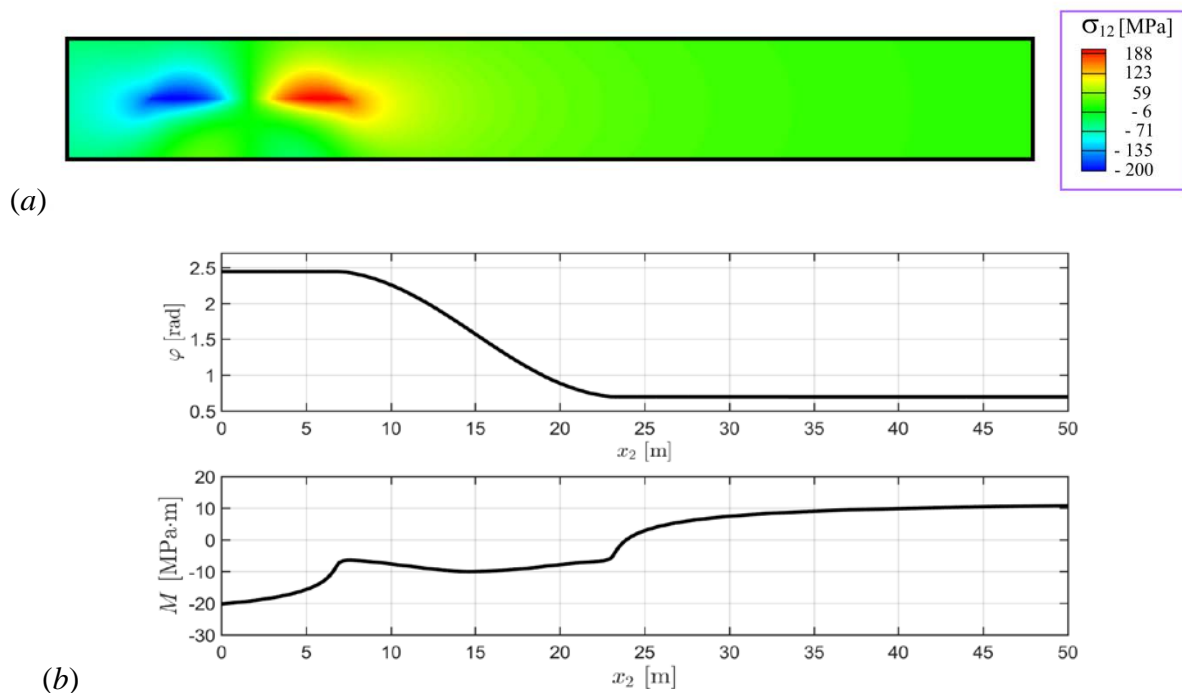


Fig. 3. Fixed fan: Level curves of tangential stress (a), distribution of the angle of rotation of slabs and distribution of the moment of restraining forces (b)

In Fig. 3 b the distributions of the angle of rotation of slabs along the fan-system and the moment of restraining forces are represented. An approximate computation of the integral

$$A = \frac{1}{2} \int_0^l M(x_2) d\varphi(x_2),$$

where l is the length of blocks, by the formula of rectangles allows to estimate the specific work of restraining forces, when a fan moves per unit distance. If $\tau_* = 100 \text{ MPa}$, then $A = 7.66 \text{ MJ/m}^2$. Because of the linearity of the problem with a fixed fan, the restraining forces are linearly dependent on the value of τ_* . Therefore, the work corresponding to other values of the limit stress can be obtained by simple recalculation.

Figure 4 shows similar results for another variant of the problem, in which only the most right slab in the head of the fan is held. In this case a dynamic process develops, the fan contracts, trying to tear off the fixed slab, which leads to a steady-state redistribution of stresses in the blocks after some time.

Fan wave motion. When modeling a moving fan, viscous friction with a coefficient $\eta = 1 \text{ MPa}\cdot\text{m}\cdot\text{s}$, stabilizing computational results, and resistance to separation of the head slab, equivalent to the moment of separation $M_* = 0.75 \text{ MPa}\cdot\text{m}$, are introduced into the model. The value of moment is lower than the limit value, which can be determined from the graph in Fig. 4 b, therefore, the fan starts and moves.

In the considered variant of the problem, the tangential stress increases monotonically with time according to the equation $\tau = \tau_* \sin^2 \pi t / t_0$ within the loading time t_0 , and after the end of this time the stress becomes constant. Boundary conditions of the problem are set in terms of the velocities for the state of simple shear, corresponding to the tangential stress reached at the given time moment.

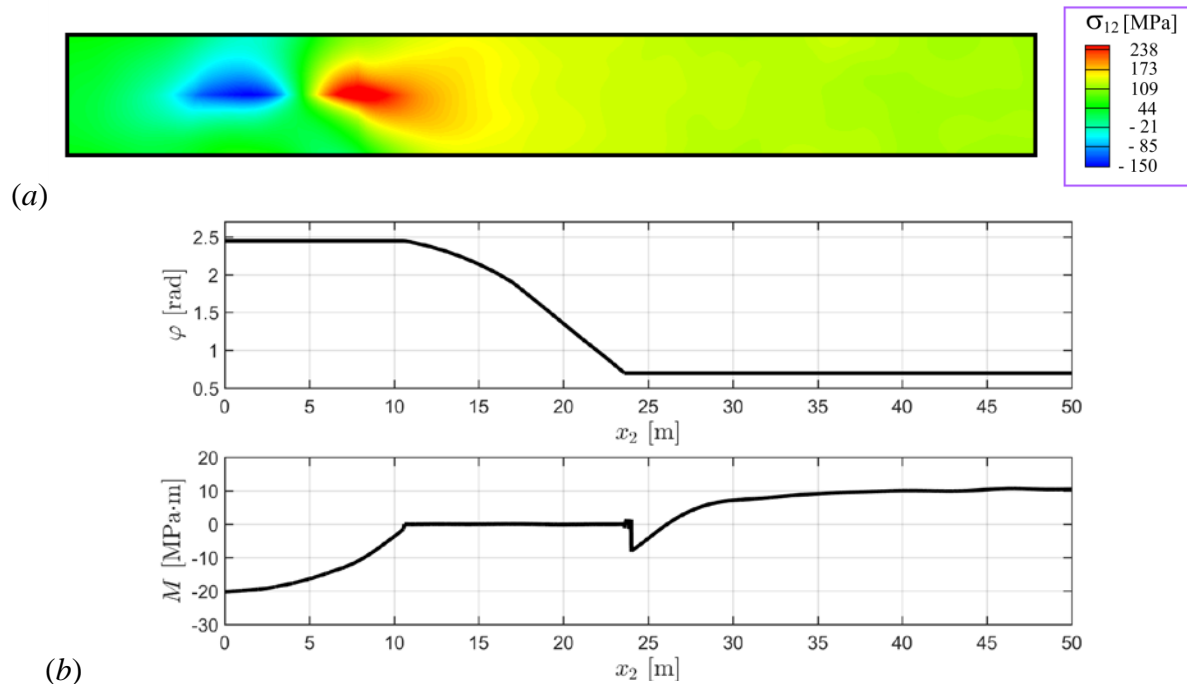


Fig. 4. Stopped fan: Level curves of tangential stress (a), distribution of the angle of rotation of slabs and distribution of the moment of restraining forces (b)

Figure 5 shows the diagrams of the angle of rotation of slabs in a fan-system successively through 0.02 s after the start, and the diagrams of the rotational moment for the loading time 0.1 s. From this figure, it can be seen that the motion of the fan is essentially nonuniform.

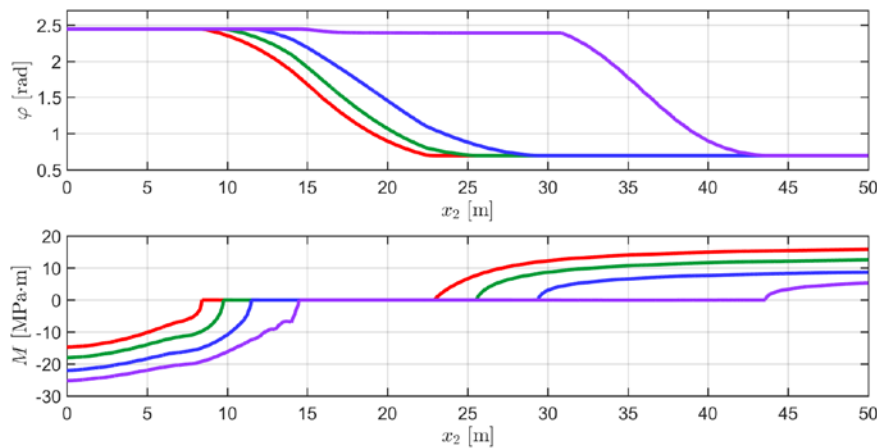


Fig. 5. Distribution of the angle of rotation of slabs and distribution of the rotational moment in a moving fan-system

Level surfaces of tangential stress for the moving fan at different time moments are represented in Fig. 6.

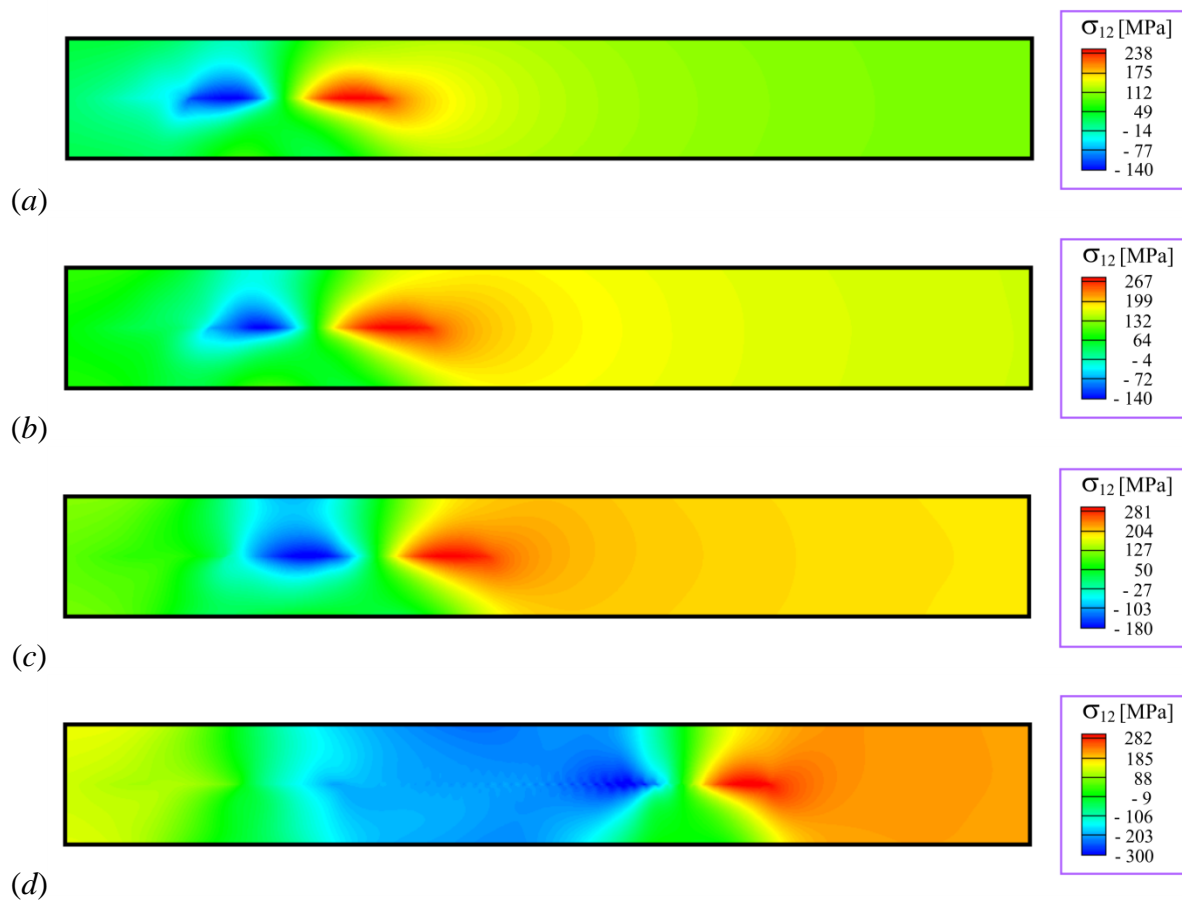


Fig. 6. Level curves of tangential stress in the process of fan motion

As computations have shown, the fan speed depends weakly on the loading time. The maximum speed is 2770 m/s at $t_0 = 0.1$ s and the maximum speed is 2890 m/s at $t_0 = 0.05$ s, both below the velocity of transverse elastic waves. For three values of the loading time $t_0 = 0.05, 0.075$ and 0.1 s the dependences of the fan speed on time are represented in Fig. 7 a. In Fig. 7 b similar dependences are given for three values of the additional tangential stress $\tau = 100, 150$ and 200 MPa. Analysis shows that the speed of a fan depends essentially on the value of tangential stress, and that at $\tau = 200$ MPa it exceeds the velocity of transverse waves, which level corresponds to the dashed line.

Note that the decrease in the fan speed after reaching the maximum value is due to the specifics of the boundary conditions on the right-hand border of the solution domain. In all variants of computations, the velocities of particles of a medium at this border after the time of loading are assumed to be zero, which leads to the effect of locking of the fan. It stops and moves in the opposite direction until the moment of a similar reflection from the left-hand border. The question of how to formulate the conditions for an unhindered passing of a fan across the border of computational domain remains open.

Computations were carried out with a variable step of the finite-difference scheme by time variable. At the beginning, the time step parameter was greater than the characteristic value of Courant–Friedrichs–Lewy $\Delta t = \Delta x/c_1$ by 25 times. With time, it was decreased, practically, to this characteristic value, in order to avoid the appearance of unphysical effects in the fan structure.

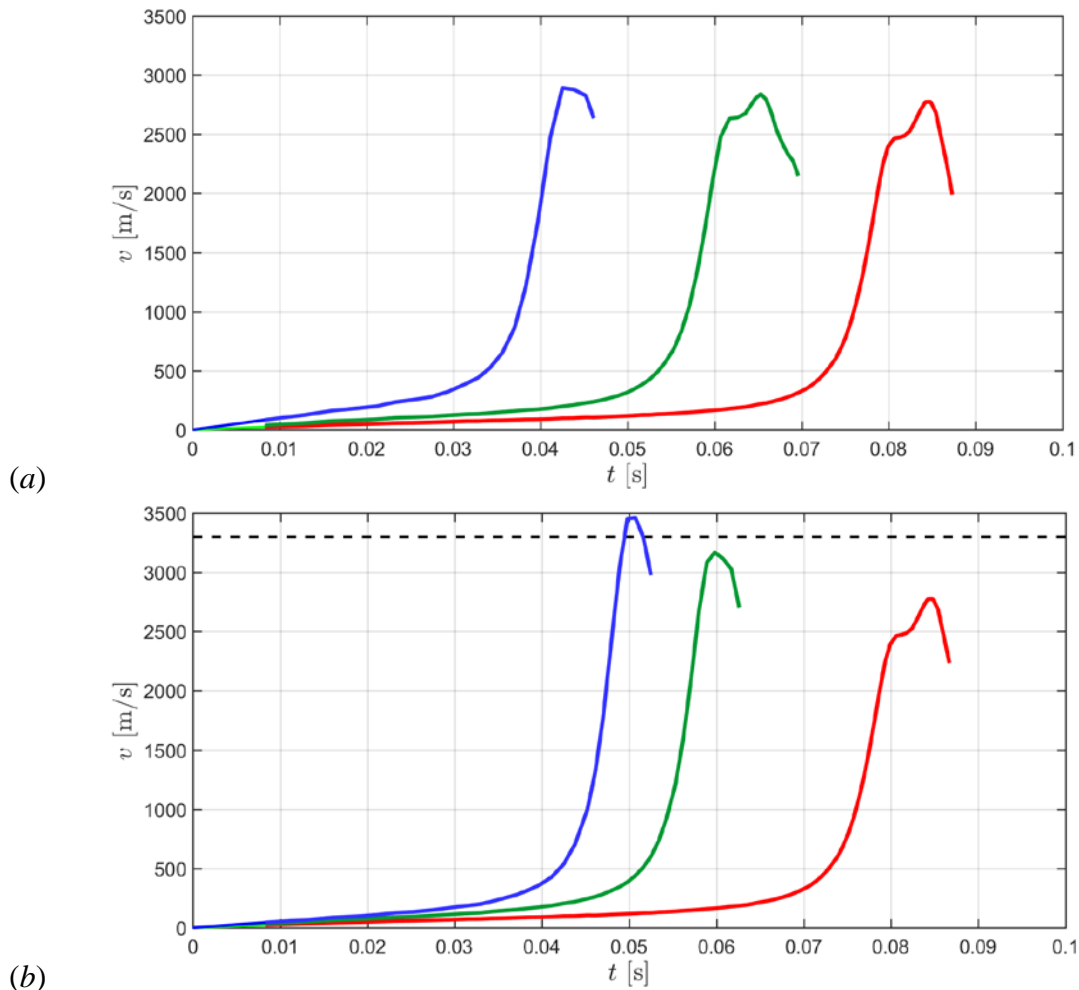


Fig. 7. Dependence of the fan velocity on the loading time (a) and on the additional tangential stress (b)

Average speed of the fan system at a given time was calculated by the estimated formula:

$$V = \frac{1}{\varphi_1 - \varphi_0} \int_0^l \dot{\varphi}(x_2) dx_2, \tag{6}$$

which follows from the equation of a traveling wave: $\varphi = \varphi(x_2 - Vt)$. Simple transformations of this equation give:

$$\dot{\varphi} = -V\varphi, \quad \dot{\varphi} dx_2 = -V d\varphi, \quad \int_0^l \dot{\varphi} dx_2 = -V \int_{\varphi_1}^{\varphi_0} d\varphi = V(\varphi_1 - \varphi_0).$$

Formula (6) takes into account that the angular velocity of domino-slabs is equal to zero outside the zone of the fan.

The range of loading times, investigated during the computations, corresponds to the passage through the fan system of low-frequency transverse waves with a frequency of 10 – 20 Hz and a wavelength in the range of 150 – 300 m. To study a more interesting case of quasistatic loading with extremely long waves of the order of several kilometers, a much more extensive domain of solution of the problem must be considered. This is possible only using a more powerful supercomputer with 1000 or more computational nodes. Current computations were fulfilled on the cluster MVS–1000 of average performance of the Institute

of Computational Modeling SB RAS and on a small cluster of the Siberian Federal University having about a hundred computational nodes.

4. Conclusions

A computational technology is developed including the mathematical model, numerical algorithm and computer program for multiprocessor supercomputers, which allows further study of the Tarasov's fan-shaped mechanism, describing the high-speed process of tectonic fracture propagation in zones of seismic activity of the Earth's crust. Based on this technology, numerical experiments simulating the fan motion excited by elastic shear waves of low frequency, of the order of tens Hertz, in the surrounding rock were performed. Obtained results characterize the fan-system as an exceptionally mobile physically unstable structure. It was shown that in the case of intensive loading the fan speed can exceed the velocity of elastic transverse waves. To analyze the motion of a fan over long distances, of the order of a kilometer, under the action of a static system of tangential stresses, it is necessary to go over to the stationary model of a running fan. Using the considered here dynamic model to solve such problem with the time of loading of the order of hours or even minutes, would require extremely large computational resources, which currently have only the world's largest supercomputer centers.

Acknowledgements. *This research was supported by the Centre for Offshore Foundation Systems of the University of Western Australia.*

References

- [1] Burridge R. Admissible speeds for plane-strain self-similar shear cracks with friction but lacking cohesion. *Geophysical Journal International*. 1973;35(4): 439-455.
- [2] Andrews DJ. Rupture velocity of plane strain shear cracks. *Journal of Geophysical Research: Solid Earth*. 1976;81(32): 5679-5687.
- [3] Freund LB. The mechanics of dynamic shear crack propagation. *Journal of Geophysical Research: Solid Earth*. 1979;84(B5): 2199-2209.
- [4] Dunham EM. Conditions governing the occurrence of supershear ruptures under slip-weakening friction. *Journal of Geophysical Research: Solid Earth*. 2007;112(87): B07302.
- [5] Lu X, Lapusta N, Rosakis AJ. Analysis of supershear transition regimes in rupture experiments: The effect of nucleation conditions and friction parameters. *Geophysical Journal International*. 2009;177(2): 717-732.
- [6] Tarasov BG. Hitherto unknown shear rupture mechanism as a source of instability in intact hard rocks at highly confined compression. *Tectonophysics*. 2014;621: 69-84.
- [7] Tarasov BG, Guzev MA, Sadovskii VM, Cassidy MJ. Modelling the mechanical structure of extreme shear ruptures with friction approaching zero generated in brittle materials. *International Journal of Fracture*. 2017;207(1): 87-97.
- [8] Tarasov BG, Sadovskii VM, Sadovskaya OV. Analysis of fan waves in a laboratory model simulating the propagation of shear ruptures in rocks. *Journal of Applied Mechanics and Technical Physics*. 2017;58(7): 1139-1152.
- [9] Tarasov BG, Sadovskii VM, Sadovskaya OV, Cassidy MJ, Randolph MF. Modelling the static stress-strain state around the fan-structure in the shear rupture head. *Applied Mathematical Modelling*. 2018;57: 268-279.
- [10] Sadovskii VM, Sadovskaya OV, Chentsov EP. *Parallel program system for numerical modeling of dynamic processes in multi-blocky media on cluster systems (2Dyn_Blocks_MPI)*. RU2016615178 (Certificate of state registration of computer program), 2016.

- [11] Sadovskaya O, Sadovskii V. *Mathematical Modeling in Mechanics of Granular Materials*. Heidelberg: Springer; 2012.
- [12] Sadovskii VM, Sadovskaya OV. Numerical algorithm based on implicit finite-difference schemes for analysis of dynamic processes in blocky media. *Russian Journal of Numerical Analysis and Mathematical Modelling*. 2018;33(2): 111-121.

FINITE ELEMENT MODELING AND INVESTIGATION OF ELASTIC HOMOGENEOUS AND HETEROGENEOUS MATERIALS

V.L. Leontiev^{1*}, I.V. Efremkov²

¹Peter the Great St. Petersburg Polytechnic University (SPbPU),
Polytechnicheskaya st., 29, Saint Petersburg 195251, Russia

²Ulyanovsk State University, L. Tolstoy st., 42. Ulyanovsk, 432000, Russia

*e-mail: leontiev_vl@spbstu.ru

Abstract. A novel finite element (FE) connected with orthogonal finite functions (OFF) was developed for ANSYS software and was tested. The FE is proposed for modeling and investigation of stress-strain states of homogeneous and heterogeneous elastic materials. The efficiency of the developed FE is demonstrated using the examples of plane problems of elasticity. The accuracy of this FE was found to be higher than that of the classical FE of ANSYS. Moreover, the developed FE was proved to require less computational time, and this difference in computational time increases with the increasing number of FE in the model.

Keywords: homogeneous and heterogeneous materials, finite element methods, orthogonal finite functions, shape functions

1. Introduction

Finite element simulations and investigations of stress-strain states of technical constructions often require very fine meshes. Even when supercomputers are used, the advantages of numerical methods are usually taken into account because in that case methods with high accuracy and low computational time allow investigation of constructions' stress-strain states without almost any geometrical simplifications. Therefore, the development of advanced discrete models and numerical methods can be referred to as an actual direction in computational mechanics.

It is impossible [1] to create basis OFFs by the classical procedure of orthogonalization of the splines. The first OFFs, Daubechies's compactly supported orthonormal wavelets [2], do not have an analytical form, and their smoothness is very low. They are also characterized by poor efficiency in numerical methods. The OFFs [3] were created by the author of this paper specifically for their application in numerical methods without the classical procedure of orthogonalization. The structure of some OFFs is presented here, and the novel FE for the ANSYS software is constructed on the basis of these OFFs. The corresponding discrete modeling of homogeneous and heterogeneous elastic plates was made. The series of approximate solutions for the plane problem were obtained and analyzed. This analysis shows that the application of the OFFs in the FE provides an increase in accuracy of approximate solutions in comparison with the classical FE. Besides, the solution requires much less computational time.

Mixed finite elements are well known, but classical mixed FEs [4-9] have a strong disadvantage – the number of unknown variables at each node is significantly higher than that in the case of FE connected with the Lagrange's variational principle. Orthogonal finite functions [3] provide possibilities for exception of a part of unknown values at grid nodes

(stresses, strains) prior to the solution of FE systems formulated using mixed numerical methods. The fundamental properties of the basic functions (functions are compactly supported – finite functions) of numerical methods are retained in that case. Thereby, the OFFs [3] remove the mentioned disadvantage of mixed numerical methods. Mixed FEs allow obtaining approximate solutions for derivatives (strains and stresses) of the main unknown function (displacement) without numerical differentiation, because the derivatives are approximated independently [3,4-9]. Consequently, the approximate solutions [3,4-9] for derivatives (strains and stresses) have accuracy and smoothness same as those of solutions for displacement. The computational time of the mixed FEMs [3] is less than that of classical mixed FEMs [4-9]. The computational time of mixed FEMs [3] is approximately equal to the computational time of classical FEMs connected with the Lagrange's variational principle.

ANSYS allows creating a new FE by means of linking an additional dynamical Fortran library. Here, on the examples of plane problems of elasticity, it is shown for the FEM of ANSYS connected with the Lagrange's variational principle that application of OFFs also increases the accuracy of approximate solutions "in displacements" and simultaneously decreases the computational time significantly due to increase in the number of zero elements in global FE matrixes. Application of OFFs in 3D FE for elasticity gives similar results: high accuracy of approximate solutions and even more significant difference in computational time between the novel FEM (OFF) and the classic FE of ANSYS. These results are the content of the next article. Application area of the novel FE for plane problems of elasticity comprises problems of mechanics of deformable heterogeneous bodies. The FE allows obtaining approximate solutions for analysis of stress-strain states of heterogeneous bodies with significantly smaller computational time and with higher accuracy. Simplification of the construction structure by elimination of numerous small features becomes unnecessary in that case.

The base finite function [3]

$$\varphi^{(1)}(x) = \begin{cases} 1 + x, x \in [-1, -1 + H_1] \cup [-1 + H_2, 0], \\ -\alpha + 2(\alpha + H_1)(K_N - 1 - x)/H_2 - H_1, x \in [-1 + H_1, -1 + K_N], \\ -\alpha + 2(\alpha + H_2)(1 - K_N + x)/H_2 - H_1, x \in [-1 + K_N, -1 + H_2], \\ 1 - x, x \in [0, H_1] \cup [H_2, 1], \\ \beta + 2(\beta + H_1 - 1)(x - K_N)/H_2 - H_1, x \in [H_1, K_N], \\ \beta + 2(\beta + H_2 - 1)(K_N - x)/H_2 - H_1, x \in [K_N, H_2], \\ 0, x \notin [-1, 1], \end{cases} \quad (1)$$

where $K_N = (H_1 + H_2)/2, \alpha > 0, \beta > 0$; generates finite functions on the grid. The function (1) is the sum of the even functions – the B-spline of first degree which has the compact support $[-1, 1]$ and two B-splines of first degree with smaller compact supports. The uniform grid $a = x_1 < x_2 < \dots < x_N = b$ is used (h – the step of the grid). Then the function (1) generates the grid finite functions

$$\varphi_i(x) = \varphi^{(1)}(x/h - i) = \begin{cases} (x - x_{i-1})/h, x \in [x_{i-1}, x_{i-1} + h_1] \cup [x_{i-1} + h_2, x_i], \\ -\alpha + 2(\alpha h + h_1)(x_{i-1} + k_N - x)/h, x \in [x_{i-1} + h_1, x_{i-1} + k_N], \\ -\alpha + 2(\alpha h + h_2)(x - x_{i-1} - k_N)/(h(h_2 - h_1)), x \in [x_{i-1} + k_N, x_{i-1} + h_2], \\ (x_{i+1} - x)/h, x \in [x_i, x_i + h_1] \cup [x_i + h_2, x_{i+1}], \\ \beta + 2(\beta h + h_1 - h)(x - x_i - k_N)/(h(h_2 - h_1)), x \in [x_i + h_1, x_i + k_N], \\ \beta + 2(\beta h + h_2 - h)(x_i + k_N - x)/(h(h_2 - h_1)), x \in [x_i + k_N, x_i + h_2], \\ 0, x \notin [x_{i-1}, x_{i+1}], \end{cases} \quad (2)$$

where $k_N = h_1 + h_2/2$, $h_1 = H_1h$, $h_2 = H_2h$ ($0 \leq h_1 < h_2 \leq h$). Grids for OFFs can be non-uniform. The theorem [3] about approximate properties of a sequence of groups of the functions (2) on grids has been proved for the Sobolev's space. The condition [3] connects the free parameters (2) and defines their values for which the functions (2) are orthogonal on the grid. This property is valuable for algorithms of numerical methods. The main properties of basis functions of numerical methods (functions are compactly supported – finite functions) are remained and that improves the characteristics of the global FE matrix.

2. The finite element connected with OFFs

The novel FE, which is similar to the FE Plane142 of ANSYS, is being constructed. The local stiffness matrix, the vector of body forces and loads on a boundary are created for the quadrangular FE. The nodes of the base FE are assumed to have the following numbers and coordinates: 1(-1,-1), 2(1,-1), 3(1,1), 4(-1,1).

The system of equations of a plane problem of elasticity can be written in a matrix form:

$$\varepsilon = Bu, \sigma = D\varepsilon, B^T \sigma = f, \quad (3)$$

where $u = (u_x, u_y)^T$ – the displacement vector; $\varepsilon = (\varepsilon_{xx}, \varepsilon_{yy}, \varepsilon_{xy})^T$ – the strain vector;

$\sigma = (\sigma_{xx}, \sigma_{yy}, \sigma_{xy})^T$ – the stress vector; D – the symmetric matrix of elastic modules (has different components for "plain stress" and "plain strain" problems); B – the matrix differential operator; $f = (f_x, f_y)^T$ – the vector of body forces.

The approximations of components of the displacement vector have forms [10]

$$u_x(x, y) = \sum_{i=1}^{n_p} N_i(x, y)u_i, \quad u_y(x, y) = \sum_{i=1}^{n_p} N_i(x, y)v_i, \quad (4)$$

where u_i , v_i – unknown constant coefficients; n_p – the number of nodes of a grid; $N_i(x, y)$ – the shape functions which form a Lagrange's basis on the grid:

$$N_i(x_j, y_j) = \delta_{ij}, \quad \delta_{ij} = \begin{cases} 1, & i = j; \\ 0, & i \neq j \end{cases}$$

The problem (3) after the discretization (4) and after the exception of ε and σ is written as

$$Ku = f, \quad K = \sum_{(e)} k^{(e)}, \quad f = \sum_{(e)} f^{(e)},$$

where

$$k^{(e)} = \int_{S^{(e)}} B^T DB dS, \quad f^{(e)} = \int_{S^{(e)}} N^T f dS + \int_{l^{(e)}} N^T p dl \quad (5)$$

are accordingly a local stiffness matrix and a local vector of body forces and loads on the boundary for the FE $S^{(e)}$ ($p = (p_x, p_y)^T$ is a vector of a load on the boundary $l^{(e)}$ of the region $S^{(e)}$).

Structures of the classic local stiffness matrix (5) and the local vector of body forces and loads on the boundary (5) are described further for a classic bilinear quadrangular FE. These structures define also the subprograms for the novel FE, which is connected with OFFs.

The Gauss's formula was used for calculation of the integrals (5). The Gauss's points were generated, the nodes t_1, t_2, \dots, t_s and the coefficients W_1, W_2, \dots, W_s were taken so that the Gauss's formula

$$\int_{-1}^1 f(x) dx \cong \sum_{i=1}^s W_i f(t_i)$$

is exact for all polynomials of the degree $(2s - 1)$. The local stiffness matrix of the bilinear quadrangular FE is written for $s=2$ as

$$k^{(e)} = \int_{S^{(e)}} B_N^T DB_N dS = \sum_{i=1}^2 \sum_{j=1}^2 W_i W_j B_N^T(\xi_i, \eta_j) DB_N(\xi_i, \eta_j) \det|J(\xi_i, \eta_j)|, \quad (6)$$

where

$$B_N = B \cdot N^T = \begin{pmatrix} \frac{\partial}{\partial x} & 0 \\ 0 & \frac{\partial}{\partial y} \\ \frac{\partial}{\partial y} & \frac{\partial}{\partial x} \end{pmatrix} \begin{pmatrix} N_1 & 0 & N_2 & 0 & N_3 & 0 & N_4 & 0 \\ 0 & N_1 & 0 & N_2 & 0 & N_3 & 0 & N_4 \end{pmatrix} =$$

$$= \begin{pmatrix} \frac{\partial N_1}{\partial x} & 0 & \frac{\partial N_2}{\partial x} & 0 & \frac{\partial N_3}{\partial x} & 0 & \frac{\partial N_4}{\partial x} & 0 \\ 0 & \frac{\partial N_1}{\partial y} & 0 & \frac{\partial N_2}{\partial y} & 0 & \frac{\partial N_3}{\partial y} & 0 & \frac{\partial N_4}{\partial y} \\ \frac{\partial N_1}{\partial y} & \frac{\partial N_1}{\partial x} & \frac{\partial N_2}{\partial y} & \frac{\partial N_2}{\partial x} & \frac{\partial N_3}{\partial y} & \frac{\partial N_3}{\partial x} & \frac{\partial N_4}{\partial y} & \frac{\partial N_4}{\partial x} \end{pmatrix},$$

the derivatives of the shape functions N_i in the global (x, y) and in local (ξ, η) coordinate systems are connected by the Jacobi's matrix J .

The algorithm of calculation of the first integral in the right part of the second formula (5) is similar to (6), but for the second integral it is necessary to make an additional explanation. That can be illustrated on the example of the part of the FE boundary with nodes 2(1,-1) and 3(1,1) and the local coordinate $\xi = 1$. For this part of the boundary, the classical shape functions have the forms:

$$N_1 = \frac{(1 - \xi)(1 - \eta)}{4} = 0, \quad N_2 = \frac{(1 + \xi)(1 - \eta)}{4} = \frac{1 - \eta}{2},$$

$$N_3 = \frac{(1 + \xi)(1 + \eta)}{4} = \frac{1 + \eta}{2}, \quad N_4 = \frac{(1 - \xi)(1 + \eta)}{4} = 0,$$

consequently, in the case of a constant load on the boundary

$$\int_{l^{(e)}} N^T p dl = l^{(e)} \int_{-1}^1 N^T \cdot p d\eta =$$

$$= \frac{l^{(e)}}{2} \int_{-1}^1 \begin{pmatrix} 0 & 0 & (1 - \eta) & 0 & (1 + \eta) & 0 & 0 & 0 \end{pmatrix}^T \cdot \begin{pmatrix} p_x \\ p_y \end{pmatrix} d\eta =$$

$$= l^{(e)} \begin{pmatrix} 0 & 0 & p_x & p_y & p_x & p_y & 0 & 0 \end{pmatrix}^T.$$

The creation of the novel FE of ANSYS on the base of OFFs is similar to the creation of the classic FE of ANSYS. The structure of the subprogram UserElem.f of ANSYS was used for that. This structure defines the variables, the functions, the computations of derivatives of

shape functions, the construction of the Jacobi's matrix, the creation of local and global stiffness matrices, verifications, and output of results.

The grid functions

$$\varphi_i(x) = \begin{cases} \frac{(\sqrt{2}-1)(x_{i-1}-x)}{h_{i-1}}, & x \in \left[x_{i-1}, x_{i-1} + \frac{h_{i-1}}{2}\right]; \\ \frac{(\sqrt{2}+1)(x-x_i)}{h_{i-1}} + 1, & x \in \left[x_{i-1} + \frac{h_{i-1}}{2}, x_i\right]; \\ \frac{(\sqrt{2}-1)(x-x_i)}{h_i} + 1, & x \in \left[x_i, x_i + \frac{h_i}{2}\right]; \\ \frac{(\sqrt{2}+1)(x_{i+1}-x)}{h_i}, & x \in \left[x_i + \frac{h_i}{2}, x_{i+1}\right]; \\ 0, & x \notin [x_{i-1}, x_{i+1}] \end{cases}$$

follow from (2) and for the given values of parameters are orthogonal on non-uniform grids.

The shape functions for the novel bilinear quadrangular FE are the tensor products of single-argument OFFs

$$N_i = \varphi_i(\xi)\varphi_i(\eta), \quad i = \overline{1,4}; \tag{7}$$

and are defined in local coordinates by Table 1.

Table 1. OFFs for the shape functions (7)

	$\varphi_i(\xi)$	$\varphi_i(\eta)$
N_1	$\begin{cases} \frac{(\sqrt{2}-1)(\xi+1)}{2} + 1, & \xi \in [-1,0] \\ \frac{(\sqrt{2}+1)(1-\xi)}{2}, & \xi \in [0,1] \end{cases}$	$\begin{cases} \frac{(\sqrt{2}-1)(\eta+1)}{2} + 1, & \eta \in [-1,0] \\ \frac{(\sqrt{2}+1)(1-\eta)}{2}, & \eta \in [0,1] \end{cases}$
N_2	$\begin{cases} \frac{(\sqrt{2}-1)(-1-\xi)}{2}, & \xi \in [-1,0] \\ \frac{(\sqrt{2}+1)(\xi-1)}{2} + 1, & \xi \in [0,1] \end{cases}$	$\begin{cases} \frac{(\sqrt{2}-1)(\eta+1)}{2} + 1, & \eta \in [-1,0] \\ \frac{(\sqrt{2}+1)(1-\eta)}{2}, & \eta \in [0,1] \end{cases}$
N_3	$\begin{cases} \frac{(\sqrt{2}-1)(-1-\xi)}{2}, & \xi \in [-1,0] \\ \frac{(\sqrt{2}+1)(\xi-1)}{2} + 1, & \xi \in [0,1] \end{cases}$	$\begin{cases} \frac{(\sqrt{2}-1)(-1-\eta)}{2}, & \eta \in [-1,0] \\ \frac{(\sqrt{2}+1)(\eta-1)}{2} + 1, & \eta \in [0,1] \end{cases}$
N_4	$\begin{cases} \frac{(\sqrt{2}-1)(\xi+1)}{2} + 1, & \xi \in [-1,0] \\ \frac{(\sqrt{2}+1)(1-\xi)}{2}, & \xi \in [0,1] \end{cases}$	$\begin{cases} \frac{(\sqrt{2}-1)(-1-\eta)}{2}, & \eta \in [-1,0] \\ \frac{(\sqrt{2}+1)(\eta-1)}{2} + 1, & \eta \in [0,1] \end{cases}$

The subprogram for computation of values of the shape functions (7) is constructed by use of FORTRAN 77 programming language.

Let the variables *ft* and *fs* correspond to the basis functions $\varphi_i(\xi)$ and $\varphi_i(\eta)$, and *intPnt* be the number of nodes of the FE, then Part 1 of the subprogram for the shape functions (7) has the following form:

Part 1 of the subprogram

```

if (intPnt.EQ.1) then
  ft(1)=((((sqrt(2.)-1.)*(-Pnt(1,1)+1.))/2.)+1.)
  ft(2)=((((sqrt(2.)-1.)*(-1.+Pnt(1,2)))/2.))
  ft(3)=((((sqrt(2.)-1.)*(-1.+Pnt(1,3)))/2.))
  ft(4)=((((sqrt(2.)-1.)*(-Pnt(1,4)+1.))/2.)+1.)
  fs(1)=((((sqrt(2.)-1.)*(-Pnt(2,1)+1.))/2.)+1.)
  fs(2)=((((sqrt(2.)-1.)*(-Pnt(2,2)+1.))/2.)+1.)
  fs(3)=((((sqrt(2.)-1.)*(-1.+Pnt(2,3)))/2.))
  fs(4)=((((sqrt(2.)-1.)*(-1.+Pnt(2,4)))/2.))
end if
if (intPnt.EQ.2) then
  ft(1)=((((sqrt(2.)+1.)*(1.-Pnt(1,1)))/2.))
  ft(2)=((((sqrt(2.)+1.)*(Pnt(1,2)-1.))/2.)+1.)
  ft(3)=((((sqrt(2.)+1.)*(Pnt(1,3)+1.))/2.)+1.)
  ft(4)=((((sqrt(2.)+1.)*(1.-Pnt(1,4)))/2.))
  fs(1)=((((sqrt(2.)-1.)*(-Pnt(2,1)+1.))/2.)+1.)
  fs(2)=((((sqrt(2.)-1.)*(-Pnt(2,2)+1.))/2.)+1.)
  fs(3)=((((sqrt(2.)-1.)*(-1.+Pnt(2,3)))/2.))
  fs(4)=((((sqrt(2.)-1.)*(-1.+Pnt(2,4)))/2.))
end if
if (intPnt.EQ.3) then
  ft(1)=((((sqrt(2.)+1.)*(1.-Pnt(1,1)))/2.))
  ft(2)=((((sqrt(2.)+1.)*(Pnt(1,2)-1.))/2.)+1.)
  ft(3)=((((sqrt(2.)+1.)*(Pnt(1,3)+1.))/2.)+1.)
  ft(4)=((((sqrt(2.)+1.)*(1.-Pnt(1,4)))/2.))
  fs(1)=((((sqrt(2.)+1.)*(1.-Pnt(2,1)))/2.))
  fs(2)=((((sqrt(2.)+1.)*(1.-Pnt(2,2)))/2.))
  fs(3)=((((sqrt(2.)+1.)*(Pnt(2,3)-1.))/2.)+1.)
  fs(4)=((((sqrt(2.)+1.)*(Pnt(2,4)-1.))/2.)+1.)
end if
if (intPnt.EQ.4) then
  ft(1)=((((sqrt(2.)-1.)*(-Pnt(1,1)+1.))/2.)+1.)
  ft(2)=((((sqrt(2.)-1.)*(-1.+Pnt(1,2)))/2.))
  ft(3)=((((sqrt(2.)-1.)*(-1.+Pnt(1,3)))/2.))
  ft(4)=((((sqrt(2.)-1.)*(-Pnt(1,4)+1.))/2.)+1.)
  fs(1)=((((sqrt(2.)+1.)*(1.-Pnt(2,1)))/2.))
  fs(2)=((((sqrt(2.)+1.)*(1.-Pnt(2,2)))/2.))
  fs(3)=((((sqrt(2.)+1.)*(Pnt(2,3)-1.))/2.)+1.)
  fs(4)=((((sqrt(2.)+1.)*(Pnt(2,4)-1.))/2.)+1.)
end if

```

The cycle operator was used for the computation of values of the shape functions (7) in the nodes of the FE. Let $N_n(i)$, ($i = \overline{1,4}$) be an array of values of the shape functions (7) at all nodes of the FE. Part 2 of the subprogram for this case is presented below.

The shape functions (7) are formed in the subprogram, and their values are transmitted to the system variables of the FE library. The local stiffness matrix and the local load vector were created similarly to such matrix and vector of the FE Plane142 of ANSYS. The novel FE was created in the FE library of ANSYS and was named as User300.

Part 2 of the subprogram

```

if (intPnt.EQ.1) then
  Nn(1)=ft(1)*fs(1)
  Nn(2)=(ft(2)*fs(2))
  Nn(3)=ft(3)*fs(3)
  Nn(4)=(fs(4)*ft(4))
end if
if (intPnt.EQ.2) then
  Nn(1)=ft(1)*fs(1)
  Nn(2)=ft(2)*fs(2)
  Nn(3)=ft(3)*fs(3)
  Nn(4)=ft(4)*fs(4)
end if
if (intPnt.EQ.3) then
  Nn(1)=ft(1)*fs(1)
  Nn(2)=ft(2)*fs(2)
  Nn(3)=ft(3)*fs(3)
  Nn(4)=ft(4)*fs(4)
end if
if (intPnt.EQ.4) then
  Nn(1)=ft(1)*fs(1)
  Nn(2)=ft(2)*fs(2)
  Nn(3)=ft(3)*fs(3)
  Nn(4)=ft(4)*fs(4)
end if

```

3. Solutions for the plane problems of elasticity for homogeneous and heterogeneous materials

Approximate solutions for several plane problems of elasticity were obtained and analyzed.

Problem 1. A homogeneous isotropic square plate is considered, the length of the side of the plate is equal to 2 m. The center of the plate coincides with the origin of coordinates. The modulus of elasticity is equal to 200 GPa, the Poisson's ratio is equal to 0.33. The side ($x=-1$) of the plate is fixed, and a uniform force $p_x=10$ N is applied to the opposite side ($x=1$); two sides ($y=-1, y=1$) of the plate are free (Fig. 1).

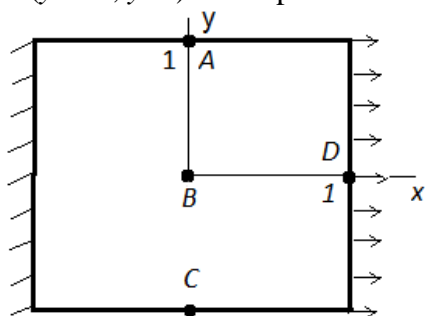


Fig. 1. The homogeneous square plate

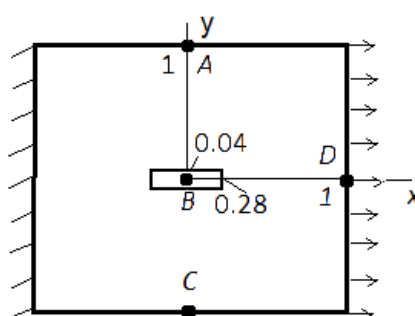


Fig. 2. The heterogeneous square plate

Series of computations were conducted for different numbers M of divisions along every side of the plate boundary, ranging from 10 to 100 (corresponds to the total number of FEs in the model ranging from 100 to 10000). Results of the computations are presented in Fig. 3 and in Tables 2-5 for the following points: points A (0, 1) and C (0, -1) are in the

middle of the opposite sides of the plate which are free (Fig. 1), point $B(0, 0)$ is in the center of the plate, and point D is in the middle of the side on which the external load is applied.

The computational time [ms] of the methods that use User300 (t_1) or Plane142 (t_2) for the different numbers M , and the coefficient $k=t_2/t_1$ are presented in Table 2 and are shown in Fig. 3. The coefficient k is the ratio of computational time of two FEMs. It increases with rise of total number of FE due to the zero elements in the global grid matrix produced by OFFs. Thereby, the obtained results prove that the novel FE provides high accuracy of the approximate solutions at a relatively low computational time.

Table 2

M	t_1	t_2	k
10	0.000	0.000	0.00
20	0.010	0.006	0.60
30	0.040	0.062	1.55
40	0.120	0.125	1.04
50	0.062	0.125	2.02
60	0.094	0.219	2.33
70	0.172	0.266	1.55
80	0.188	0.312	1.66
90	0.250	0.562	2.25
100	0.266	0.622	2.34

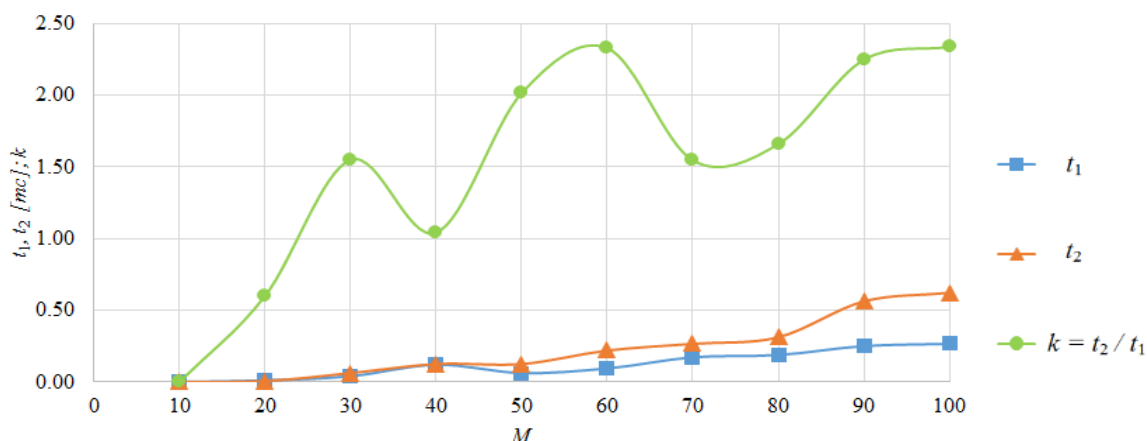


Fig. 3. The computational time and the coefficient k

Table 3

M	$10^9 U_{300}$ at point A	$10^9 U_{142}$ at point A	ε_1 at point A	ε_2 at point A
10	2.620063556	0.2914537501	798.963748142213	1.242032506472
20	2.623274810	0.5539481345	373.559643335165	1.120990817457
30	2.629161510	0.8163550033	222.061051793887	0.899103632349
40	2.635150100	1.078745142	144.279208999673	0.673375910899
50	2.644124400	1.341128972	97.156608738149	0.335107922839
60	2.650115000	1.603509427	65.269686312858	0.109304438525
66	2.650664780	1.760936616	50.525848342062	0.088581599477
70	2.651109410	1.865887724	42.083008312884	0.071822175841
76	2.651712470	2.023313942	31.057885529066	0.049091055545

80	2.652105320	2.128264497	24.613520722561	0.034283373708
86	2.652384210	2.285689993	16.043042500208	0.023771182318
90	2.652625110	2.390640126	10.958779665359	0.014690946720
96	2.652790241	2.548065063	4.109988379838	0.008466669491
100	2.652914453	2.653014863	0.003784750753	0.003784750753

Table 4

M	$10^9 U_{300}$ at point B	$10^9 U_{142}$ at point B	ε_1 at point B	ε_2 at point B
10	2.354386940	0.2530536263	830.390516201822	1.6634500738085
20	2.364379203	0.4911274176	381.418694674805	1.2460995301569
30	2.371358460	0.7290775710	225.254616836924	0.9545943222542
40	2.377346930	0.9669864625	145.851107765637	0.7044716813528
50	2.384330250	1.204875647	97.8901520614766	0.4127967726267
60	2.390327060	1.442753634	65.6781174324874	0.1623257918613
66	2.391776400	1.585476860	50.8553332024032	0.1017906721456
70	2.392956900	1.680624550	42.3849782510912	0.0524842921213
76	2.393279400	1.823344694	31.2576501785679	0.0390143153675
80	2.393484700	1.918490667	24.7587356649883	0.0304394743519
86	2.393581570	2.061208626	16.1251481197712	0.0263934692414
90	2.393666810	2.156353353	11.0053139792623	0.0228332186414
96	2.393899556	2.299069696	4.1247057522870	0.0131120303948
100	2.394299556	2.394213486	0.0035949175169	0.0035949175169

Table 5

M	$10^9 U_{300}$ at point D	$10^9 U_{142}$ at point D	ε_1 at point D	ε_2 at point D
10	4.840145745	0.5095828728	849.825043845155	1.748237213357
20	4.853458480	1.000479579	385.113197897665	1.477997482949
30	4.869125470	1.491258513	226.511160040566	1.159967930502
40	4.884046840	1.982001553	146.419930025151	0.857073971739
50	4.900145748	2.472727909	98.167607934739	0.530276769078
60	4.913012570	2.963444851	65.787211067624	0.269088778144
66	4.920997840	3.257872015	51.049452444497	0.106993069634
70	4.923254780	3.454155841	42.531345041302	0.061178677840
76	4.924048724	3.748580402	31.357692671414	0.045062138863
80	4.924617846	3.944862772	24.836227028077	0.033509338041
86	4.925134567	4.239285476	16.178412491511	0.023020242920
90	4.925547622	4.435566783	11.046634240249	0.014635499151
96	4.925885447	4.729988103	4.141603313458	0.007777874709
100	4.926427484	4.926268606	0.003225118497	0.003225118497

The values ($10^9 U_{300}$) [m] and ($10^9 U_{142}$) [m] of the displacement vector magnitude for selected points of the plate are presented in Tables 3-5. These displacements were received by two FEMs which are connected with User300 and Plane142 FEs. Tables 3-5 contain also: ε_1 [%] – a relative difference between the values of such two solutions obtained on the stated grid, and ε_2 [%] – a relative difference between the value of the User300 solution on the stated grid and the value of the Plane142 solution on the dense grid ($M=100$; 10000 FE). The solution obtained by use of Plane142 element on the dense grid is considered to be a reference solution for comparison with others, because an additional increase of the number of nodes of the grid gives only a variation of last ciphers of the mantissa.

A similar table for the point C coincides with the Table 3 and therefore is not provided. Tables 3-5 show a high accuracy of the approximate solutions obtained by the elements connected with OFF in comparison with those obtained by classical FEM of ANSYS, which is demonstrated by ε_1 . The accuracy ε_2 of the approximate solutions obtained by use of the novel FEM (OFF) increases with the increase in the number of grids' cells.

Problem 2. A heterogeneous square plate has the same sizes and properties as considered in Problem 1, but a small rectangular region ($-0.28 \leq x \leq 0.28$, $-0.04 \leq y \leq 0.04$) of the plate (Fig. 2) is assumed to be characterized by different material properties: the modulus of elasticity 160 GPa, and the Poisson's ratio 0.3. Boundary conditions are identical to those of Problem 1.

The results of computations are presented in Tables 6-8 show that the characteristics of approximate solutions for the heterogeneous plate (Problem 2) are similar to those of approximate solutions for the homogeneous plate (Problem 1). The FEM connected with OFF demonstrates a high accuracy of approximate solutions and reduced computational time in both Problems 1, 2. Thereby, this FEM and corresponding FE models are effective in the plane problems for elastic homogeneous and heterogeneous materials.

Table 6

M	$10^9 U_{300}$ in point A	$10^9 U_{142}$ in point A	ε_1 in point A	ε_2 in point A
50	2.647846135	1.344217665	96.9804596	0.427095692
60	2.652324564	1.636720729	62.05113781	0.258683251
70	2.656648790	1.894932755	40.19752326	0.096069672
80	2.657216879	2.183838367	21.67644454	0.074706547
90	2.658648790	2.449754511	8.527151519	0.020859178
100	2.658981676	2.659203478	0.008340919	0.008340919

Table 7

M	$10^9 U_{300}$ in point B	$10^9 U_{142}$ in point B	ε_1 in point B	ε_2 in point B
50	2.393236558	1.208636561	98.01126618	0.351401094
60	2.397841240	1.519945769	57.75834176	0.159673243
70	2.400094575	1.712669627	40.13762708	0.065849805
80	2.400833450	1.975710565	21.51746782	0.035084831
90	2.401236780	2.208970952	8.703864024	0.018291143
100	2.401451328	2.401676074	0.009357881	0.009357881

Table 8

M	$10^9 U_{300}$ in point D	$10^9 U_{142}$ in point D	ε_1 in point D	ε_2 in point D
50	4.921236855	2.482214775	98.25991304	0.485557091
60	4.930369854	3.162257695	55.91296882	0.300874787
70	4.940368468	3.541921705	39.48271248	0.098688522
80	4.942448468	4.128578203	19.71308826	0.056627949
90	4.943865875	4.566589689	8.261661574	0.027965962
100	4.944736478	4.945248861	0.010361117	0.010361117

Problems for plates with two and three small regions which have different properties were also solved. The obtained accuracy of approximate solutions and the computational time were found to be similar to such parameters for the Problems 1, 2 and are therefore not reported here.

Conclusions

The FEM connected with OFF and corresponding FE models were proved to be effective in plane problems for elastic homogeneous and heterogeneous bodies. This FEM allows obtaining approximate stress-strain state with high accuracy and relatively small computational time without simplification of the structure under consideration and without elimination of its small features. The results of computations illustrate that OFFs allow to improve significantly the characteristics not only of mixed FEMs in elasticity, but also of classical FEMs based on the Lagrange's variational principle, which form the basis of many FE codes, such as ANSYS. These FEs can be used in creating and investigating of heterogeneous materials.

Acknowledgements. No external funding was received for this study.

References

- [1] Strang G, Fix GJ. *An Analysis of the Finite Element Method*. New Jersey: Prentice-Hall Inc.; 1973.
- [2] Daubechies I. Orthonormal bases of compactly supported wavelets. *Comm. Pure and Appl. Math.* 1988;41(7): 909-996.
- [3] Leontiev VL. *Ortogonalnie finitnie funktsii i chislenie metodi [Orthogonal Finite Functions and Numerical Methods]*. Ulyanovsk: UISU; 2003. (In Russian)
- [4] Ciarlet P. *The Finite Element Method for Elliptic Problems*. Amsterdam: North-Holland Publ. Comp.; 1978.
- [5] Rozin LA. *Metod konechnykh elementov v primeneni k uprugim sistemam [FEM in Application to Elastic Systems]*. Moscow: Stroyizdat Publ.; 1977. (In Russian)
- [6] Poceski A. A mixed finite element method for bending of plates. *Int. J. Num. Meth. Eng.* 1975;9(1): 3-15.
- [7] Poceski A. *Mixed Finite Element Method*. Berlin: Springer; 1992.
- [8] Brezzi F, Douglas J, Marini LD. Two Families of Mixed Finite Elements for Second Order Elliptic Problems. *Numer. Math.* 1985;47(2): 217-235.
- [9] Boffi D, Brezzi F, Fortin M. *Mixed Finite Element Methods and Applications*. Springer Series in Computational Mathematics. Vol. 44. Berlin: Springer; 2013.
- [10] Zienkiewicz OC. *The finite element method in engineering science*. London: McGraw-Hill; 1971.

NEURAL NETWORKS AND DATA-DRIVEN SURROGATE MODELS FOR SIMULATION OF STEADY-STATE FRACTURE GROWTH

A.V. Kalyuzhnyuk^{1,2}, R.L. Lapin¹, A.S. Murachev^{1*}, A.E. Osokina¹, A.I. Sevostianov²,
D.V. Tsvetkov¹

¹Peter the Great St. Petersburg Polytechnic University, Polytechnicheskaya 29, St.Petersburg 195251, Russia

²Gazpromneft Science & Technology Centre, 75-79 lit. D Moika River emb., St Petersburg, 190000, Russia

*e-mail: andrey.murachev@gmail.com

Abstract. This work is devoted to an assessment of the application of machine learning algorithms in the prediction of a fracture's aspect ratio caused by the hydraulic fracturing. By the aspect ratio in this work is assumed the ratio of the larger half-axis of the fracture to the smaller one. The study shows the prospects of applying data-driven surrogate model methods (deep neural networks learning from data simulated by means of traditional solvers) to particle dynamics modelling of hydraulic fracturing. The solution obtained allows to predict the aspect ratio value quickly, and thus, to evaluate the volume of the hydraulic fracturing fluid injection necessary to achieve the required fracture length.

Keywords: neural networks, surrogate model, hydraulic fracturing, crack

1. Introduction

Nowadays, hydraulic fracturing has become the main method to increase oil production from conventional and unconventional fields. Hydraulic fracturing is a stimulation technique in which a high-permeable fracture is created in a productive layer by a pressurized liquid [1].

Hydraulic fracturing planning, support, and optimization are implemented using the special software (e.g. MFrac, FracPro, FracCADE, Mangrove). These tools use basic analytic solutions in hydraulic fracturing theory [2], and some of the contemporary numerical modelling techniques (Pseudo3D [3], Planar3D [3], and Full3D [4]). Such modelling includes the solution of partial differential equations with corresponding initial and boundary conditions [5]. The amount of the equations can be of high order (10^6 – 10^9), making such tasks computationally expensive.

The alternatives to resource-intensive numerical modelling are meta-modelling, surrogate modelling [6] or model order reduction approach [7]. These approaches allow to simulate physical systems with lower resource costs while maintaining acceptable accuracy. The modern rapid development of deep learning methods [8] makes it possible to use results obtained by traditional numerical solvers as surrogates [9] to accelerate computationally expensive calculations.

Deep learning technology is a subtype of machine learning most often implemented by artificial neural networks. Deep learning allows to find implicit dependencies and predict the desired values of the target function by processing huge data sets (big data). In particular, this approach becomes a common instrument in problems of the petroleum industry [10,11,12].

To gain high predictive ability, deep learning instruments require large training sample size. Therefore, the amount of data available in natural experiments may not be sufficient. In such cases, the necessary amount of training data can be obtained by modelling: e.g., by

carrying out a number of numerical experiments. The models constructed on the basis of this approach are called data-driven surrogate models [13,14]. In recent years, this approach has shown great success, for instance, in the tasks of accelerating resource-intensive simulations in computational fluid dynamics [13], electric potential distribution [14], heat transfer [15], etc. In these works, deep neural networks are trained on data simulated with traditional solvers.

In this paper, the analogous approach is used to accelerate the hydraulic fracturing simulation process and to calculate the geometric parameter of the resulted fracture: the aspect ratio value describing the proportional relationship between the larger half-axis of the fracture and the smaller one. The training database is generated using the numerical simulation by means of the particle dynamics method.

2. The steady-state hydraulic fracture modelling

The steady-state hydraulic fracture model is formulated as follows: the fracture is considered to be located in a linearly elastic material; the material consists of three parallel layers lying in the XY plane (Fig. 1); the productive layer is located between the semi-infinite side layers. Parameters of the model are: σ_i is the reservoir stress of the i^{th} layer; K_i is the critical stress intensity factor of the i^{th} layer; E'_i is the elastic modulus of the i^{th} layer multiplied by $\frac{E_i}{1-\nu_i^2}$, where E_i is a Young's modulus and ν_i is a Poisson's ratio of the i^{th} layer; L is the half thickness of the productive layer; V is the volume of the injected hydraulic fracturing fluid.

The challenge is to determine the geometric parameters of the resulting fracture loaded with uniform pressure.

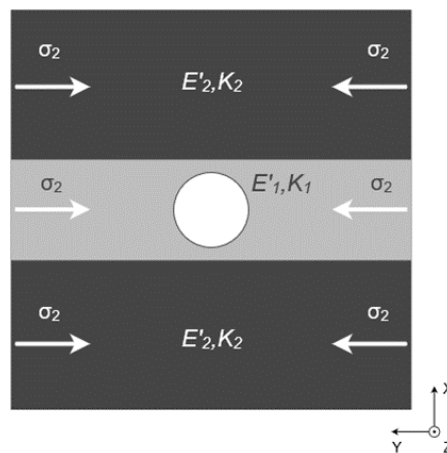


Fig. 1. The structure of the fracture between layers with different stress values

One of the ways to determine the geometric parameters of the resulting fracture in the material is to simulate its growth by the particle dynamics method [16,17].

The particle dynamics method is based on the representation of a material by a set of interacting particles (material points or solid bodies), for which classical dynamic equations are written. The interaction of particles is described by means of the interaction potentials, the main property of which is a short-range repulsion and long-range attraction mechanisms. Before the start of the simulation, the initial distribution of particles in space (i.e. the initial structure of the material) and the initial distribution of particle velocities are specified. This method allows to solve the problem in a three-dimensional formulation and to set various reservoir stresses and physical properties of layers.

One of the benefits of this approach compared to other methods, such as the boundary elements method [18] or the extended finite elements method [19], is that the particle

dynamics method eliminates the necessity of the explicit analytical description of objects' boundaries and geometry [20].

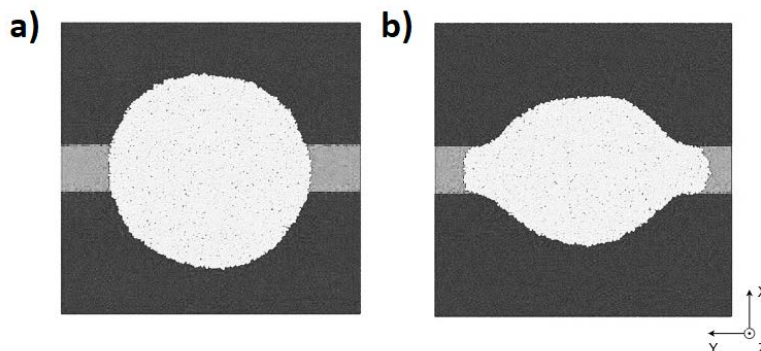


Fig. 2. Examples of the steady-state hydraulic fracture model in the fractured layer obtained by particle dynamics method. Black dots denote side layers. Grey dots denote the productive layer. White dots denote the fracture zone: a) the initial fracture; b) the fracture growing process

The reservoir initial configuration is a rectangular parallelepiped. The initial geometry of the fracture is a cylinder. The particle dynamics simulation continues until the least distance between particles denoting the fracture zone and particles denoting the border zone becomes less than 10% of the model size. The aspect ratio value in the paper is evaluated as the ratio of the greatest distance by the axis Y between particles denoting the fracture zone to the corresponding distance by the axis X (Fig. 2).

The using particle dynamics method implemented with C++ is fully described in [16]. However, such simulation is computationally expensive. To speed-up the calculation process the approximation models are commonly used, which can describe the processes occurring in the medium under consideration. The basic idea of approximation models is to construct the approximation function on the basis of previously performed calculations. As a result of the construction, numerical simulation is reduced to the calculation of this function value.

There are many ways to construct an approximation function. In particular, in modern practice major advances have been achieved in the development of machine learning methods which allow to construct approximation functions of almost any complexity.

3. The machine learning approach

Machine learning is the scientific study of algorithms and statistical models trained on large datasets. It is made instead of specifying their parameters explicitly [21].

The prediction of a hydraulic fracture aspect ratio belongs to the regression problem of the class of so-called «supervised machine learning» tasks. In the regression problem the goal is to predict a certain target variable for a given set of characteristics of the observed object. Thus, each sample in a training dataset (the part of the dataset that is used to train the algorithm) consists of input parameters and a target value.

At the first step, the structure of the training sample is formed thusly: preprocessed data contains feature vectors x of input parameters used in the particle dynamics method to obtain the model of the fracture (item 2). These parameters (features) are transformed to dimensionless in the following way [22]:

$$x = \left[\frac{E'2}{E'1} \frac{K_2}{K_1} \frac{K_1}{\Delta\sigma\sqrt{L}} \frac{E'1V}{\Delta\sigma L^3} \right]. \quad (1)$$

Each element from x is mapped to the certain aspect ratio value from the corresponding vector y : $y = [AR]$, where $[AR]$ means the vector of aspect ratio values, $\Delta\sigma$ is the stress

difference between the productive and the side layers and the other values are defined in item 2, E'_1 and K_1 are related to the productive layer, whereas E'_2 and K_2 are related to the side layers, AR is the aspect ratio value of the fracture.

The objective is to find such function $f(x)$ that would approximate the dataset with as high accuracy as possible: $f(x) = y$.

The chosen machine learning method to approximate this function is a deep fully connected neural network. So, in this case, the neural network represents the function $f(x)$, and the final objective is to find the right architecture. It is implemented using Python's framework Keras [23]: a high-level open source API capable of running on top of TensorFlow library.

The process of a neural network training is an iterative reduction of the loss (error) function value by adjusting the weights of the neural network using the gradient descent method. Each iteration is called "the epoch". One epoch consists of one complete training cycle on the training dataset which includes several training iterations on smaller sub-datasets (batches). The loss function on each epoch produces one value describing the difference between the predicted values for each feature vector x and the corresponding values of y . The ability of the neural network to predict correctly new examples that differ from those used for training is also evaluated on each epoch. It is evaluated the same way by using the test dataset instead of the training dataset.

The dataset used is generated by varying the feature values of x in ranges shown in Table 1. Values of features are varied under the assumption of the fact that the fracture volume increases for every configuration of listed parameters because of the permanent fluid injection. Thus, the calculation of the aspect ratio value is performed by the particle dynamics method for each feature set (it. 2). The process of the fracture growing is modeled several times (for instance, four times) for the same feature values, because the initial distribution of particles is set stochastically. Therefore, there are four different aspect ratio values for each input feature vector.

Table 1. The range of feature values variation

Feature	$\frac{E'_2}{E'_1}$	$\frac{K_2}{K_1}$	$\frac{K_1}{\Delta\sigma\sqrt{L}}$	$\frac{E'_1V}{\Delta\sigma L^3}$
Minimum value	0.2	0.2	0.01	0
Maximum value	5	5	1	20

Hence, the input (training set) is the matrix of the dimension $N \times M$, where N is the number of elements in training dataset and M is the dimension of the feature vector x . The used dataset is split into 630000 samples for the training set and 157000 for the test set (approximately 80% to 20% of the whole dataset).

The values of the resulting input (training matrix) are linearly scaled from 0 to 1 for a fair comparison between them. Also, it is a well-known fact that feature scaling can improve the convergence speed of the gradient descent algorithm used while adjusting the weights of the neural network [24]. The most widely used measure of forecast accuracy is "Mean Absolute Percentage Error" (MAPE) [25]. It is used in the paper as the loss function.

4. Architecture setting

Any neural network in addition to the weights adjusted during the training process is also characterized by a set of hyperparameters defining the neural network architecture. The quality of results produced by an artificial neural network depends significantly on the proper hyperparameters configuration. The selection of the model hyperparameters in this work is

implemented using the random search algorithm: different neural network architectures are generated by selecting the hyperparameters' values randomly.

The number of hidden layers of the neural network is varied and some hyperparameters are varied within each hidden layer: the number of neurons (32, 64, 128, and 256); the neurons' activation function ("relu", "tanh", "linear", "sigmoid"); the dropout value (0, 0.1, 0.2, 0.3); the size of batch sub-datasets: 8, 16, 32.

Neural networks generated with different hyperparameters values (different architectures) are then evaluated via the cross-validation method [26], and the best architecture is chosen. Cross validation is used to eliminate the effect of the dataset splitting into the training and test set when evaluating the quality of the choice of the neural network hyperparameters.

For each set of hyperparameters the new configuration of the neural network is constructed, trained and cross-validated on the equal number of epochs. The final configuration of the neural network that demonstrated the most optimal result is shown in Fig. 3.

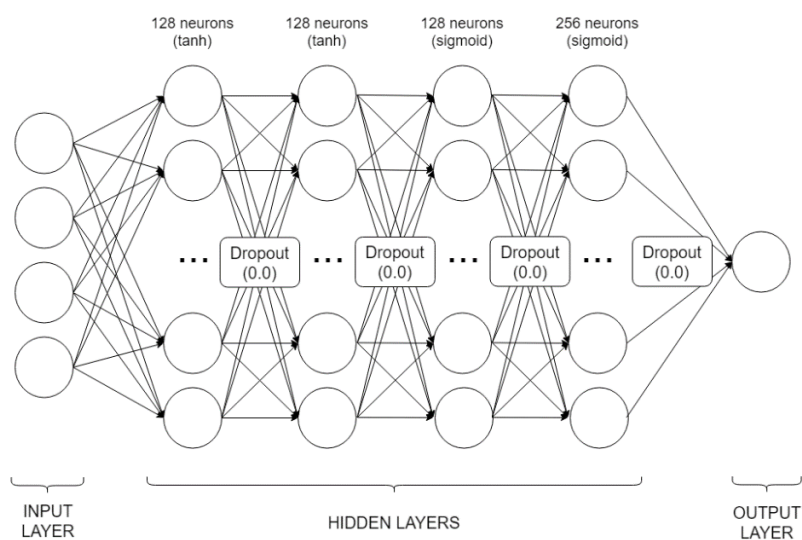


Fig. 3. The configuration of the neural network

5. Results

As anticipated, the loss values of the neural network used decline with the epoch number increasing for both the train and test sets. The training process is stopped after the 300th epoch: the chosen loss value (MAPE) on the number of epochs for test dataset fluctuates around a constant value. Figure 4 demonstrates that the MAPE value does not exceed 5% on a significant part of the test set (more than 80% of 157000 test samples). Figure 5 shows the example of the comparison between the fracture's aspect ratio values calculated by means of the particle dynamics method and neural network results. These results are obtained by assuming that parameters $\frac{E_2'}{E_1'}$, $\frac{K_2}{K_1}$, $\frac{K_1}{\Delta\sigma\sqrt{L}}$ are constant. For this reason, we can see how the dimensionless parameter $\frac{E_1'V}{\Delta\sigma L^3}$ affects the changes in fracture growth.

A scatter of aspect ratio values is caused by the fact that the initial distribution of the fracture particles was set stochastically. Therefore, fracture distribution process is modelled four times for the same feature vector.

These examples show that the fracture's aspect ratio values calculated with the neural network accurately approximate fracture's aspect ratio values calculated with particle dynamics method.

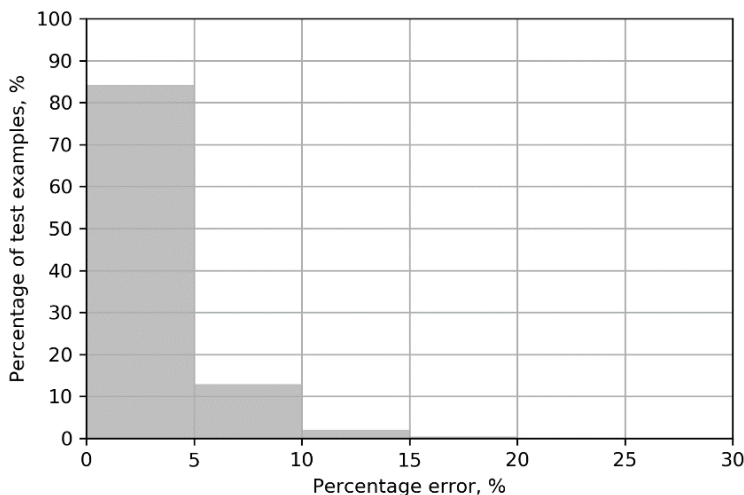


Fig. 4. The neural network's MAPE distribution on the test data

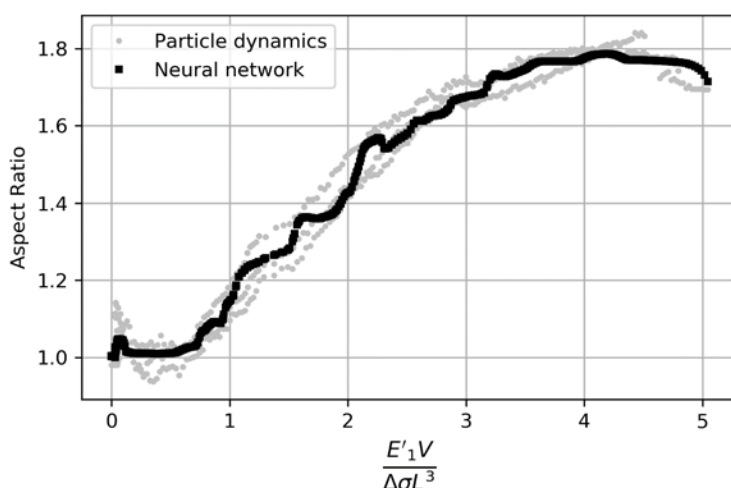


Fig. 5. The example of the results comparison for:

$$\frac{E'_2}{E'_1} = 2.8; \frac{K_2}{K_1} = 0.2; \frac{K_1}{\Delta \sigma \sqrt{L}} = 1.2875$$

6. Conclusion

As a result of this work, the practical scientific and technical significance of the proposed approach is proved. The data-driven surrogate modeling approach is successfully applied to the task of evaluating the steady-state hydraulic fracture shape. The most optimal architecture and the hyperparameters of the deep neural network are found by means of the random search algorithm. The artificial neural network is trained and validated using the dataset generated by the particle dynamics. During the surrogate modeling process, the neural network's hyperparameters are varied for each hidden layer and the most optimal ones are used.

Thus, the calculation time is decreased from 1.5 hrs. to 0.05 sec. At the same time, the accuracy is maintained on a high level since the MAPE value does not exceed 5%. The number of examples with larger error values decreases significantly with the percentage error increasing. The result obtained demonstrates the promising perspectives of machine learning application in the area of such problems as physical quantities prediction on the basis of numerically obtained data. Unlike the existing numerical simulation methods to solve the task, the application of machine learning algorithms does not involve significant time and computational costs and can be considered as the most optimal.

Acknowledgments. *This work was supported by Ministry of Science and Higher Education of the Russian Federation within the framework of the Federal Program "Research and development in priority areas for the development of the scientific and technological complex of Russia for 2014 – 2020" (activity 1.2), grant No. 14.575.21.0146 of September 26, 2017, unique identifier: RFMEFI57517X0146. The industrial partner of the grant is LLC "Gazpromneft Science & Technology Centre".*

References

- [1] Gandossi L, Von Estorff U. *An overview of hydraulic fracturing and other reservoir stimulation technologies for shale gas production – Update 2015*. Available from: <https://ec.europa.eu/jrc/en/publication/eur-scientific-and-technical-research-reports/overview-hydraulic-fracturing-and-other-formation-stimulation-technologies-shale-gas-0> [Accessed 15th august 2019].
- [2] Linkov AM. The particle velocity, speed equation and universal asymptotics for the efficient modelling of hydraulic fractures. *J. Appl. Math. Mech.* 2015;79(1): 54-63.
- [3] Meyer B. Design formulae for 2-d and 3-d vertical hydraulic fractures: Model comparison and parametric studies. In: *Proc. Unconventional Gas Technology Symposium*. Society of Petroleum Engineers; 1986. p.391-408.
- [4] Khasanov M, Paderin G, Shel E, Yakovlev A, Pustovskikh A. Approaches to modeling hydraulic fracturing and their development. *Oil Industry Journal*. 2017;2017(12): 37-41. (In Russian)
- [5] Gladkov IO, Linkov AM. Solution of a Plane Hydrofracture Problem with Stress Contrast. *Journal of Applied Mechanics and Technical Physics*. 2018;59(2): 341-351.
- [6] Ahmed M, Qin N. Surrogate-based aerodynamic design optimization: Use of surrogates in aerodynamic design optimization. In: *Proc. of 13th International Conference on Aerospace Sciences & Aviation Technology*; 2009. p.ASAT-13-AE-14.
- [7] Schilders Wil, Van der Vorst H, Rommes J. *Model Order Reduction: Theory, Research Aspects and Applications*. Berlin: Springer; 2008.
- [8] Bengio Y. Learning deep architectures for AI, Foundations and trends in Machine Learning. *Journal Foundations and Trends in Machine Learning*. 2009;2(1): 1-127.
- [9] Kononenko O, Kononenko I. *Machine Learning and Finite Element Method for Physical Systems Modeling*. Arxiv [Preprint] 2018. Available from: <https://arxiv.org/abs/1801.07337> [Accessed: 15 July 2018].
- [10] Andrianova A, Simonov M, Perets D, Margarit A, Serebryakova D, Bogdanov Y, Budenny S, Volkov N, Tsanda A, Bukharev A. *Application of Machine Learning for Oilfield Data Quality Improvement*. Society of Petroleum Engineers; 2018.
- [11] Simonov MV, Perets DS, Kotezhkov VS. Adaptive Tool for Solving Applied Problems of Oil Engineering. In: *Proc. of 20th conference on oil and gas geological exploration and development*; 2018.
- [12] Chebyshev IS, Baryshnikov ES, Legkokonets VA. Application of machine learning to predict the acoustic properties of rock samples. *Proneft*. 2018;4(10): 67-70.
- [13] Parish EJ, Duraisamy K. A paradigm for data-driven predictive modeling using field inversion and machine learning. *J. Comput. Phys.* 2016;305: 758-774.
- [14] Shan T, Tang W, Dang X, Li M, Yang F, Xu Shu, Wu J. Study on a Poisson's Equation Solver Based On Deep Learning Technique. Arxiv [Preprint] 2017. Available from: <https://arxiv.org/abs/1712.05559>.
- [15] Sharma RI, Farimani AB, Gomes J, Eastman P, Pande V. Weakly-Supervised Deep Learning of Heat Transport via Physics Informed Loss. Arxiv [Preprint] 2018. Available from: <https://arxiv.org/abs/1807.11374>.

- [16] Tsaplin VA, Kuzkin VA. On using quasi-random lattices for simulation of isotropic materials. *Materials Physics and Mechanics*. 2017;32(3): 321-327.
- [17] Krivtsov AM. Molecular Dynamics Simulation of Plastic Effects upon Spalling. *Physics of the Solid State*. 2004;46(6): 1055-1060.
- [18] Linkov A. *Boundary Integral Equations in Elasticity Theory*. Kluwer: Dordrecht; 2002.
- [19] Liu F, Gordon PA, Valiveti DM. Modeling competing hydraulic fracture propagation with the extended finite element method. *Acta Geotechnica*. 2017;13(2): 243-265.
- [20] Li Z, Bian X, Tang YH, Karniadakis GE. A dissipative particle dynamics method for arbitrarily complex geometries. *Journal of Computational Physics*. 2016;355: 534-547.
- [21] Bishop CM. *Pattern Recognition and Machine Learning*. Springer; 2006.
- [22] Shel EV, Paderin GV. Analytical solution of the pseudo-3D model for hydraulic fracturing in a storage-dominated regime. *Int. J. Rock. Mech. Min. Sci.* 2019;114: 92-100.
- [23] Gulli A, Pal S. *Deep Learning with Keras*. Packt Publishing Ltd; 2017.
- [24] Grus J. *Data Science from Scratch*. Sebastopol, CA: O'Reilly; 2015.
- [25] Tofallis C. Better Measure of Relative Prediction Accuracy for Model Selection and Model Estimation. *Journal of the Operational Research Society*. 2014;66(8): 1352-1362.
- [26] Grossman R, Seni G, Elder J, Agarwal N, Liu H. *Ensemble Methods in Data Mining: Improving Accuracy Through Combining Predictions*. Morgan & Claypool; 2010.

MODELING PLASTIC DEFORMATION AND DAMAGE ACCUMULATION PROCESSES IN STRUCTURAL STEELS UNDER BLOCK NON-SYMMETRIC LOW-CYCLE LOADING

Ivan A. Volkov*, Leonid A. Igumnov, Denis N. Shishulin

Research Institute for Mechanics, National Research Lobachevsky State University of Nizhny Novgorod,
Nizhny Novgorod, 23 Prospekt Gagarina (Gagarin Avenue) BLDG 6, 603950, Russia

*e-mail: pmptmvgavt@yandex.ru

Abstract. To assess the reliability and the scope of applicability of the defining relations of mechanics of damaged media (MDM) [1,2], plastic deformation and damage accumulation processes in a number of structural steels under low-cycle loading have been numerically investigated, and the obtained numerical results have been compared with the data from full-scale experiments. It is shown that the introduced MDM model qualitatively and quantitatively describes the main effects of plastic deformation and damage accumulation processes in structural alloys under block-type non-stationary non-symmetric low-cycle loading.

Keywords: low-cycle fatigue, plastic deformation, damage degree, block-type loading, mechanics of damaged media, modeling, numerical and full-scale experiment

1. Introduction

Many years of experimentally and theoretically studying fatigue damage accumulation in structural materials make it possible to conclude that fatigue covers the three significantly different regions of cyclic loading [3]: high-cycle fatigue (HCF), when a material works quasi-elastically, corresponding to durability values under uniaxial symmetric cyclic loading in the range of 10^5 - 10^8 cycles and higher; low-cycle fatigue (LCF), when a material undergoes non-stationary elastoplastic deformation, corresponding to the durability values under uniaxial symmetric cyclic loading up to 10^4 cycles; an intermediate region corresponding to the durability values of 10^4 - 10^5 cycles, where both the mechanisms of degradation of the initial strength properties of the material are simultaneously active.

Classical methods for predicting fatigue life using semi-empirical formulas (law) based on a stable analysis of the deformation process and connecting the parameters of loops of elastoplastic deformation with a number of cycles prior to failure require a large amount of experimental data and are valid only for a narrow range of loading conditions [1-3].

Damage and fatigue failure of structural materials is caused mainly by nucleation of microdefects, their growth and merging into macroscopic cracks. The description of the mechanical behavior of microdefects is no less important than the description of macrocrack nucleation. In the last decade a new scientific direction of mechanics of damaged media (MDM) has been successfully developed for solving such problems [1,2].

By now, a large number of constitutive relations of MDM describing damage development in a material have been developed. However, most of these equations are focused only on certain loading modes, not related to specific equations of deformation processes. In fact, the history of thermoplastic deformation (the type of strain path, the nature

of temperature change, the type of stress state, the history of its change, etc.) significantly affects the rate of damage accumulation. This emphasizes the importance of considering the kinetics of the stress-strain state (SSS) in hazardous areas of structural elements and its theoretical description by the corresponding equations of state [1,2].

At present, approaches to evaluating fatigue life of materials and structures based on the concept of damaged media have been widely developed [1,2,4-16].

General provisions on the evolution equations of damage accumulation were formulated in [8]. It is noted that generally the strength criterion should represent a process equation rather than a boundary condition. This equation should take into account time and history (trajectory) of loading (deformation), i.e. it should be written in the speeds (increments) of the corresponding values and be closely related to the governing equations describing the process of material deformation.

In [9,10], the MDM model employed in modern computing systems of finite element analysis such as ANSYS, Abaqus, and others were elaborated. The Chaboche model consists of three interrelated parts:

- constitutive relations of cyclic plasticity;
- evolutionary equations for fatigue damage accumulation;
- strength criterion of the damaged material.

In work [5], evolutionary equation of fatigue damage accumulation for monotonic and cyclic deformation of materials is formulated on the basis of the plasticity theory with kinematic and isotropic hardening.

The process of cyclic deformation is considered to occur under soft, hard or mixed loading conditions and to be stationary or non-stationary, symmetric or asymmetric.

Work [16] presents an investigation of the processes of viscoplastic deformation and fracture of materials and structures on the basis of the composite model of the damaged material. The model is based on the ability to represent a complex process of propagation of the interrelated effects of deformation and fracture in a series of formally independent elementary acts described by respective partial models of plasticity, creep and damage accumulation. Calculation of mutual influence of such basic acts is at the top level in the general model of the damaged material.

The direct effect of damage on the deformation process is calculated in the model by introducing the dependence of elastic moduli of material on the current damage value.

The following models are used to describe the process of elastoplastic deformation and damage accumulation:

- a thermoplasticity model with a combined translational-isotropic hardening;
- a damage accumulation model based on the change in the energy of plastic deformation and on the kinetic equations for changing the damage degree at brittle fracture.

In [1,2], a mathematical model of mechanics of damaged media (MDM) was developed, describing processes of complex plastic deformation and damage accumulation in structural materials (metals and their alloys) under monotonous and cyclic proportional and non-proportional regimes of thermal-mechanical loading. In the present paper, the model is used for describing the processes in stainless steels 12X18H10T, 12X18H9 (the designation of steels in this article is given in Russian) under block-type non-stationary non-symmetric low-cycle loading. The obtained numerical results are compared with the data from full-scale experiments.

2. Defining relations of mechanics of damaged media

The damaged medium model [1,2] consists of three interrelated parts:

- the relations of elastic-plastic behavior of the material, accounting for the effect of the failure process;
- the evolutionary equations of damage accumulation kinetics;
- the strength criterion of the damaged material.

The defining relations of plasticity are based on the following basic assumptions:

- components of strain tensors e_{ij} and strain rates \dot{e}_{ij} include elastic e_{ij}^e , \dot{e}_{ij}^e and plastic e_{ij}^p , \dot{e}_{ij}^p strains;
- the initial yield surface for various temperatures is described by a Mises-type surface. The evolution of the yield surface is described by the evolution of its radius C_p and displacement of its center ρ_{ij} ;
- the body volume is elastic;
- the initial medium is isotropic. Anisotropy due to the plasticity processes is only taken into account.

In the elastic region, the correlation between the spherical and deviatoric components of the stress and strain tensors is described by Hook law.

To describe the effects of monotonous and cyclic deformation, a yield surface is introduced:

$$F_s = S_{ij}S_{ij} - C_p^2 = 0, \quad S_{ij} = \sigma_{ij} - \rho_{ij}. \quad (1)$$

To describe complex cyclic deformation modes in the stress space, a cyclic "memory" surface is introduced:

$$F_p = \rho_{ij}\rho_{ij} - \rho_{\max}^2, \quad (2)$$

where ρ_{\max} is maximal modulus of variable ρ_{ij} for the entire loading history.

It is assumed that the structure of the evolutionary equation for the yield surface radius has the form:

$$\dot{C}_\chi = [q_\chi H(F_\rho) + a(Q_s - C_p)\Gamma(F_\rho)]\dot{\chi} + q_3\dot{T}, \quad (3)$$

$$C_p = C_p^0 + \int_0^t \dot{C}_p dt, \quad \dot{\chi} = \left(\frac{2}{3}\dot{e}_{ij}^p\dot{e}_{ij}^p\right)^{1/2}, \quad \chi_m = \int_0^t \dot{\chi} H(F_\rho) dt, \quad \chi = \int_0^t \dot{\chi} dt, \quad (4)$$

$$q_\chi = \frac{q_2 A \psi_1 + (1-A)q_1}{A\psi_1 + (1-A)}, \quad Q_s = \frac{Q_2 A \psi_2 + (1-A)Q_1}{A\psi_2 + (1-A)}, \quad 0 \leq \psi_i \leq 1, \quad i = 1, 2$$

$$A = 1 - \cos^2\theta, \quad \cos\theta = n_{ij}^e n_{ij}^s, \quad n_{ij}^e = \frac{\dot{e}_{ij}^e}{(\dot{e}_{ij}^e \dot{e}_{ij}^e)^{1/2}}, \quad n_{ij}^s = \frac{S_{ij}}{(S_{ij} S_{ij})^{1/2}}, \quad (5)$$

$$H(F_\rho) = \begin{cases} 1, & F_\rho = 0 \wedge \rho_{ij}\dot{\rho}_{ij} > 0 \\ 0, & F_\rho < 0 \vee \rho_{ij}\dot{\rho}_{ij} \leq 0 \end{cases}, \quad \Gamma(F_\rho) = 1 - H(F_\rho),$$

where q_1 , q_2 , q_3 are isotropic hardening moduli, Q_1 and Q_2 are cyclic hardening moduli, a is a constant defining the stabilization process rate of the hysteresis loop of cyclic deformation of the material, Q_s is stationary value of the yield surface radius for the ρ_{\max} and T , C_p^0 is initial value of the yield surface radius.

$$\dot{\rho}_{ij} = \tilde{g}_1 \dot{e}_{ij}^p - g_2 \rho_{ij} \dot{\chi} + \dot{\rho}_{ij}^*, \quad \rho_{ij} = \int_0^t \dot{\rho}_{ij} dt, \quad (6)$$

$$\tilde{g}_1 = g_1 + k_1 \left(1 - e^{-k_2 \chi_m}\right) \langle \cos \beta \rangle, \quad \rho_{ij} = \int_0^t \dot{\rho}_{ij} dt, \quad (7)$$

$$\dot{\rho}_{ij}^* = g_3 \dot{\epsilon}_{ij}^p H(F_\rho) - g_4 \rho_{ij} \dot{\chi}, \quad (8)$$

where g_1, g_2, g_3, g_4, k_1 и k_2 are experimentally determined material parameters.

For non-symmetric both hard and soft cyclic loading, term $\dot{\rho}_{ij}^*$ enables equation (6) to describe the processes of placing and ratcheting of the cyclic plastic hysteresis loop. For $g_3 = g_4 = k_1 = 0$, one obtains from (6) a special case of equation (6) – the Armstrong–Frederick–Kadashevich equation:

$$\dot{\rho}_{ij} = g_1 \dot{\epsilon}_{ij}^p - g_2 \rho_{ij} \dot{\chi}. \quad (9)$$

To describe the evolution of the "memory" surface, it is necessary to formulate an equation for ρ_{\max} :

$$\dot{\rho}_{\max} = \frac{(\rho_{ij} \dot{\rho}_{ij}) H(F_\rho)}{(\rho_{mn} \rho_{mn})^{1/2}} - g_2 \rho_{\max} \dot{\chi} - g_3 \rho_{\max} \dot{T}. \quad (10)$$

The plastic strain rate tensor components obey the law of orthogonality of the plastic strain rate vector to the yield surface at the loading point:

$$\dot{\epsilon}_{ij}^p = \lambda S_{ij}. \quad (11)$$

At the stage of the development of defects scattered over the bulk, the effect of damage on the physical-mechanical properties of the material is observed. This effect can be accounted for by introducing effective stresses:

$$\begin{aligned} \tilde{\sigma}'_{ij} &= F_1(\omega) \sigma'_{ij} = \frac{G}{\tilde{G}} \sigma'_{ij} = \frac{\sigma'_{ij}}{(1-\omega) \left[1 - \frac{(6K+12G)\omega}{(9K+8G)} \right]}, \\ \tilde{\sigma} &= F_2(\omega) \sigma = \frac{K}{\tilde{K}} \sigma = \frac{\sigma}{4G(1-\omega)/(4G+3K\omega)}, \quad \tilde{\rho}_{ij} = F_1(\omega) \rho_{ij}, \end{aligned} \quad (12)$$

where \tilde{G}, \tilde{K} are effective moduli of elasticity determined using McKenzie formulae [2,6].

It is postulated that the rate of the damage accumulation process for low-cycle fatigue (LCF) is defined by an evolutionary equation of the form [1,2,7,8]:

$$\dot{\omega} = f_1(\beta) f_2(\omega) f_3(W) f_4(\dot{W}), \quad (13)$$

where functions $f_i, i=1...4$ account for: capacity of stressed state ($f_1(\beta)$), level of accumulated damage ($f_2(\omega)$), accumulated relative damage energy for the nucleation of defects ($f_3(W)$) and rate of change of damage energy ($f_4(\dot{W})$).

In equation (13):

$$f_1(\beta) = \exp(\beta), \quad f_2(\omega) = \begin{cases} \omega^{1/3} (1-\omega)^{2/3} \wedge W > W_a \wedge \omega \leq 1/3, \\ \frac{\sqrt[3]{16}}{9} \omega^{-1/3} (1-\omega)^{-2/3} \wedge W > W_a \wedge \omega > 1/3, \end{cases} \quad (14)$$

$$\dot{\omega} = f_1(\beta) f_2(\omega) f_3(W) f_4(\dot{W}), \quad (15)$$

where β is capacity parameter of stressed state ($\beta = \sigma/\sigma_u$), W_a is value of the damage energy at the end of the nucleation stage of scattered defects under LCF, and W_f is energy value corresponding to the formation of a macroscopic crack.

The condition when damage level ω reaches its critical value

$$\omega = \omega_f \leq 1 \quad (16)$$

is taken as a criterion of the termination of the phase of the development of scattered micro-defects.

3. Numerical results

Specimens of 12X18H10T stainless steel were experimentally tested in the conditions of hard uniaxial tension-compression at ambient temperature. The testing program consisted of five blocks including monotonous and cyclic loading [5]:

- the first block consists of 20 cycles of symmetric hard cyclic loading with the strain amplitude of $e_{11}=0.0008$;
- the second block implements monotonous tension up to $e_{11}=0.05$;
- the third block consists of 200 cycles of non-symmetric cyclic loading with the strain range of $\Delta e_{11} = e_{11}^{(+)} - e_{11}^{(-)} = 0.012$ and average strain $e_{11}^{(m)} = 0.044$ (during this block, placing of the plastic hysteresis loop takes place);
- in the fourth block, monotonous tension up to $e_{11}=0.01$ is realized;
- the fifth block implements non-symmetric cyclic loading with the strain range of $\Delta e_{11} = e_{11}^{(+)} - e_{11}^{(-)} = 0.012$ and average strain $e_{11}^{(m)} = 0.094$ up to failure (number of cycles to failure $N_f = 2800$). During this loading block, placing of the plastic hysteresis loop also takes place.

Tables 1–3 list the main physical-mechanical parameters of the MDM model for steel 12X18H10T, determined from the results of the basic experiment [1,2], which are used in the calculations.

Table 1. Physical-mechanical characteristics and parameters of the MDM model

K , MPa	G , MPa	C_p^o , MPa	g_1 , MPa	g_2	g_3 , MPa	g_4	k_1 , MPa	k_2	a
165277	76282	203	20850	297	660	3	10000	0.2	5

Table 2. Modulus of cyclic hardening $Q_S(\rho_{\max})$ (MPa)

Q_S , MPa	203	210	232	232	232	232	232
P_{\max} , MPa	0	30	60	90	100	110	120

Table 3. Modulus of monotonous hardening q_χ (MPa)

q_k , MPa	-17000	-4634	-811	371	737	849
χ	0	0.002	0.004	0.006	0.008	0.01
q_k , MPa	897	900	900	900	900	900
χ	0.015	0.02	0.03	0.04	0.05	0.09

Figure 1 depicts the 20-th cycle of symmetric loading followed by monotonous tension up to $e_{11} = 0.05$ and the first cycle of non-symmetric loading. Here and in what follows the dots correspond to the test data and the solid lines show the computational results.

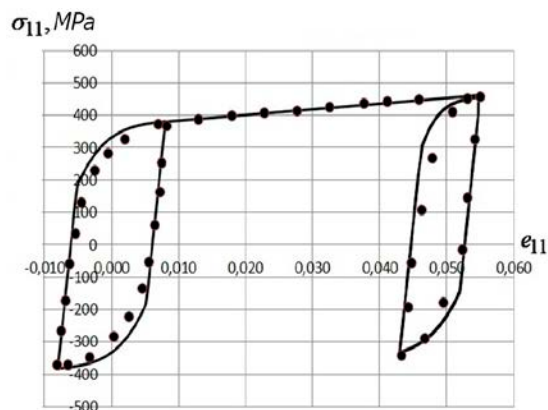


Fig. 1. Deformation diagram during the transition from symmetric cyclic loading to asymmetrical cyclic loading by monotonic stretching

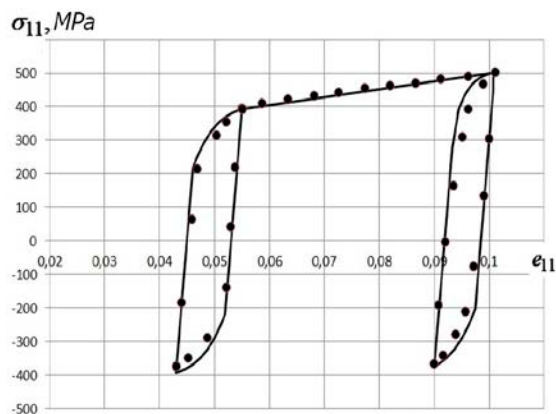


Fig. 2. Deformation diagram during the transition from the third to the fifth block of asymmetric cyclic loading

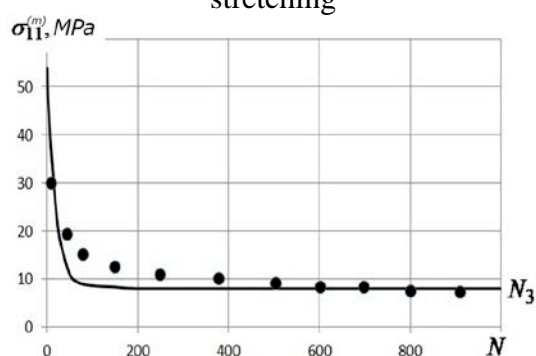


Fig. 3. The dependence of the average stress in the cycle on the number of cycles for the third block of loading

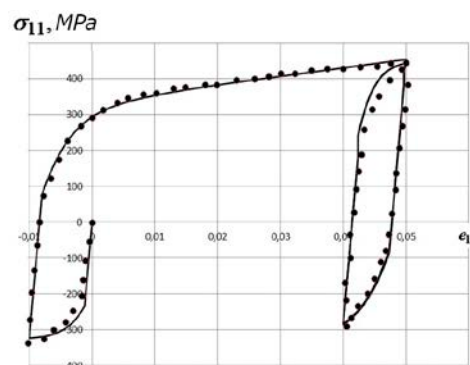


Fig. 4. Deformation process for the second loading block

Figure 2 shows the cyclic deformation diagram at the end of the third (the 200-th cycle) and the beginning of the fifth (the 1-st cycle) loading blocks. Figure 3 presents the results illustrating the processes of placing of the plastic hysteresis loop during the third block of non-symmetric cyclic loading (variation of the average stress $\sigma_{11}^{(m)}$ over the cycle in the process of cyclic loading). Both qualitative and quantitative agreement of the experimental and computational data is observed.

Specimens of stainless steel 12X18H9 were experimentally studied under hard non-stationary non-symmetric cyclic loading consisting of two blocks:

- in the first block, the specimen is compressed up to the strain of $e_{11}=0.01$, followed by tension up to $e_{11}=0.05$;
- in the second block, non-symmetric hard cyclic loading with the strain range of $\Delta e_{11} = e_{11}^{(+)} - e_{11}^{(-)} = 0.01$ is implemented up to failure ($N_f=850$). Here, placing of the plastic hysteresis loop takes place (Fig. 5), and after the 500-th loading cycle the loop becomes practically symmetric;

Tables 4–6 list the main physical-mechanical characteristics and material parameters of the MDM model for steel 12X18H9 as determined from the results of the basic experiment [1,2], which are used in the calculations.

Table 4. Physical-mechanical characteristics and parameters of the MDM model

K , MPa	G , MPa	C_p^o , MPa	g_1 , MPa	g_2	g_3 , MPa	g_4	k_1 , MPa	k_2	a	W_a , J/m ³	W_f , MJ/m ³
165277	76282	190	24090	286	800	2	10000	0.2	5	0	800

Table 5. Modulus of cyclic hardening $Q_s(\rho_{max})$ (MPa)

Q_s , MPa	190	205	210	215	220	225	225
P_{max} , MPa	0	20	40	60	80	100	120

Table 6. Modulus of monotonous hardening q_χ (MPa)

q_χ , MPa	-5000	-4471	-4188	-3859	-2460	-182
χ	0	0.002	0.004	0.006	0.008	0.01

q_χ , MPa	888	1531	1274	913	913	913
χ	0.015	0.02	0.03	0.04	0.05	0.06

Figure 4 shows the deformation process for steel 12X18H9 during the second loading block (500-th cycle).

Figure 5 depicts the history of average stress $\sigma_{11}^{(m)}$ over a cycle in the process of cyclic loading during the second block. Both qualitative and quantitative agreement of the experimental and numerical results is also observed.

Figure 6 presents a fatigue curve for stainless steel 12X18H9 under hard symmetric cyclic loading. The comparison of the experimental and computational results testifies to their qualitative and, adequate for engineering design purposes, quantitative agreement.

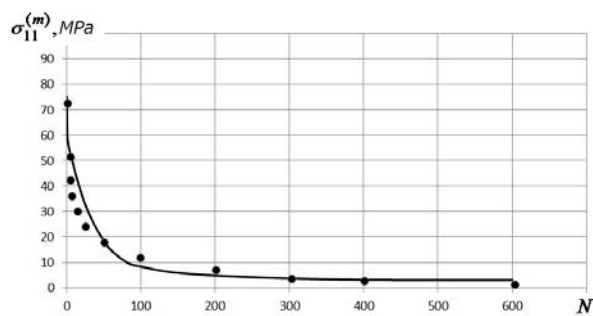


Fig. 5. The dependence of the average stress in the cycle on the number of cycles for the second loading block

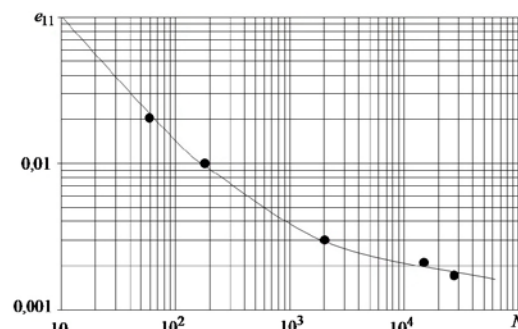


Fig. 6. Fatigue curve for steel 12X18H9

Inverse Fourier transform, sine and cosine transformation are done numerically through an algorithm presented in [12,13].

4. Conclusion

The comparison of the results of numerical experiments against the test data on plastic deformation and damage accumulation in stainless steels (12X18H10T, 12X18H9) under block non-stationary non-symmetric low-cycle loading corroborates the reliability of the defining equations of the MDM model and its adequacy in determining material parameters.

This result are in addition to the results obtained earlier in [11-13,15] when were considered problems of constructing surface Green's functions.

Acknowledgements. *The work is financially supported by the Federal Targeted Program for Research and Development in Priority Areas of Development of the Russian Scientific and Technological Complex for 2014-2020 under the contract No. 14.578.21.0246 (unique identifier RFMEFI57817X0246).*

References

- [1] Volkov IA, Korotkikh YG. *Equations of state of viscoelastoplastic damaged media*. Moscow: Fizmatlit; 2008. (In Russian)
- [2] Volkov IA, Igumnov LA. *Introduction to continuum mechanics damaged enviroment*. Moscow: Fizmatlit; 2017. (In Russian)
- [3] Collins J. *Renormalization*. Moscow: Mir; 1984.
- [4] Lemaitre J. Damage modelling for prediction of plastic or creep fatigue failure in structures. In: *Trans. 5th Int. Conf. SMRiT*. North Holland; 1979. p.L 5/1b.
- [5] Bondar VS, Abashe DR, Petrov VK. Comparative analysis of variants of plasticity theories under cyclic loading. *PNRPU Mechanics Bulletin*. 2017;2: 23-44. (In Russian)
- [6] Murakami S. Deformation damage theory of materials and its application to the analysis of the deformation process of square plates. *J. Mec. Theor. Appl.* 1982;1: 743-761.
- [7] Bonder SR, Lindholm US. The criteria of the growth of defects for time-dependent failure of materials. *Proc. Amer. Soc. Mech. Eng. Ser. D. Theoret. Bases of Eng. Calculations*. 1976;100(2): 51-58. (In Russian)
- [8] Lemaitre J. A continuum model of damage used in analyzing failure of plastic materials. *Proc. Amer. Soc. Mech. Eng. Ser. D Theoret. Bases of Eng. Calculations*. 1985;107(1): 90-98. (In Russian)
- [9] Chaboche JL. Constitutive equation for cyclic plasticity and cyclic viscoplasticity. *Inter. J. of Plasticity*. 1989;5(3): 247-302.
- [10] Chaboche JL. Continuous damage mechanics a tool to describe phenomena before crack initiation. *Engineering Design*. 1981;64(2): 233-247.
- [11] Cardebois JP, Sidoroff F. Damage Induced Elastic Anisotropy. In: Boehler JP. (ed.) *Mechanical Behavior of Anisotropic Solids / Comportment Mécanique des Solides Anisotropes*. Dordrecht: Springer; 1982. p.761-774.
- [12] Betten J. Damage tensors in continuum mechanics. *Journal de Mécanique et applique*. 1983;2(1): 13-32.
- [13] Beaver PW. Biaxial Fatigue and Fracture of Metals: a Review. *Metals Forum*. 1985;8(1): 14-29.
- [14] Jordan EU, Broun MW, Miller KJ. Fatigue under severe nonproportional loading. In: *ASTM STP 853*. Philadelphia: American Soc. for Testing and Material; 1985. p.569–585.
- [15] Wang J, Chaw CL. Mixed mode ductile fracture studies with nonproportional loading based on continuum damage mechanics. *Trans. ASME. J. Eng. Mater. and Technolog.* 1989;111(2): 204-209.
- [16] Kapustin SA, Churilov YA, Gorokhov VA. *Modelirovanie nelineynogo modelirovaniya i razrusheniya konstruktsiy v usloviyakh mnogofaktornykh vozdeystviy na osnove MKE*. Nyzhny Novgorod: Izdatelstvo NNGU; 2015. (In Russian)

EFFECT OF BAMBOO WEIGHT FACTION ON MECHANICAL PROPERTIES IN NON-ASBESTOS COMPOSITE OF MOTORCYCLE BRAKE PAD

Y. Sukrawan^{*}, A.Hamdani, S.A. Mardani

Departemen Pendidikan Teknik Mesin, Universitas Pendidikan Indonesia, Jl. Dr. Setiabudi no 229,

Bandung 40154, Indonesia

*e-mail: yusepsukrawan@upi.edu

Abstract. This study aims to determine the mechanical properties of the use of brake pads based on composite materials from bamboo fiber, and to evaluate the effect of replacement of brake pad material made from asbestos with natural materials to avoid the impacts of asbestosis substances, such as cancer. The method used several stages: weighing, mixing, inserting materials in molding, compacting, and sintering. The stages were carried out in three types of composites: Composite 1 (40% of bamboo fiber, 30% of MgO, and 30% of epoxy resin), composite 2 (50% of bamboo fiber, 25% of MgO, and 25% of epoxy resin), and composite 3 (60% of bamboo fiber, 20% of MgO, and 20% of epoxy resin). Tests for mechanical properties were carried out using a standard analysis, such as wear rate using ASTM D3702-94 standard, hardness test using ASTM D 785-03 type R, heat resistance using 2300 testing temperature, and composite brake lifetime analysis. The results showed that the composition of bamboo brought great influences on the mechanical properties. The best specimen had a wear rate of $0.9612 \cdot 10^{-8}$ g/mm².s, hardness of 91.8 HRR, and heat resistance at 280°C with a duration of 810 days. It is expected that the use of composite brake pads made from bamboo fiber can replace brake pads made from asbestos, which is healthier and safer to use.

Keywords: asbestosis, bamboo fiber, composite material, brake pad

1. Introduction

Brake Pad is one of the important components in motorized vehicles on the highway. The development of two-wheeled motorized vehicles is currently increasing rapidly in line with the economic growth in the community. Along with rapid growth, problems often occur in vehicles such as brakes that can cause cancer due to the existence of asbestos dust during breaking [1-4].

The quality of brake lining is determined by several factors, including the composition of the material, the type of material, and the hardness of the material. Brake lining made from asbestos braking ability will decrease at a temperature of 200°C, and above that temperature will cause brake failure [5]. One alternative that is being developed for use on motorbikes is changing the composition of brake pads, based on the green composite concept.

Green composite criterion is material that has one or two components (matrix and reinforcing fibers) as a biological based component [6,7]. This component can be: (a) Natural reinforcing fibers with synthetic polymeric matrix (polyolefins polyester, epoxy, vinylester, phenolics), (b) Natural polymer matrix (Polylactic Acid / PLA,

PolyhydroxyAlkanoat / PHA) reinforced with natural fibers (jute, ramie, bamboo), and (c) Natural polymer matrix reinforced with synthetic fibers (E-glass or carbon fiber).

Composites consist of a combination of two or more materials on the macroscopic scale. In practical condition, the composite consists of a main material (matrix), and one type of component as a reinforcement to increase the strength and stiffness of the matrix. The reinforcement component is usually in the form of fibers. Composite materials have advantages such as lighter weight, stronger, higher durability, corrosion resistance, and having good wear resistance [8].

Natural lignin-based reinforcing fibers (such as bamboo, flax, palm fiber, and coconut) have been shown to contribute better to green composite strength [9]. The reasons for choosing natural fibers for green composites are:

- (1) Adverse effects of application of natural fibers are smaller than synthetic fibers,
- (2) Applications of natural fibers can reduce the use of synthetic matrices because for the same performance composites need more natural fibers than synthetic fibers,
- (3) On automotive applications, lower natural fiber density can support increased fuel oil efficiency,
- (4) CO₂ emissions from combustion of green composites are smaller than synthetic composites.

Bamboo fiber is used as an existing substitute material because it is economical and light [10]. The latest development found the advantages of bamboo fiber green composites, in which the vibration reduction capacity of the product was better than glass fiber synthetic polymer composites [11]. Researches on green composite reinforced bamboo fiber and epoxy matrix have been carried out, even applied for bulletproof vests. Bamboo fiber is quite efficient, lightweight, and more economical for bulletproof applications compared to aramid fiber [12]. Modification of bamboo fiber for epoxy composites proves an increase in tensile strength and significant elongation in resulting new composite [13].

Here, this study aims to determine the mechanical properties of the use of brake pads based on composite materials from bamboo fiber. This bamboo was used for replacing brake pad material made from asbestos with natural materials to avoid the effects of asbestosis substances, such as cancer. As a model of bamboo, *dendrocalamus asper* was used. *Dendrocalamus asper* is one type of bamboo that has a large stem size and is included in the tribe of grasses. The researches begun with making a mixture of ingredients. The formula consists of several constituent materials, such as binder (epoxy resin), fiber material (bamboo fiber), and filler material (MgO). Then, the process of mixing the ingredients until the production of brake pads is made with several variations of the addition of bamboo fiber.

The making of brake pads is determined based on a predetermined reference, such as the value of mechanical properties must be based on the value of the safety standard [14]:

- (1) For the value of violence according to safety standards = 68-105.
- (2) Heat resistance of 360°C, for continuous use = up to 250°C.
- (3) The value of wear of brake linings = is 5×10^{-4} - 5×10^{-3} mm²/kg.
- (4) Coefficient of friction = 0.14 – 0.27.
- (5) The mass of the type of brake lining = 1.5 - 2.4 g/cm³.
- (6) Thermal conductivity = 0.12 - 0.8 Wm/K.
- (7) Specific pressure = 0.17 - 0.98 J/g°C.
- (8) Shear strength = 1300 - 3500 N/cm².
- (9) Strength of fracture = 480 - 1500 N/cm².

To determine the mechanical strength of composite materials, the reference test must be based on stipulated provisions such as the description above.

2. Method

This study varied the addition of bamboo fiber, while the dosage between MgO and epoxy resin was fixed. The addition of bamboo fiber fraction includes 40, 50, and 60% (See Table 1)

Table 1. Variation in composition between samples

Specimen	MgO (%)	Bamboo Fiber (%)	Epoxy Resin (%)
Composite 1	30	40	30
Composite 2	25	50	25
Composite 3	20	60	20

Steps for making specimens are in the following. First, we performed and checked the mass composition for each materials. Then, the each component was added and mixed. The mixing process used an electric stainless steel mixer with a rotating speed of around 13,600-15,700 rpm (adjusted to the Atomic Tuned 2 Pro brand) for 8 minutes. The mixed components were put into the mold and compacted under a specific condition. The compaction process was carried out by adding force into the mold. This process was carried out by loading 200 psi for 20 minutes. Finally, the pressed component was sintered at 180°C for 30 minutes using an electrical furnace.

3. Results and Discussion

In the process of making motorcycle composite brake pads, we varied the mixture composition. The following are the results of weighing of each composition: Composite 1, 2, and 3 contained 7.9998; 7.5874; and 7.3070 g of sample. Detailed information for the composition of each component is shown in Table 2.

Table 2. Heavy fraction

Specimens	MgO(gram)	Bamboo Fiber (gram)	Ratio of resin andhardener	Composite Weight (gram)
Composite 1	2.50	3.25	12:2	7.9998
Composite 2	2.00	3.80	10:2	7.5874
Composite 3	1.50	4.35	8:2	7.3070

Coefficient of friction. To determine the friction coefficient, determination of the torque (T) used in the following formula:

$$T = P/\omega, \quad (1)$$

where P is the electricity power and ω is the rotation. Then, applied $P = 24$ Watt and $\omega = 180$ rpm, we can get $T = 24/180 = 0.13$ Nm.

Specific the friction coefficient (μ) was calculated using the following formula:

$$\mu = T/(2 \cdot F_n \cdot r), \quad (2)$$

where F_n and r are the force applied and the diameter of rod, respectively. Then, applied the condition of $r = 0.3$ m and $F_n = 2.3 \cdot 9.8 = 22.54$ N, we can get $\mu = 0.13/(2 \cdot 22.54 \cdot 0.3) = 0.0096$.

Testing the value of ware rate. Before testing, we checked the weight of sample before and after testing. The wear rate test used the ASTM D3702-94 Standard with a load of 2.3 kg and a speed of 180 rpm. We found that there is an increase in the mass. However, the increases in the mass are less than 0.5%.

The calculation in determining the value of the wear rate of a material using the formula, as follows:

$$M = (M_a - M_b) / (t \cdot A), \quad (3)$$

where M is the value of wear rate, M_a is the composite initial weight (gram), M_b is the composite final weight (gram), t is the testing time (second), and A is the frictional cross section area (mm^2). The wear test results in 1800 seconds are shown in Table 3.

Table 3. Wear rate obtained during the testing

Specimens	M_a (gram)	M_b (gram)	t (second)	A (mm^2)	M ($\text{g}/\text{mm}^2 \cdot \text{s}$)
Composite 1	6.4265	6.4142	1800	289	$2.3644 \cdot 10^{-8}$
Composite 2	4.5902	4.5816	1800	289	$1.6532 \cdot 10^{-8}$
Composite 3	4.0517	4.0467	1800	289	$0.9612 \cdot 10^{-8}$

From the results of testing the wear rate, the best wear resistance value occurs in the small value of the wear rate that is in the third specimen. So, by increasing the composition of bamboo fiber, the lower the wear rate of brake lining samples was obtained. This informs the material to be more resistant to wear [15].

Hardness test. The hardness test on the composite results and compares with the hardness value of the Rockwell Hardness of Plastics and Electrical Insulating Materials. This testing is important for understanding the effect of additional component into the material [16-20]. The testing procedure was carried out using ASTM D 785-03 type R with an indenter diameter of 12.7 mm and a minor load of 10 kg and a major load of 60 kg. The results of hardness testing are shown in Table 4.

Based on the three specimens, the addition of bamboo fiber has an impact on the hardness of the material. The more amount of bamboo fiber was added, the harder the material can be obtained [21]. Based on the safety standards, the mechanical properties of composite brake pads are in the standard safety range of 68.3-91.8 HRR (safety standard composite brake pads 68-105 HRR).

Table 4. Composite hardness value

Specimens	Rockwell R hardness value(HRR)			Average value of hardness (HRR)
	Testing number			
	1	2	3	
Composite 1	67.50	67.00	70.50	68.30
Composite 2	72.00	97.00	98.00	89.00
Composite 3	89.00	93.50	93.00	91.80

Calculation of lifetime of Composite Brake Shoes. To find out the lifetime of composites, we used the following formula:

$$U(n) = M_a / M_i, \quad (4)$$

where $U(n)$ is the lifetime (days), M_a is the initial brake pad mass (gram), M_i is the mass wasted in 1800 seconds (gram). The calculation results of each composition are shown in Table 5.

When compared with other compositions, the third composite has a relatively long usage of age compared to the first and second composites. This informs that the third composite is able to survive with the optimum specifications for 810 days.

Table 5. The lifetime of composite brake pads

Specimens	Initial Mass (gram)	Gram wasted/ 800 seconds	Time	Second	Hour	Day
Composite 1	6.4265	0.0123	523	941400	261.50	523
Composite 2	4.5902	0.0086	534	961200	267.00	534
Composite 3	4.0517	0.0050	810	1458000	405.00	810

Heat resistance testing. Heat resistance testing was done using an electrical furnace with the following regulatory specifications: processing time to reach a maximum temperature from room temperature is 7 minutes, holding time at the specific temperature is 10 minutes, and the testing temperature is 230°C. Each sample was done twice.

The following images paneled in Fig. 1 are the results of heat resistance testing. The condition of composite 1 (Figs. 1a and 1b) did not burn or burn due to heating, but the color of the specimen looks darker before heating the furnace. The condition of composite 2 (Figs. 1c and 1d) did not burn or scorch like a composite 1, but the color appears slightly dark compared to the initial state. The condition of composite 3 (Figs. 1e and 1f) did not burn or scorch like composites 1 and 2, but there is a difference other than the color that appears slightly dark and the bamboo fiber looks black.

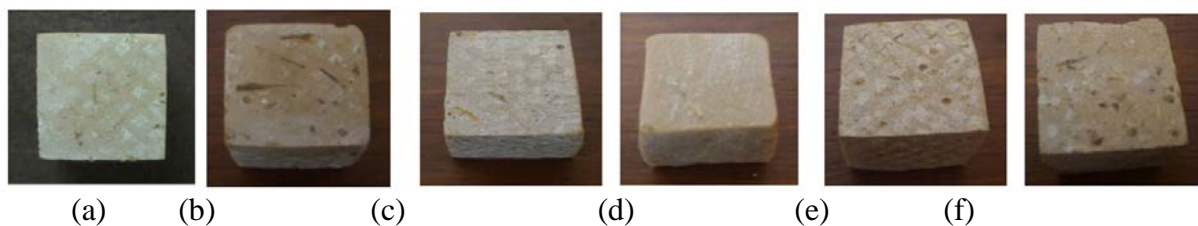


Fig. 1. Image of condition before-after heat testing. Figures (a) and (b) are for composite 1, Figures (c) and (d) are for composite 2, and Figures (e) and (f) are for composite 3

Based on the three specimens, there was no fire at all in the testing specimens. In this test, the brake lining specimens made from composites were better than ordinary brake pads made from asbestos, which could survive up to temperatures of 200°C [5].

4. Conclusions

Based on the data and analysis of the calculations, it can be concluded that bamboo is effective to be used. The best constituent material is in the third composite because it has the best mechanical properties, such as the wear rate of $0.9612 \cdot 10^{-8} \text{ g/mm}^2$ (in which this can remain up to 810 days (2 years and 3 months)), hardness value of 91.8 HRR, and having good heat resistance (because there is no fire or burning phenomena during the testing specimen). This study demonstrates that natural based renewable materials from bamboo has good mechanical strength, giving information for the potential usage in motorbikes safely.

Acknowledgements. No external funding was received for this study.

References

[1] Algranti E, Ramos-Bonilla JP, Terracini B, Santana VS, Comba P, Pasetto R, Marsili D. Prevention of asbestos exposure in latinamerica within a global public health perspective. *Annals of Global Health*.2019;85(1): 1-15.

- [2] Hessel PA, Teta MJ, Goodman M, Lau E. Mesothelioma among brake mechanics: an expanded analysis of a case-control study. *Risk Analysis*. 2004;24(3): 547-552.
- [3] Rodelsperger K, Jahn H, Brückel B, Manke J, Paur R, Woitowitz HJ. Asbestos dust exposure during brake repair. *American Journal of Industrial Medicine*. 1986;10: 63-72.
- [4] Paustenbach DJ, Richter RO, Finley BL, Sheehan PJ. An evaluation of the historical exposures of mechanics to asbestos in brake dust. *Applied Occupational and Environmental Hygiene*. 2003;18(10): 786-804.
- [5] Mulahela SKA, Catur AD, Pandiatmi P. Analisis keausan dan waktu pengereman kampas cakram asbestos dan non asbestos dengan variasi beban pengereman dan berat pengendara pada sepeda motor honda supra x 125 cc. *Dinamika Teknik Mesin*. 2015;5(2): 82-89.
- [6] Faruk AKP. Biocomposites reinforced with natural fibers: 2000–2010. *Progress in Polymer Science*. 2012;37(11): 1552-1596
- [7] Suardana NPG, Lokantara IP, Lim JK. Influence of water absorption on mechanical properties of coconut coir fiber/poly-lactic acid biocomposites. *Materials Physics and Mechanics*. 2011;12(2): 113-125.
- [8] Fahmi H, Hermansyah H. Pengaruh orientasi serat pada komposit resin polyester/serat daun nenas terhadap kekuatan tarik. *Jurnal Teknik Mesin*. 2013;1(2): 46-52.
- [9] Hojo T, Xu Z, Yang Y, Hamada H. Tensile properties of bamboo, jute and kenaf mat-reinforced composite. *Energy Procedia*. 2014;56: 72-79.
- [10] Lemen RA. Asbestos in brakes: exposure and risk of disease. *American Journal of Industrial Medicine*. 2004;45(3): 229-237.
- [11] Takagi H, Ichihara Y. Effect of fiber length on mechanical properties of "green" composites using a starch-based resin and short bamboo fibers. *JSME International Journal Series A Solid Mechanics and Material Engineering*. 2004;47(4): 551-555.
- [12] Cruz JM. Giant Bamboo Fiber Reinforced Epoxy Composite in Multilayered Ballistic Armor. *Materials Research*. 2015;18(2): 70-75.
- [13] Lu T, Jiang M, Jiang Z, Hui D, Wang Z, Zhou Z. Effect of surface modification of bamboo cellulose fibers on mechanical properties of cellulose/epoxy composites. *Composites Part B: Engineering*. 2013;51: 28-34.
- [14] Dowlatshahi S. Product design in a concurrent engineering environment: an optimization approach. *The International Journal of Production Research*. 1992;30(8): 1803-1818.
- [15] Wardana PF, Estriyanto Y. Pemanfaatan serbuk bambu sebagai alternatif material kampas rem non-asbestos sepeda motor. *Nosel*. 2013;1(3): 1-8.
- [16] Triawan F, Nandiyanto ABD, Abdullah AG, Aziz M. Plasma nitriding time on the hardness and crystal structure/phase of SUS403 and SCS6 martensitic stainless steels: an analytical study. *Journal of Engineering Science and Technology*. 2018;13(8): 2369-2378.
- [17] Nurprasetio IP, Budiman BA, Triawan F. Failure investigation of plastic shredding machine's flange coupling based on mechanical analysis. *Indonesian Journal of Science and Technology*. 2017;2(2): 124-133.
- [18] Bale JS, Pell YM, Jafri M, Selan R. Experimental Investigation on Mechanical Joint of Lontar (BorassusFlabellifer) Fiber Reinforced Polyester Composites under Static Flexural Test. *Indonesian Journal of Science and Technology*. 2019;4(1): 17-27.
- [19] Pratama ER, Mukhammad AFH. Bearing Failure Analysis on Gearbox Forced Draft Fan at LNG Plant. *Indonesian Journal of Science and Technology*. 2018;3(2): 124-137.
- [20] Fitrianto FD, Estriyanto Y, Harjanto B. Pemanfaatan serbuk tongkol jagung sebagai alternatif bahan friksi kampas rem non-asbestos sepeda motor. *Nosel*. 2013;1(3): 1-11.

Submission of papers:

Manuscript should be submitted (**both MS Word and PDF**) by e-mail to: **mpmjournal@spbstu.ru**

After a confirmation of the paper acceptance, the authors should send the signed hard copy of the "Transfer of Copyright Agreement" form (available at <http://www.mpm.spbstu.ru> section "Authors") by regular post to "Materials Physics and Mechanics" editorial office:

Periodicals Editorial Office, Institute of Advanced Manufacturing Technologies, Peter the Great St.Petersburg Polytechnic University, Polytechnicheskaya, 29, St.Petersburg 195251, Russia.

The scanned copy of the signed "Transfer of Copyright Agreement" should be send by e-mail to: **mpmjournal@spbstu.ru**.

Filetype:

Authors are invited to send their manuscripts **as MS Word file with PDF format copy**.

MS Word file should be prepared according to the general instructions bellow; we are kindly asking the authors to look through the detail instruction at: <http://www.mpm.spbstu.ru>.

Length:

Papers should be limited to 30 typewritten pages (including Tables and Figures placed in the proper positions in the text).

Structure of the manuscript:

PAPER TITLE: CENTERED,

TIMES NEW ROMAN 14 BOLD, CAPITAL LETTERS

A.B. Firstauthor¹, C.D. Secondauthor^{2*} -Times New Roman 12, bold, centered

¹Affiliation, address, country - Times New Roman 10, centered

*e-mail: e-mail of the corresponding author - Times New Roman 10, centered

Abstract. Times New Roman 12 font, single line spacing. Abstract should not exceed 12 lines.

Keywords: please, specify paper keywords right after the abstract.

Paper organization. Use Times New Roman 12 font with single line spacing. Use *Italic* font in order to stress something; if possible, please, use **bold** for headlines only.

Page numbering. Please, do not use page numbering.

Tables, Figures, Equations. Please, see the sample file at <http://www.mpm.spbstu.ru> for more details.

References

References should be subsequently numbered by Arabic numerals in square brackets, e.g. [1,3,5-9], following the sample style below:

[1] Koch CC, Ovid'ko IA, Seal S, Veprek S. *Structural Nanocrystalline Materials: Fundamentals and Applications*. Cambridge: Cambridge University Press; 2007.

[2] Hull D, Bacon DJ. *Introduction to Dislocations*. 5nd ed. Amsterdam: Butterworth-Heinemann; 2011 Available from: <https://www.sciencedirect.com/science/book/9780080966724?via%3Dihub> [Accessed 19th June 2018].

[3] Romanov AE, Vladimirov VI. Disclinations in crystalline solids. In: Nabarro FRN (ed.) *Dislocations in Solids*. Amsterdam: North Holland; 1992;9. p.191-402.

[4] Mukherjee AK. An examination of the constitutive equation for elevated temperature plasticity. *Materials Science and Engineering: A*. 2002;322(1-2): 1-22.

- [5] Soer WA, De Hosson JTM, Minor AM, Morris JW, Stach EA. Effects of solute Mg on grain boundary and dislocation dynamics during nanoindentation of Al–Mg thin films. *Acta Materialia*. 2004;52(20): 5783-5790.
- [6] Matzen ME, Bischoff M. A weighted point-based formulation for isogeometric contact. *Computer Methods in Applied Mechanics and Engineering*. 2016;308: 73-95. Available from: doi.org/10.1016/j.cma.2016.04.010.
- [7] Joseph S, Lindley TC, Dye D. Dislocation interactions and crack nucleation in a fatigued near-alpha titanium alloy. To be published in *International Journal of Plasticity*. *Arxiv*. [Preprint] 2018. Available from: <https://arxiv.org/abs/1806.06367> [Accessed 19th June 2018].
- [8] Pollak W, Blecha M, Specht G. *Process for the production of molded bodies from silicon-infiltrated, reaction-bonded silicon carbide*. US4572848A (Patent) 1983.
- [9] Brogan C. *Experts build pulsed air rig to test 3D printed parts for low carbon engines*. Available from: <http://www.imperial.ac.uk/news/186572/experts-build-pulsed-test-3d-printed/> [Accessed 19th June 2018].

Правила подготовки статей:

Рукопись (**английский язык, MS Word и копия PDF**) должна быть направлена в редакцию журнала по электронной почте: mpmjournal@spbstu.ru.

После подтверждения принятия статьи в печать, авторы должны отправить подписанные:

1. Соглашение о передаче авторских прав (<http://www.mpm.spbstu.ru>, раздел «Авторам»);
2. Экспертные заключения о том, что материалы статьи не содержат сведений, составляющих государственную тайну, и информацию, подлежащую экспортному контролю; по адресу:

Россия, 195251, Санкт-Петербург, Политехническая, д. 29, Санкт-Петербургский политехнический университет Петра Великого, Институт передовых производственных технологий, Редакция периодических изданий.

Скан-копии подписанных документов просим направить по электронной почте: mpmjournal@spbstu.ru

Тип файла:

Редакция принимает **файлы MS Word с копией в формате PDF**. Статья должна быть подготовлена в соответствии с настоящей инструкцией, мы просим авторов также следовать более подробным инструкциям на сайте журнала <http://www.mpm.spbstu.ru> в разделе «Авторам».

Длина статьи:

Статья не должна превышать 30 страниц формата А4, включая Таблицы и Рисунки, размещенные непосредственно в соответствующих местах.

Общие правила оформления статьи:

НАЗВАНИЕ СТАТЬИ: ВЫРОВНЯТЬ ПО ЦЕНТРУ,

ШРИФТ, TIMES NEW ROMAN 14 BOLD, ЗАГЛАВНЫЕ БУКВЫ

Автор(ы): **А.Б. Первыйавтор¹, В.Г. Автор^{2*}** - шрифт Times New Roman 12, bold, по центру

¹Наименование организации, адрес, страна - шрифт Times New Roman 10, по центру

* e-mail автора, представившего статью - шрифт Times New Roman 10, по центру

Аннотация. Аннотация статьи составляет не более 12 строк. Используйте шрифт Times New Roman 12, одинарный межстрочный интервал.

Ключевые слова: укажите ключевые слова после аннотации.

Как организовать текст статьи. Используйте шрифт Times New Roman 12, одинарный межстрочный интервал. При необходимости выделить какую-либо информацию используйте *курсив*. Используйте **полужирный** шрифт только для заголовков и подзаголовков.

Номера страниц. Пожалуйста, не используйте нумерацию страниц

Таблицы, Рисунки, Уравнения. Подробные правила оформления данных элементов статьи приведены в инструкции на сайте журнала <http://www.mpm.spbstu.ru>

Литература

Ссылки приводятся в тексте в квадратных скобках [1,3,5-9]. Стиль оформления ссылок:

[1] Koch CC, Ovid'ko IA, Seal S, Veprck S. *Structural Nanocrystalline Materials: Fundamentals and Applications*. Cambridge: Cambridge University Press; 2007.

[2] Hull D, Bacon DJ. *Introduction to Dislocations*. 5nd ed. Amsterdam: Butterworth-Heinemann; 2011 Available from: <https://www.sciencedirect.com/science/book/9780080966724?via%3Dihub> [Accessed 19th June 2018].

[3] Romanov AE, Vladimirov VI. Disclinations in crystalline solids. In: Nabarro FRN (ed.) *Dislocations in Solids*. Amsterdam: North Holland; 1992;9. p.191-402.

[4] Mukherjee AK. An examination of the constitutive equation for elevated temperature plasticity. *Materials Science and Engineering: A*. 2002;322(1-2): 1-22.

- [5] Soer WA, De Hosson JTM, Minor AM, Morris JW, Stach EA. Effects of solute Mg on grain boundary and dislocation dynamics during nanoindentation of Al–Mg thin films. *Acta Materialia*. 2004;52(20): 5783-5790.
- [6] Matzen ME, Bischoff M. A weighted point-based formulation for isogeometric contact. *Computer Methods in Applied Mechanics and Engineering*. 2016;308: 73-95. Available from: doi.org/10.1016/j.cma.2016.04.010.
- [7] Joseph S, Lindley TC, Dye D. Dislocation interactions and crack nucleation in a fatigued near-alpha titanium alloy. To be published in *International Journal of Plasticity*. *Arxiv*. [Preprint] 2018. Available from: <https://arxiv.org/abs/1806.06367> [Accessed 19th June 2018].
- [8] Pollak W, Blecha M, Specht G. *Process for the production of molded bodies from silicon-infiltrated, reaction-bonded silicon carbide*. US4572848A (Patent) 1983.
- [9] Brogan C. *Experts build pulsed air rig to test 3D printed parts for low carbon engines*. Available from: <http://www.imperial.ac.uk/news/186572/experts-build-pulsed-test-3d-printed/> [Accessed 19th June 2018].

МЕХАНИКА И ФИЗИКА МАТЕРИАЛОВ

42 (3) 2019

Учредители: Санкт-Петербургский политехнический университет Петра Великого,

Институт проблем Машиноведения Российской академии наук

Издание зарегистрировано федеральной службой по надзору в сфере связи,
информационных технологий и массовых коммуникаций (РОСКОМНАДЗОР),

свидетельство ПИ №ФС77-69287 от 06.04.2017 г.

Редакция журнала

Профессор, д.т.н., академик РАН, А.И. Рудской – главный редактор

Профессор, д.ф.-м.н., член-корр. РАН, Д.А. Индейцев – главный редактор

Профессор, д.ф.-м.н. И.А. Овидько (1961 - 2017) – основатель и почетный редактор

Профессор, д.ф.-м.н. А.Л. Колесникова – ответственный редактор

Доцент, к.т.н. А.С. Немов – ответственный редактор

А.Ю. Зобачева, к.т.н. – выпускающий редактор

Л.И. Гузилова – редактор, корректор

Телефон редакции

+7 (812) 591-65-28

E-mail: mpmjournal@spbstu.ru

Компьютерная верстка А.Ю. Зобачева

Подписано в печать 30.08.2019 г. Формат 60x84/8. Печать цифровая
Усл. печ. л. 10,0. Тираж 100. Заказ ____.

Отпечатано с готового оригинал-макета, предоставленного автором
в Издательско-полиграфическом центре Политехнического университета Петра
Великого. 195251, Санкт-Петербург, Политехническая ул., 29.
Тел.: (812) 552-77-17; 550-40-14.

Evolution of the droplet shape in the vapor-liquid-solid growth of III-V nanowires under varying material fluxes	265-271
V.G. Dubrovskii, A.S. Sokolovskii	
Study of heat dissipating material using boron nitride fabricated by laser ablation	272-279
Atsushi Yamaguchi, Pankaj Koinkar, Akihiro Furube	
Comparative study of adsorption of ozone molecule on pristine and Si doped Single Wall Carbon Nanotube by density functional theory.....	280-287
R.G. Atram, M.R. Sonawane	
Effect of warm rolling on microstructure, porosity, and hardness of a spray-formed LM25 aluminum alloy	288-295
Bandi Venkata Ramana Reddy, S.R. Maity, K.M. Pandey	
Coupled thermo-electro-mechanical modeling of thermal fatigue of single-crystal corset samples	296-310
A.V. Savikovskii, A.S. Semenov, L.B. Getsov	
Numerical method of single-crystal turbine blade static strength estimation taking into account plasticity and creep effects	311-322
Boris Vasilyev, Alexander Selivanov	
Identification of micro-mechanical characteristics of monoclinic tungsten trioxide microparticles by nanoindentation technique.....	323-329
A.B.D. Nandiyanto, F. Triawan, R. Firly, A.G. Abdullah, Y. Aono, K. Inaba, K. Kishimoto	
Supercomputing analysis of fan-shaped waves in the Earth's crust at the depth of seismic activity	330-339
V.M. Sadovskii, O.V. Sadovskaya	
Finite element modeling and investigation of elastic homogeneous and heterogeneous materials	340-350
V.L. Leontiev, I.V. Efremenkov	
Neural networks and data-driven surrogate models for simulation of steady-state fracture growth	351-358
A.V. Kalyuzhnyuk, R.L. Lapin, A.S. Murachev, A.E. Osokina, A.I. Sevostianov, D.V. Tsvetkov	
Modeling plastic deformation and damage accumulation processes in structural steels under block non-symmetric low-cycle loading.....	359-366
Ivan A. Volkov, Leonid A. Igumnov, Denis N. Shishulin	
Effect of bamboo weight fraction on mechanical properties in non-asbestos composite of motorcycle brake pad	367-372
Y. Sukrawan, A.Hamdani, S.A. Mardani	